RANDOM MEDIA CHARACTERIZATION FROM LASER SPECKLE FREQUENCY CORRELATIONS

A Thesis

Submitted to the Faculty

of

Purdue University

by

Mark A. Webster

In Partial Fulfillment of the

Requirements for the Degree

of

Doctor of Philosophy

December 2002

I dedicate this thesis to my parents, Andrew and Lynette, and my brother, Peter, whose love, encouragement, and support made this possible.

ACKNOWLEDGMENTS

I am deeply grateful to my thesis advisor, Prof. Kevin Webb, for his guidance, encouragement, and patience, enabling me to complete this thesis. I also wish to thank him for providing me with independence to pursue the many interesting research directions in this challenging project. I am also indebted to my advisory committee, in particular, Prof. Andrew Weiner for the close collaboration and for his experimental insight. Also, to Prof. Dan Elliott and Prof. Rick Millane for their critical observations and comments. I thank Dr. Dan Leaird for his technical assistance.

I owe many thanks to the friends that I have made during my time at Purdue for making it truly memorable. I am especially thankful to David, Tammy, Cathy, Katrin, Polly, Jeff, Steve, Dan, Ivan, Rajesh, Ramesh, Rafael, Riccardo, Jason, Jim, Soheila, and Kelly. Finally, I am especially grateful to Kausar for her kindness, support, and wisdom when things became difficult, and for putting up with me when I became difficult.

TABLE OF CONTENTS

Page

LIST OF TABLES

LIST OF FIGURES

Figure Page

Figure Page

ABSTRACT

Webster, Mark A. Ph.D., Purdue University, December, 2002. Random Media Characterization From Laser Speckle Frequency Correlations. Major Professor: Kevin J. Webb.

The study of wave propagation through random media is important for measurements involving the atmosphere and for other environmental sensing applications. Of recent importance, is the study of near-IR light within biological tissue for imaging and spectroscopy, especially for tumor detection.

Highly coherent laser light propagating through a random medium accumulates a random phase due to the multiple scattering and forms an intensity speckle pattern when imaged. It is demonstrated experimentally that the statistical properties of the resultant speckle pattern enables the scattering properties of the random medium to be characterized. In particular, the key result of this study shows for the first time that third-order frequency correlations of a speckle pattern allow the temporal response of a random medium to be determined. The statistical properties of the speckle pattern are also sensitive to the coherence of the source and to any inhomogeneities within the random medium, thus providing potential for optical imaging.

1. INTRODUCTION

1.1 Applications of Light in Random Media

The study of wave propagation through random media is important for many environmental sensing applications, as well as for the important area of biomedical optics [1, 2, 3]. A measured signal from a random medium, such as optical intensity, has observed spatial and temporal fluctuations. This signal could be used as a probe for characterizing the random medium itself, such as for determining the optical scattering properties of biological tissue, or for imaging an object within the random medium. Alternatively, the random medium could be the communication channel through which an information carrying signal is transmitted to some remote receiver, as is the case with rain in a microwave link and the presence of fog or clouds in a free-space optical link. This thesis is focused on the optical characterization of random media with scattering properties similar to those of biological tissue in the so called "therapeutic window" (600 nm to 1300 nm) wavelength range of the optical spectrum, where scatter dominates absorption.

Many techniques have been investigated for optical imaging in a multiple scattering random medium, and they have been separated into the two broad categories of "coherent" imaging and "incoherent" imaging. Using this categorization, light that propagates through a random medium and is detected at the output is separated into the two components of "coherent" light and "incoherent" light [1]. The "coherent" light is that light which maintains the initial direction, phase, and polarization of the incident light, and the "incoherent" light is all the other scattered light. However, it should be noted that the "incoherent" component of the light from a random medium may still be optically coherent and hence able to interfere with itself or a reference beam, so in this context the notation of "incoherent" can be misleading.

The terms "ballistic" imaging and "diffusive" imaging are often applied to the coherent imaging and incoherent imaging techniques, respectively. These terms arise from using a photon-based picture of light propagating through the random medium, where "ballistic" refers to the un-scattered photons and "diffusive" refers to the multiply-scattered photons. Under sufficient scattering conditions, the photon density can be modeled using a diffusion equation, hence the name diffusive imaging. For a review of these techniques applied to biomedical imaging, see the study by Hebden [4]. Each of these methods have relative advantages and disadvantages.

The principle behind coherent imaging is to image only the un-scattered component of the light and thus form the geometric image of an object, say an absorber, within a scattering random medium. The difficulty arises from trying to gate the coherent or first arriving light that contains the desired information from the undesirable multiply-scattered light. Various techniques used to achieve this are a streak camera [5, 6], an optical Kerr gate [7], and second harmonic generation (SHG) [8]. It is also possible to use holographic techniques, sometimes called a "coherence gate", to achieve the gating of coherent light [9]. The primary disadvantage of the coherent imaging techniques is that the coherent signal itself is very weak and therefore difficult to measure for typical amounts of scatter in an important array of problems. The coherent signal intensity decays exponentially with the total amount of scattering, and is limited to relatively thin scattering samples.

Optical coherence tomography (OCT) is another coherent imaging technique that uses a low coherence interferometer to perform imaging within a scattering medium [10, 11]. In OCT, the internal structure of a scattering medium, such as human skin, is determined by measuring the optical reflections as a function of axial depth and lateral position. The axial resolution is determined by the coherence of the source. A broad bandwidth source with a small coherence length will have a high resolution. The transverse resolution, which is independent of the axial resolution, is determined by the numerical aperture (NA) of the focusing lens, as in optical microscopy. The axial depth of an OCT image is achieved by scanning the optical delay in the reference arm

of the interferometer, but because of the multiple scattering, the currently achievable depth for OCT is limited to a few millimeters [12].

Incoherent imaging measurements can either be performed in the time domain [13, 14, 15] or frequency domain [16, 17, 18, 19]. The time domain techniques apply a short optical pulse to the random medium and then measure the total intensity output as a function of time (and not just the coherent component). Even though the incoherent light intensity is much greater than the coherent intensity, it is still experimentally challenging to measure the temporal output, since both a sensitive and fast detector is required, such as a streak camera. In the frequency domain approach, a continuous wave source is intensity modulated at radio frequencies, and is then applied to the random medium sample. The output intensity is then detected at the same modulation frequency, giving a magnitude and phase measurement relative to the input intensity. It is also interesting to note that a photon density wave [20] propagates through the random medium sample with phase velocity determined by the scattering properties, and is refracted at boundaries of different scattering properties. The frequency domain technique offers advantages over the time domain technique with regards to measurement dynamic range and sensitivity, but less information is obtained in a single frequency measurement than a single time domain measurement, i.e., multiple modulation frequencies are necessary to describe the temporal behavior.

The disadvantage of incoherent imaging over coherent imaging is that, because all of the multiply scattered light is measured, no direct geometric image can be formed from the measurements. An image reconstruction procedure is needed, which is a computationally intensive inverse problem that needs to be solved [21, 22, 23, 24].

When optically coherent light is reflected from a rough surface or transmitted through a random medium, the measured intensity has a grainy appearance of bright and dark spots, which is called speckle. These intensity fluctuations are caused by the interference of many scattered partial waves having a random phase, introduced by the scattering process. Speckle cannot be avoided when the highly coherent light from

a laser is used in any form of random media, and has in fact found many applications [25].

The statistical properties of a rough surface can be determined by using speckle techniques [26, 27, 28]. It has also been shown that the coherence properties of the light used to illuminate the rough surface affects the measured speckle pattern statistics and can used to characterize the surface roughness [29, 30].

Another application of speckle techniques is in the famous astronomical speckle interferometry method of Labeyrie [31]. The random fluctuations of the atmosphere severely limits the resolution of optical telescopes to well below their diffraction limit. Labeyrie's technique allows the diffraction limited intensity autocorrelation of a star to be measured by taking many short-time exposures which contain speckle due to atmospheric turbulence and then processing then to form the desired image. The atmosphere is modeled as being static, but random, for each exposure. A long-time exposure "washes out" the speckle due to the time varying random atmosphere, and also reduces the image resolution.

Laser speckle has also been used to measure the displacement of rough surfaces in an interferometric configuration [32, 33]. Traditionally, to accurately measure displacement, an interferometer usually requires mirrors of high quality with extreme flatness, so it seems surprising that similar information can be obtained with a rough surface. In fact, this area has developed significantly and is usually called electronic speckle pattern interferometry (ESPI), where the displacement, vibration, and stress in a sample with a rough surface can be viewed real-time on a video monitor [34].

1.2 Thesis Outline

This thesis is focused on laser speckle produced from laser light traversing a random medium. As will be shown, important information used to characterize the random medium can be obtained by measuring the intensity correlations of the resultant speckle patterns. Previous investigations into speckle correlations [35, 36, 37, 38,

39, 40] have focused on second-order intensity correlations. One of the key contributions of this work is the application of third-order correlations to the study of speckle from random media [41]. This allows the temporal response of a random medium to be obtained independent of a forward model. Using the measurement technique proposed, data suitable for application in optical diffusion tomography (ODT) can be readily obtained over very large bandwidths.

Third-order correlations have been investigated in the past for several different applications. Gamo [42, 43] proposed using a third-order correlation to extend the information obtainable from the intensity interferometer of Hanbury-Brown and Twiss [44] for the analysis of optical spectrum profiles. Lohmann, Weigelt, and Wirnitzer [45] applied a third-order correlation in a speckle masking technique for astronomical applications, which provided for stellar imaging and extended the technique of Labeyrie [31]. In a deterministic application, Blount and Klauder [46] proposed a third-order correlation technique for determining the intensity pulse shape from a short-pulse laser. They established that third-order correlations are sufficient to fully characterize the intensity pulse shape.

Chapter 2 discusses the theoretical background of speckle from random media. This includes the statistics of a speckle pattern, the formation of speckle in an imaging system, and effects that a random medium have on speckle correlations. Also discussed in this chapter, is the photon transport model of light propagation in a random medium and the diffusion approximation of this model, as well as the bispectral techniques of third-order correlations. In Chapter 3, the experimental technique used for measuring the speckle correlations from a random medium are discussed, together with the experimental setup and its characterization. Chapter 4 presents the experimental results. In Chapter 5, a speckle interferometer proposal for characterizing random media is introduced, and the conclusions are given in Chapter 6.

2. THEORY OF SPECKLE FROM RANDOM MEDIA

2.1 Speckle Theory

Speckle is the random intensity distribution observed when a random medium is imaged using highly coherent light from, for example, a laser. The random medium could be the rough surface of ground-glass, or it could be a volume of discrete scattering particles. The key process in the formation of speckle is that the random medium introduces a random phase onto the scattered partial waves that are summed at some observation point and hence produces a random intensity due to interference effects.

The statistical description of speckle was originally developed by Goodman [47] and Dainty [48]. Their model, which highlights the important concepts in speckle, was developed by considering monochromatic light that is reflected from (or transmitted through) a rough surface such as that of ground-glass. As will be shown later, this model is also very well suited to describing the field from a random medium consisting of discrete scatterers in a finite volume. In this model, the complex amplitude of the field at a point in space can be expressed as a random phasor sum. Each elementary phasor in this sum is the randomly-phased partial wave scattered from the rough surface that arrives at the observation point. The complex amplitude E of the field at some observation point is

$$E = \frac{1}{\sqrt{N}} \sum_{k=1}^{N} A_k \exp(-j\phi_k), \tag{2.1}$$

where A_k is the random magnitude of the k^{th} elementary random phasor and ϕ_k is its random phase. The statistical properties of the complex amplitude in (2.1) are determined by the statistical properties of the elementary random phasors. The assumptions made by Goodman [47], which have been found to be valid in most practical situations, are: (a) the k^{th} elementary random magnitude A_k and random phase

ϕ_k are statistically independent and independent of all other random magnitudes and phases, and (b) the random phase ϕ_k is uniformly distributed over $-\pi$ to π. Assumption (b) will be valid when the surface roughness is greater than a wavelength. The random phasor sum model, with these assumptions, can be interpreted as a random walk in the complex plane, where the magnitude of each step is independent of its direction, and there is equal probability of taking a step in any particular direction.

For a large number of elementary random phasors, the limit $N \to \infty$ can be used, allowing the central limit theorem to be applied [47]. Under assumptions (a) and (b), the probability density function for the complex amplitude given in (2.1), which can be expressed by the real and imaginary components of $E = E^r + jE^i$, is a zero-mean Gaussian of the form

$$p_{ri}(E^r, E^i) = \frac{1}{2\pi\sigma^2} \exp\left[-\frac{1}{2}\frac{(E^r)^2 + (E^i)^2}{\sigma^2}\right], \tag{2.2}$$

where

$$\sigma^2 = \lim_{N\to\infty} \frac{1}{N} \sum_{k=1}^{N} \frac{\langle A_k^2 \rangle}{2}. \tag{2.3}$$

The real and imaginary components of the complex amplitude have zero means, $\langle E^r \rangle = \langle E^i \rangle = 0$, equal variances $\langle (E^r)^2 \rangle = \langle (E^i)^2 \rangle = \sigma^2$, and are uncorrelated $\langle E^r E^i \rangle = 0$. The brackets $\langle \cdots \rangle$ represent the ensemble average over all statistically equivalent rough surfaces. Under these conditions, the statistics of the random complex amplitude described by the joint probability density function of (2.2) are said to be zero-mean circular complex Gaussian.

For most experiments performed at optical frequencies, the wave intensity is usually directly measured. Therefore, it is useful to determine the statistics of the intensity (and total phase) at the observation point. The real and imaginary components of the field are related to the intensity I and total phase θ by the relations

$$\begin{aligned} E^r &= \sqrt{I}\cos\theta \\ E^i &= \sqrt{I}\sin\theta. \end{aligned} \tag{2.4}$$

Using the standard techniques for transformations of random variables [49], the marginal probability density function for intensity is calculated using (2.2) and (2.4)

$$p_I(I) = \frac{1}{\mu_I} \exp(-I/\mu_I), \quad I \geq 0, \tag{2.5}$$

where $\mu_I = 2\sigma^2$ is the mean intensity. The marginal probability density function for the total phase is given by

$$p_\theta(\theta) = \frac{1}{2\pi}, \quad -\pi \leq \theta < \pi. \tag{2.6}$$

Thus, it can be seen that under assumptions (a) and (b), the statistics for the field are zero-mean circular complex Gaussian, for the intensity they are negative exponential, and for the total phase they are uniform over $-\pi$ to π. Such a speckle pattern is said to have "fully developed" statistics [47].

In some experimental situations, the assumptions (a) and (b) may not hold, such as when the random phase is not uniformly distributed over $-\pi$ to π, or the number of scattered partial waves N is small and the application of the central limit theorem is suspect. These situations can lead to non-Gaussian speckle, which I shall not discuss here, but is an area that has been investigated by several authors [50, 51, 52].

2.1.1 Speckle Formation in Imaging Systems

The previous section discussed the statistical properties of speckle, based on a random phasor sum model, but did not specify how a speckle pattern can be formed and accurately measured in the laboratory. The formation of a speckle pattern can be conveniently modeled under the Fresnel approximation of scalar diffraction theory [53].

The field in the image plane, $E_{\text{im}}(x, y)$, is related to the field in the object plane, $E_{\text{ob}}(\xi, \eta)$, by the superposition integral of

$$E_{\text{im}}(x, y) = \iint_{-\infty}^{\infty} \mathrm{d}\xi \mathrm{d}\eta \; E_{\text{ob}}(\xi, \eta) h(x, y; \xi, \eta), \tag{2.7}$$

under the assumption that the imaging of the field is a linear process, which is the case assumed here. The function $h(x, y; \xi, \eta)$ is the spatial impulse response or point

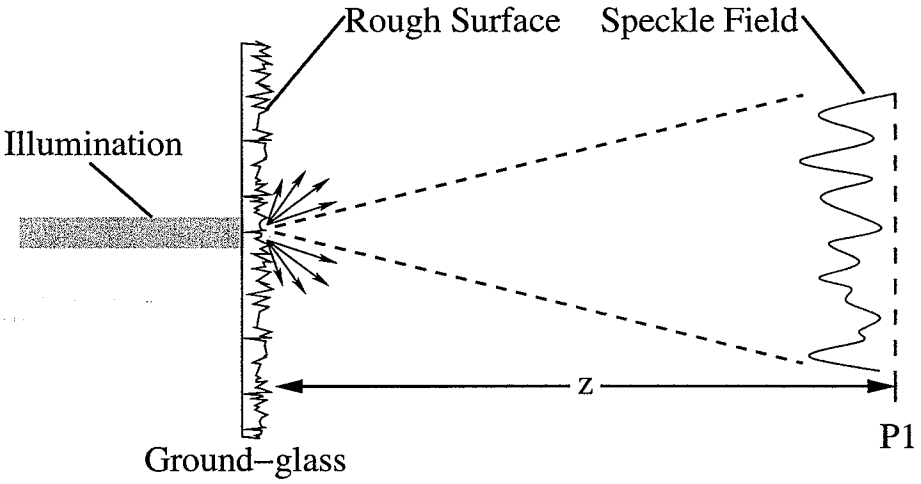

Fig. 2.1. The free-space propagation geometry used to demonstrate the formation of a speckle pattern under the Fresnel approximation of scalar diffraction theory. The propagation distance between the object plane (rough surface) and image plane of $P1$ is given by z.

spread function (PSF) of the optical system between the object plane and image plane. The PSF describes the field response at location (x, y) in the image plane due to a delta-function at location (ξ, η) in the object plane. In some circumstances the PSF is space-invariant, which means that it can be expressed in the form $h(x - \xi, y - \eta)$, and the superposition integral of (2.7) becomes a convolution integral. In this case the optical system is also called isoplanatic [54].

The simplest imaging geometry that can be used in the formation of a speckle pattern is that of free-space propagation. Under the Fresnel approximation, the PSF $h(x, y; \xi, \eta)$ for free-space propagation to be used in the superposition integral of (2.7) is given by [53]

$$h(x, y; \xi, \eta) = \frac{1}{j\lambda z} \exp\left[j\frac{\pi}{\lambda z}\left((x - \xi)^2 + (y - \eta)^2\right)\right], \tag{2.8}$$

where z is the propagation distance and λ is the wavelength of light used. Figure 2.1 shows the geometry for free-space propagation, where the rough surface of a ground-glass sample is illuminated in a transmission geometry. The speckle field is formed

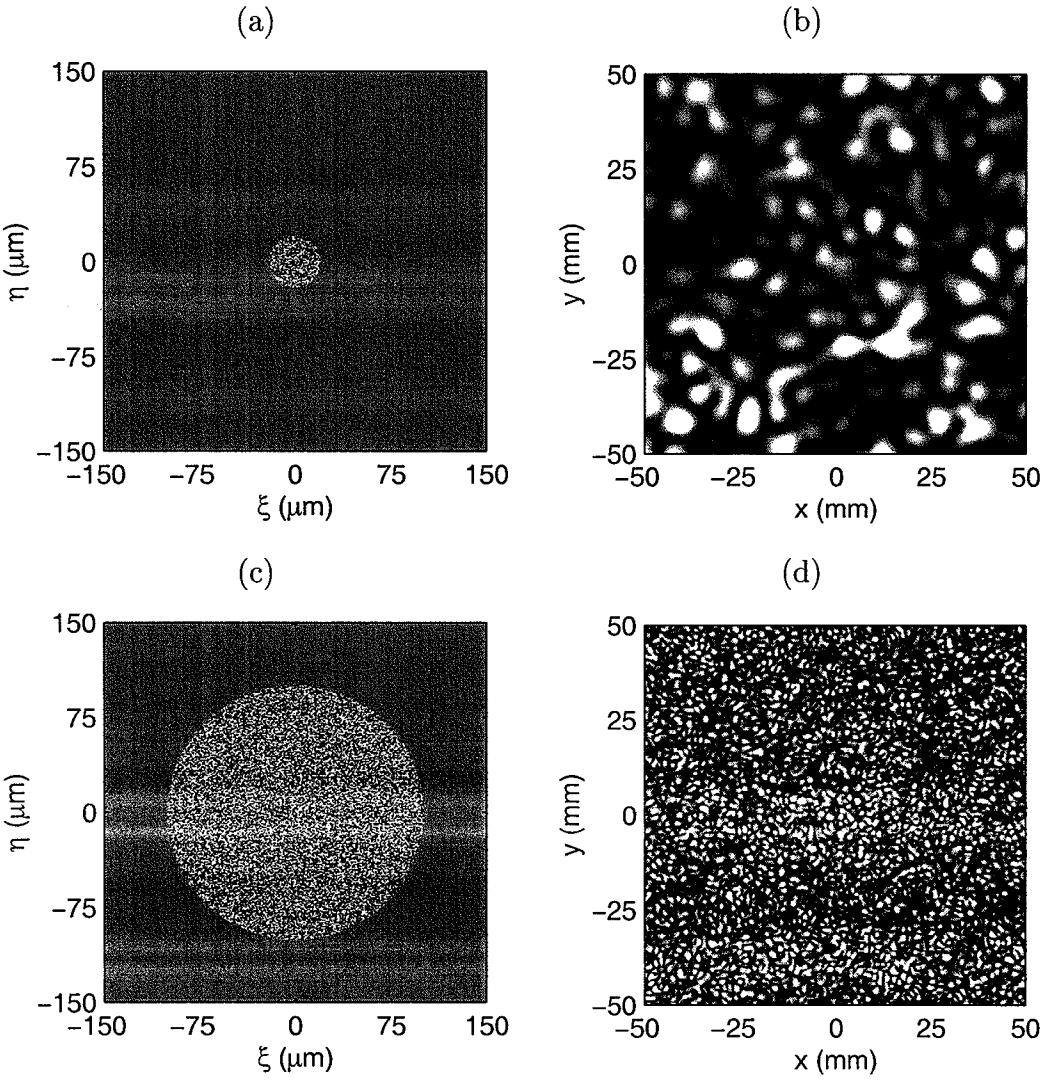

Fig. 2.2. (a) A plot of the random phase of the uniform magnitude object field with a diameter of 40 μm. (Scaled such that $-\pi$ maps to black and π maps to white). (b) A plot of the calculated speckle intensity observed in the image plane at a distance $z = 250\,\text{mm}$ from the object plane for the geometry of Fig. 2.1. (c), (d) Same as (a) and (b) except the object field has a diameter of 200 μm. The wavelength for all cases is $\lambda = 850\,\text{nm}$.

at the image plane $P1$, a propagation distance z from the object plane at the rough surface.

The field in the image plane was calculated numerically by solving (2.7) with the PSF of (2.8) and using a fast Fourier transform (FFT) with the MATLAB software

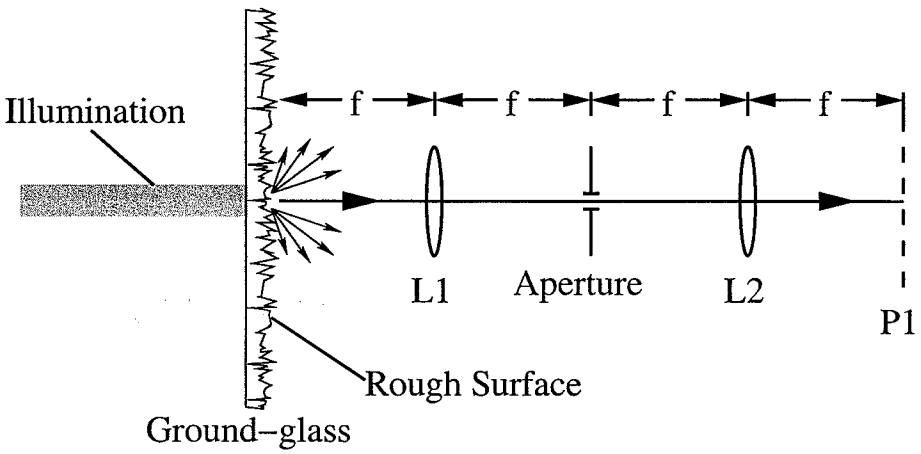

Fig. 2.3. The 4-f spatial filter (telescope) imaging geometry. The lenses $L1$ and $L2$ both have a focal length of f, and the aperture located at the Fourier plane has a diameter of D. The image plane at $P1$ is a spatially filtered version of the object plane at the rough surface.

package. The results are shown in Fig. 2.2, for the incident illumination having two different finite supports. A circular beam of diameter 40 μm with a uniform magnitude and random phase over $-\pi$ to π was used for illumination in the object plane field and is shown in Fig. 2.2(a), and the resultant image plane intensity at a distance $z = 250\,\text{mm}$ away is shown in Fig. 2.2(b). In Figs. 2.2(c) and (d), the same results are shown, except the diameter of the circular beam used for illumination is 200 μm.

An alternative to the free-space geometry of Fig. 2.1 for forming a speckle pattern is to use an imaging geometry. One commonly used geometry is the 4-f spatial filter or telescope configuration shown in Fig. 2.3. The PSF for this imaging geometry, calculated under the Fresnel approximation of scalar diffraction theory, is given by [53]

$$h(x,y;\xi,\eta) = \frac{\pi D}{2\lambda^2 f^2}\text{jinc}\left\{\frac{D}{2\lambda f}\sqrt{(x-\xi)^2+(y-\eta)^2}\right\}, \tag{2.9}$$

where f is the focal length of lenses $L1$ and $L2$, and D is the diameter of the aperture at the Fourier plane. The function $\text{jinc}(x)$ (sometimes called "besinc(x)") is defined by

$$\text{jinc}(x) = 2\frac{J_1(2\pi x)}{2\pi x}, \tag{2.10}$$

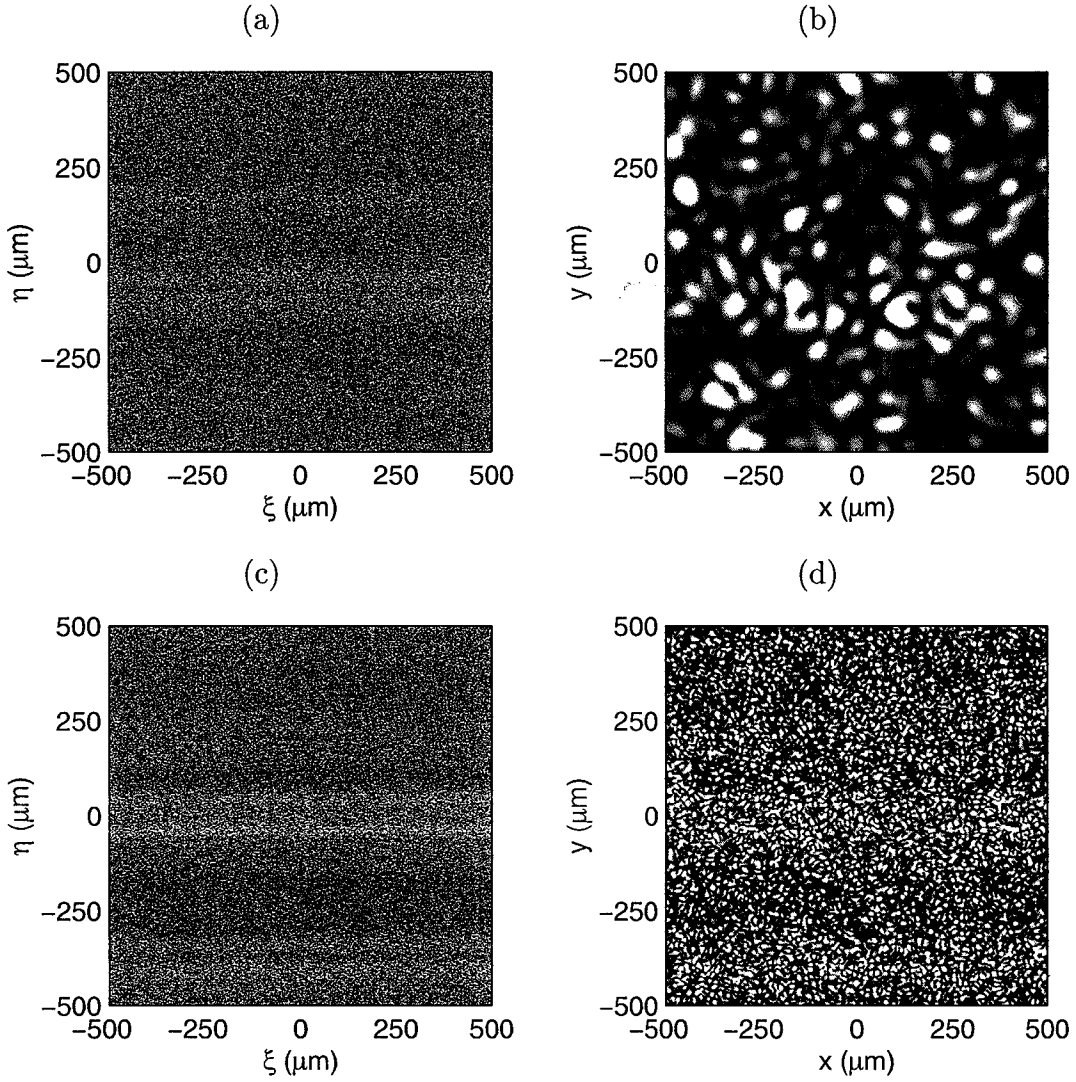

Fig. 2.4. (a) The random phase (uniform over $-\pi$ to π). The object field has a uniform magnitude. (b) The speckle intensity at the image plane of the geometry of Fig. 2.3 calculated using $f = 50\,\text{mm}$ and $D = 1\,\text{mm}$. (c), (d) As for (a) and (b), except with $D = 5\,\text{mm}$. All calculations used a wavelength of $\lambda = 850\,\text{nm}$.

where $J_1(x)$ is a Bessel function of the first kind and order one.

The object plane field for the imaging geometry of Fig. 2.3 was also calculated by solving (2.7) with the PSF of (2.9), again by using a FFT within MATLAB, with the results shown in Fig. 2.4. A $500\,\mu\text{m} \times 500\,\mu\text{m}$ region in the object plane with a uniform magnitude and a random phase (over $-\pi$ to π) was imaged using a focal length of

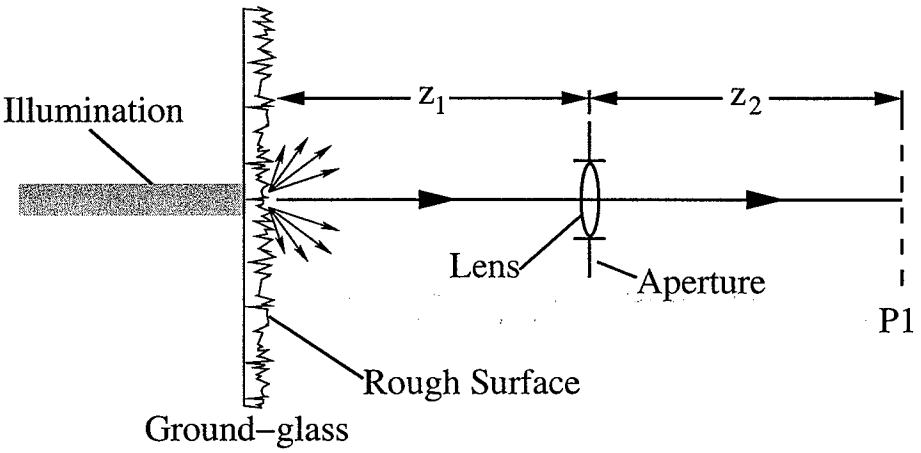

Fig. 2.5. The single lens imaging geometry used to form a speckle pattern in the image plane at $P1$. The lens has a focal length of f, and the aperture has a diameter of D. The PSF of this imaging geometry is given by (2.12).

$f = 50\,\text{mm}$ for lenses $L1$ and $L2$, for two different aperture diameters of $D = 1\,\text{mm}$ and $D = 5\,\text{mm}$. Figure 2.4(a) shows the random phase in the object plane, and Fig. 2.4(b) shows the resultant image plane intensity for $D = 1\,\text{mm}$. Figure 2.4(c) shows the random phase in the object plane, and Fig. 2.4(d) shows the resultant image plane intensity for $D = 5\,\text{mm}$.

It is also possible to form a speckle pattern using the single lens imaging geometry shown in Fig. 2.5. In this configuration, the distances z_1 and z_2, which are the distances from the object plane to the lens and from the lens to the image plane respectively, are chosen to satisfy the geometric optics imaging condition

$$\frac{1}{z_1} + \frac{1}{z_2} = \frac{1}{f}, \tag{2.11}$$

where f is the focal length of the lens. The lens has a finite diameter of D, which is facilitated by the aperture. The PSF of this imaging system under the Fresnel approximation of scalar diffraction theory for the unity magnification case of $z_1 = z_2 = 2f$ is [53]

$$h(x, y; \xi, \eta) = \frac{\pi D}{8\lambda^2 f^2} \exp\left[j\frac{\pi}{2\lambda f}\left(x^2 + y^2\right)\right] \exp\left[j\frac{\pi}{2\lambda f}\left(\xi^2 + \eta^2\right)\right] \times$$

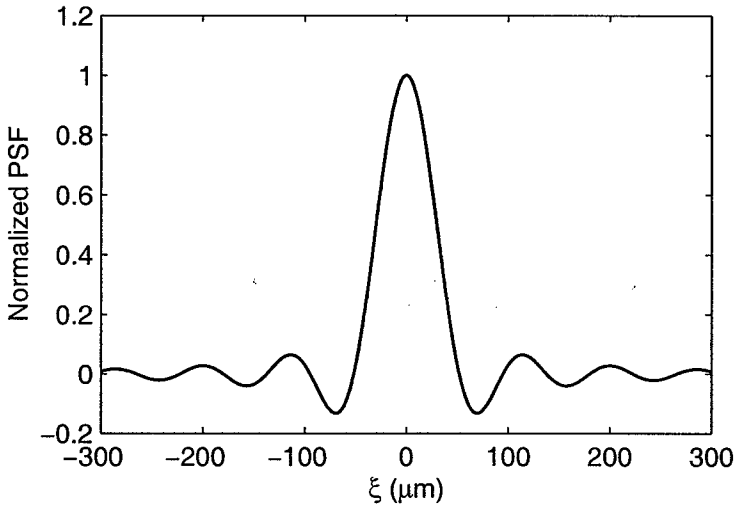

Fig. 2.6. The PSF of (2.9) given by $h(0,0;\xi,0)$, normalized to unity for the imaging geometry of Fig. 2.3 with $f = 50\,\text{mm}$, $D = 1\,\text{mm}$, and $\lambda = 850\,\text{nm}$.

$$\text{jinc}\left\{\frac{D}{4\lambda f}\sqrt{(x-\xi)^2+(y-\eta)^2}\right\}. \tag{2.12}$$

In practice, the PSF will not be exactly of the form given in (2.12) because the limiting aperture of diameter D is physically placed next to the lens and not at the lens plane. This will lead to a small error that is neglected.

It is important to reconcile the statistics of the field produced in the image plane by an imaging system with the statistics of the object plane field. In principle, this can be achieved by transforming the statistics of $E_{\text{ob}}(\xi,\eta)$ using (2.7). However, in practice, this is a very difficult problem and it is usually approximated [47]. The field in the image plane $E_{\text{im}}(x,y)$ can be assumed Gaussian when the spatial correlation of $E_{\text{ob}}(\xi,\eta)$ in the object plane is very small compared with the resolving power of the PSF. In this case, the field at a particular point in the image plane will be a summation of many independent fields from the object plane weighted by the PSF, allowing the central limit theorem to be applied. This is also the basis of the random phasor sum model. As an example, the PSF given by (2.9) of the imaging geometry of Fig. 2.3 is normalized to unity and plotted in Fig. 2.6. This curve shows the weighting distribution applied to the field in the object plane that contributes to the field at a

single point in the image plane. Therefore, so long as the spatial correlation of the object plane field is very small compared with $100\,\mu$m, many independent samples will contribute to the field in the image plane and thus it will be Gaussian.

For a ground-glass sample, the correlation statistics of the object field can be related to the surface roughness statistics. This allows the statistics of the speckle field to exploited in measuring the surface roughness of ground-glass [55].

For the case of a random medium that consists of a volume of discrete scatterers, the object field spatial correlation properties are a little more difficult to calculate. However, Shapiro [56] has calculated an expression based on the assumption that scattering paths of the partial waves contributing to the total field at a particular point are uncorrelated. The resulting field spatial correlation for a random medium is

$$\langle E(r+\Delta r)E^*(r)\rangle = \exp(-\Delta r/2l)\frac{\sin(k\Delta r)}{k\Delta r}, \tag{2.13}$$

where r is a location on the random medium, Δr is a small distance away, l is the scattering mean free path, and $k = 2\pi/\lambda$. From this result, it can be seen that the spatial correlation is only significant over a range equal to a wavelength (as determined from the sinc function part of this expression). Thus, with the imaging conditions of the PSF shown in Fig. 2.6, the field from a random medium at a wavelength of $\lambda = 850\,$nm will give many contributions to the field in the object plane, which can then be expected to be Gaussian.

2.1.2 Speckle Size

The speckle size in the image plane is determined by the spatial correlation of the image plane field. Using the superposition integral of (2.7), the image plane field correlation is given by

$$\langle E_{\rm im}(x_1,y_1)E^*_{\rm im}(x_2,y_2)\rangle = \int\!\!\int_{-\infty}^{\infty} {\rm d}\xi{\rm d}\eta \int\!\!\int_{-\infty}^{\infty} {\rm d}\xi'{\rm d}\eta'\; h(x_1,y_1;\xi,\eta)h^*(x_2,y_2;\xi',\eta')\times \langle E_{\rm ob}(\xi,\eta)E^*_{\rm ob}(\xi',\eta')\rangle. \tag{2.14}$$

As can be seen in (2.14), the field correlation in the image plane is dependent upon the field correlation in the object plane. When the object plane correlation is very small compared with the width of the PSF, the object plane correlation function can be approximated as a delta function in the form [47]

$$\langle E_{\rm ob}(\xi,\eta)E^*_{\rm ob}(\xi',\eta')\rangle \simeq \langle |E_{\rm ob}(\xi,\eta)|^2\rangle \delta(\xi-\xi',\eta-\eta'). \tag{2.15}$$

To simplify (2.14) further, it is assumed that the PSF is space-invariant, as given by the PSF of (2.9), for example. Also, if the object plane mean intensity is constant (i.e., the object plane statistics are stationary), then defining the object plane mean intensity by $\langle I_{\rm ob}\rangle = \langle |E_{\rm ob}(\xi,\eta)|^2\rangle$, (2.14) can be written as

$$\langle E_{\rm im}(x_1,y_1)E^*_{\rm im}(x_2,y_2)\rangle = \langle I_{\rm ob}\rangle \int\!\!\int_{-\infty}^{\infty} {\rm d}\xi{\rm d}\eta\; h(x_1-\xi,y_1-\eta)h^*(x_2-\xi,y_2-\eta). \tag{2.16}$$

It is convenient to make the variable substitutions of

$$\begin{aligned} x_1 &= x+\Delta x, \qquad & x_2 &= x \\ y_1 &= y+\Delta y, \qquad & y_2 &= y \end{aligned} \tag{2.17}$$

and by performing a change of integration variables of

$$\begin{aligned} \xi' &= x+\Delta x-\xi \\ \eta' &= y+\Delta y-\eta \end{aligned} \tag{2.18}$$

allows (2.16) to be expressed as

$$\langle E_{\rm im}(x+\Delta x,y+\Delta y)E^*_{\rm im}(x,y)\rangle = \langle I_{\rm ob}\rangle \int\!\!\int_{-\infty}^{\infty} {\rm d}\xi'{\rm d}\eta'\; h(\xi',\eta')h^*(\xi'-\Delta x,\eta'-\Delta y). \tag{2.19}$$

The result of (2.19) shows that for a spatially-invariant PSF, a constant mean in the object plane, and for the object plane field correlation being very small so that it can be accurately approximated by a delta function, then the spatial correlation of the image plane field is determined by the PSF of the imaging optics. A more general analysis, such as when these conditions do not hold, has been treated in greater detail by several authors [57, 58, 59, 60, 61, 62, 63].

The spatial correlation of the speckle intensity can be calculated from (2.19). When the image plane field is assumed a circular complex Gaussian random process

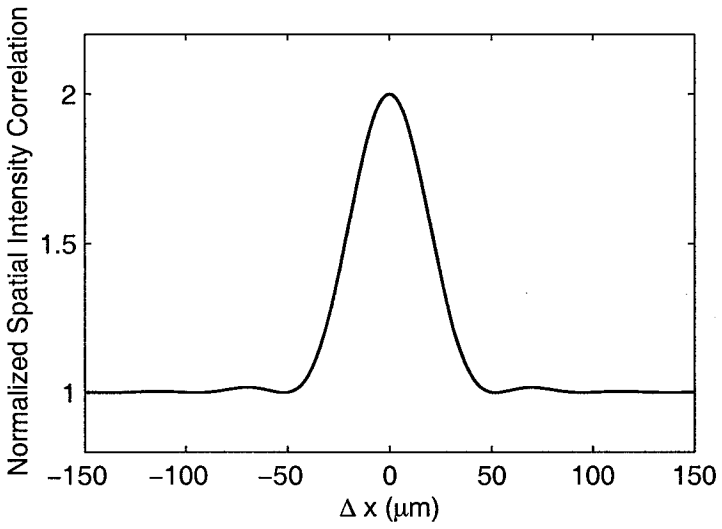

Fig. 2.7. The normalized intensity spatial correlation of (2.20) for the imaging geometry of Fig. 2.3 with $f = 50\,\text{mm}$, $D = 1\,\text{mm}$, and $\lambda = 850\,\text{nm}$.

[47], then the relation of $\langle I_1 I_2 \rangle = \langle E_1 E_1^* E_2 E_2^* \rangle = \langle I_1 \rangle \langle I_2 \rangle + |\langle E_1 E_2^* \rangle|^2$ can be used. For the imaging geometry of Fig. 2.3, with a PSF given by (2.9), and after some algebra, the intensity spatial correlation is calculated from (2.16) to give

$$\langle I_{\text{im}}(x + \Delta x, y + \Delta y) I_{\text{im}}(x, y) \rangle = \langle I_{\text{im}} \rangle^2 \left[1 + \left| \text{jinc} \left\{ \frac{D}{2\lambda f} \sqrt{\Delta x^2 + \Delta y^2} \right\} \right|^2 \right], \quad (2.20)$$

where

$$\langle I_{\text{im}} \rangle = \langle I_{\text{ob}} \rangle \iint_{-\infty}^{\infty} \text{d}\xi' \text{d}\eta' \; |h(\xi', \eta')|^2. \quad (2.21)$$

A normalized plot of (2.20) is given in Fig. 2.7 for the imaging geometry of Fig. 2.3 with $f = 50\,\text{mm}$, $D = 1\,\text{mm}$, and a wavelength of $\lambda = 850\,\text{nm}$. The width of this plot gives a measure of the mean speckle size in a speckle intensity pattern. The mean speckle size is the distance from the origin to the first minimum of spatial intensity correlation function, and for the example given in Fig. 2.7, the mean speckle size is approximately $50\,\mu\text{m}$.

2.2 Random Media

The rough surface of a ground-glass sample serves as a very good model to develop the fundamental concepts of speckle and also speckle formation through an imaging system. The goal of this study is to use these speckle techniques to characterize random media, which have a larger range of applications and have more diverse properties than a rough surface.

There are several important length scales used as parameters to describe a random medium and the scattering regime to which it belongs. These are: (i) the wavelength of light λ; (ii) the scattering mean free path l, which is the average distance between scatterers; (iii) the transport mean free path l^*, which is the mean distance over which the initial direction of the incident light is completely randomized; and (iv) the physical size of the random medium sample L, which could be the thickness of a slab, for example. For isotropic point scatterers, l and l^* are equal, but in general it requires several scattering events to randomize a partial wave's direction, and therefore it is typical for $l^* > l$.

There are two important scattering limits of weak-scattering where $\lambda \ll l$, and strong-scattering where $\lambda \sim l$ [39]. In the strong-scattering limit, localization effects [35, 64] can be observed. In the weak-scattering limit, there is still a very large amount of multiple scattering occurring within the random medium, contrary to what the name may imply. The samples used in this study are in the weak-scattering limit, and have $L \gg l^*$ which is called the diffusive regime. This is an important scattering regime, to which biological tissue in the near-IR wavelength range belongs.

(There is also a fifth length scale, a, the diameter of a scattering particle, which is a factor in the relationship between l and l^* through Mie scattering theory [1]. The samples used for this study have scattering particles with $a \ll \lambda$, which is called the Rayleigh scattering limit where the scattering cross-section has a λ^{-4} dependence [1]. A sixth length scale of l_{abs} which is the length scale over which absorption occurs could

also be defined. In most practical situations, $l_{\text{abs}} > L$, therefore allowing absorption effects to be neglected.)

2.2.1 Random Phasor Sum Model

When a monochromatic field illuminates a random medium, the total field at a particular point after traversing the medium can be expressed as the superposition of many scattered partial waves. Each of these partial waves has a random magnitude and a random phase relative to the incident wave, thus allowing the total field to be described by a random phasor sum. This random phasor sum model is the foundation for the statistical description of speckle discussed by Goodman [47], and was developed for light reflected from (or transmitted through) a rough surface, but applies equally to a random medium consisting of many scatterers.

Using the random phasor sum model, we obtain a convenient and general expression for the scattered field from a time invariant random medium. We assume a scalar model for the scattered electric field which physically means we consider only a single linear polarization, however it is possible to extend this approach to a generalized vectorial model.

At some specified source location on the random medium, the applied monochromatic electric field of frequency ν is

$$e_{\text{in}}(t) = E_i \exp(j2\pi\nu t) \ + \text{c.c.}, \tag{2.22}$$

where E_i is the complex amplitude and c.c. represents the complex conjugate. Then, at some specified detector location, the resultant electric field is represented as

$$e_{\text{out}}(t) = E_o(\nu) \exp(j2\pi\nu t) \ + \text{c.c.}, \tag{2.23}$$

where the output electric field complex amplitude, $E_o(\nu)$, is a random variable dependent upon the frequency of the applied field. The statistical properties of the random

medium can be studied by determining the statistics of $E_o(\nu)$. The random phasor sum model represents $E_o(\nu)$ as

$$E_o(\nu) = \frac{1}{\sqrt{N}} \sum_{k=1}^{N} A_k \exp\left[-j\phi_k(\nu)\right], \tag{2.24}$$

where A_k is the random magnitude and $\phi_k(\nu)$ is the random phase of the k^{th} elementary partial wave. The number of elementary partial waves is given by N, which is assumed to be large such that the limit of $N \to \infty$ can be used. The random magnitudes A_k are modeled independent of frequency, because we have assumed the scattering cross-sections of the scatterers do not vary with small changes in frequency, and can therefore be considered frequency independent. The random phase, on the other hand, is very sensitive to small changes in frequency. Each random phase $\phi_k(\nu)$ is modeled as an accumulated phase from traversing the k^{th} path whose random "time of flight" is t_k, resulting in

$$\phi_k(\nu) = 2\pi\nu t_k. \tag{2.25}$$

For the random phasor sum model to be practical for gaining insight into the response of a random medium, several assumptions need to be made about the statistical properties of the scattered partial waves. As did Goodman [47], we assume: (i) the random magnitudes A_k are statistically independent and identically distributed; (ii) the random phases $\phi_k(\nu)$ are statistically independent and uniformly distributed over the interval of $-\pi$ to π, when taken modulo 2π; (iii) the random magnitude A_k and random phase $\phi_k(\nu)$ of each elementary partial wave are statistically independent. These assumptions are equivalent to specifying that the random paths of each partial wave through the random medium are all statistically equivalent and statistically independent.

Assumption (ii) requires that the random phase be uniformly distributed when taken modulo 2π. In (2.25) we relate the random phases to the random (independent and identically distributed) times of flight t_k, which in general will not be uniformly distributed, but have a probability density function that we denote by $p(t)$. As long as the width of $p(t)$ is broad compared with $1/\nu$, the random phases will be

approximately uniform when taken modulo 2π. For our study, the optical frequency ν is approximately $3.5 \times 10^{14}\,\mathrm{s}^{-1}$ (a wavelength of 850 nm), and $p(t)$ has a width on the order of $10^{-10}\,\mathrm{s}$ or greater. Thus the random phase will cover many multiples of 2π and be approximately uniform when taken modulo 2π, as required.

2.2.2 Statistics of Scattered Field

Under the assumptions (i)–(iii) listed above, the output field $E_o(\nu)$ from a random medium, measured at a single frequency ν, and modeled by the random phasor sum of (2.24) has first-order statistics that are zero-mean circular complex Gaussian [47]. Writing $E_o(\nu) = x + jy$, the probability density function for the real and imaginary parts is

$$p_{xy}(x,y) = \frac{1}{2\pi\sigma^2} \exp\left(-\frac{1}{2}\frac{x^2+y^2}{\sigma^2}\right), \tag{2.26}$$

where

$$\sigma^2 = \frac{1}{N}\sum_{k=1}^{N} \frac{\langle A_k^2 \rangle}{2}. \tag{2.27}$$

The brackets $\langle \cdots \rangle$ represent the ensemble average over all possible scatterer configurations of the random medium. By assuming that the random magnitudes A_k are identically distributed, the expression in (2.27) further simplifies to $\sigma^2 = \langle A^2 \rangle / 2$. The output intensity from a random medium is given by $I(\nu) = |E_o(\nu)|^2$, whose ensemble average is calculated from (2.26) to give $\langle I(\nu) \rangle = 2\sigma^2$. This result shows that by assuming the random magnitudes are frequency independent (for small frequency variations) along with the assumptions (i)–(iii) implies that the ensemble average output intensity is also frequency independent, namely

$$\langle I \rangle = \langle A^2 \rangle. \tag{2.28}$$

Only limited information about the scattering properties of the random medium can be obtained from knowing the first-order statistics for the field from a random medium, such as determining that the assumptions (i)–(iii) for the statistics of the scattered partial waves are valid leading to fully-developed speckle statistics [47].

More information, specifically the temporal response of a random medium as will be shown in this study, can be obtained by determining the correlations between the scattered fields measured at two or more different frequencies. Therefore knowledge about the higher-order statistics of the field is required.

Under the assumptions (i)–(iii) described above, the statistics for the set of scattered fields $E_o(\nu_1), E_o(\nu_2), \ldots, E_o(\nu_M)$ measured at different frequencies are jointly zero-mean circular complex Gaussian. The development of this result is presented in Appendix A. If the output fields measured at M discrete frequencies are written in the form of a random vector of size M,

$$\mathbf{z} = \begin{bmatrix} E_o(\nu_1) \\ E_o(\nu_2) \\ \vdots \\ E_o(\nu_M) \end{bmatrix}, \tag{2.29}$$

then the probability density function for the random vector $\mathbf{z}$ has the form

$$p_z(\mathbf{z}) = \frac{1}{\pi^M |C_z|} \exp\left(-\mathbf{z}^H C_z^{-1} \mathbf{z}\right), \tag{2.30}$$

where $\mathbf{z}^H$ is the Hermitian transpose of $\mathbf{z}$ and C_z is the complex covariance matrix whose $(i,j)^{\text{th}}$ element is given by $[C_z]_{i,j} = \langle E_o(\nu_i) E_o^*(\nu_j) \rangle$. In general, circular complex Gaussian statistics are convenient because high-order moments can be easily evaluated using the Gaussian moment theorem of Reed [65]. This theorem enables high-order moments to be expressed as a sum of products of second-order moments, which are the elements of C_z, and is discussed in Appendix B.

2.2.3 Field and Intensity Correlations

The scattered partial waves in a random medium have a distribution for the times of flight that we denote by the probability density function $p(t)$. Let the spread in the times of flight distribution be approximately Δt. The output field $E_o(\nu)$ will become uncorrelated with the output field $E_o(\nu + \Delta\nu)$ when the change in frequency $\Delta\nu$ satisfies the condition of $\Delta\nu \Delta t \sim 1$. When this condition occurs, the difference between the accumulated phase of the two fields will be approximately random over

2π, hence leading to de-correlation. In fact, it was shown by Genack [66, 67] that the second-order correlation between these two fields at different frequencies is related to the Fourier transform of $p(t)$. Here we shall develop the expression for the field second-order correlation for a random medium, utilizing the assumptions (i)–(iii).

Using the random phasor sum model for the scattered field of (2.24), we write the output field at frequency $\nu + \Delta\nu$ as

$$E_o(\nu + \Delta\nu) = \frac{1}{\sqrt{N}} \sum_{k=1}^{N} A_k \exp\left[-j\phi_k(\nu + \Delta\nu)\right], \tag{2.31}$$

where the random phase of the k^{th} elementary partial wave is given by (2.25), as $\phi_k(\nu + \Delta\nu) = 2\pi(\nu + \Delta\nu)t_k$. Here, t_k represents the random time of flight for the k^{th} partial wave. Similarly, we write the output field at frequency ν as

$$E_o(\nu) = \frac{1}{\sqrt{N}} \sum_{i=1}^{N} A_i \exp\left[-j\phi_i(\nu)\right], \tag{2.32}$$

with the random phase of the i^{th} elementary partial wave of $\phi_i(\nu) = 2\pi\nu t_i$. Substituting these two random phasor sum expressions for the output fields into the field second-order correlation expression gives

$$\langle E_o(\nu + \Delta\nu)E_o^*(\nu)\rangle = \frac{1}{N} \sum_{k=1}^{N} \sum_{i=1}^{N} \langle A_k A_l \exp[-j\phi_k(\nu + \Delta\nu) + j\phi_i(\nu)]\rangle . \tag{2.33}$$

By utilizing the statistical independence of the random magnitudes and random phases, and separating the summation into the two cases of $k = i$ and $k \neq i$ results in

$$\begin{aligned} \langle E_o(\nu + \Delta\nu)E_o^*(\nu)\rangle = {} & \frac{1}{N} \sum_{k=1}^{N} \langle A_k^2\rangle \langle \exp(-j2\pi\Delta\nu t_k)\rangle + \\ & \frac{1}{N} \sum_{k=1}^{N} \sum_{\substack{i=1 \\ i\neq k}}^{N} \langle A_k\rangle\langle A_i\rangle \langle \exp(-j\phi_k(\nu + \Delta\nu)\rangle \langle \exp(j\phi_i(\nu)\rangle \end{aligned} \tag{2.34}$$

Since the random phase is assumed uniformly distributed over $-\pi$ to π, the second summation of (2.34) is zero. Also, the elementary random magnitudes A_k are assumed to be identically distributed, as are the random times of flight t_k. This simplifies the expression for the field second-order correlation to

$$\langle E_o(\nu + \Delta\nu)E_o^*(\nu)\rangle = \langle A^2\rangle \langle \exp(-j2\pi\Delta\nu t)\rangle. \tag{2.35}$$

By definition, the expected value of the exponential term in (2.35) over the probability density function p(t) for the random times of flight is

$$\langle \exp(-j2\pi\Delta\nu t) \rangle = \int_{-\infty}^{\infty} \mathrm{d}t \; p(t) \exp(-j2\pi\Delta\nu t), \tag{2.36}$$

which can be easily identified as $P(\Delta\nu)$, the Fourier transform of $p(t)$. Finally, using the result of (2.28), where $\langle A^2 \rangle = \langle I \rangle$ (the ensemble average intensity), gives the desired expression for the field second-order correlation

$$\langle E_o(\nu + \Delta\nu) E_o^*(\nu) \rangle = \langle I \rangle P(\Delta\nu). \tag{2.37}$$

Typical random media in the diffusion regime, such as the samples used in this study, have a spread in the times of flight distribution in the range of $\Delta t = 0.1 \sim 1.0\,\mathrm{ns}$, hence the frequency bandwidth after which the fields in (2.37) become uncorrelated will be approximately $\Delta\nu = 1 \sim 10\,\mathrm{GHz}$.

In practice it is usually quite difficult to measure the field second-order correlation of (2.37) directly at optical frequencies for light scattered by a random medium. However, it is convenient to measure the intensity second-order correlation of $\langle I(\nu + \Delta\nu) I(\nu) \rangle$. This correlation is fourth-order in field, and since the field statistics are circular complex Gaussian, the Gaussian moment theorem [65] can be applied to give

$$\langle I(\nu + \Delta\nu) I(\nu) \rangle = \langle I \rangle^2 + \langle I \rangle^2 |P(\Delta\nu)|^2, \tag{2.38}$$

in which the relation given in (2.37) was also used to obtain this result. We can see that the intensity second-order correlation contains information only about the Fourier magnitude of $p(t)$. Since the Fourier phase information is lost, it is not possible to reconstruct $p(t)$ from measurements of intensity second-order correlations without using *a priori* information, which was the approach investigated in previous studies [66, 68].

We have recently shown [41] that intensity third-order correlations do contain sufficient information about the Fourier phase of $p(t)$ to enable reconstruction of $p(t)$ from intensity based measurements. The intensity third-order correlation, which is a

sixth-order correlation for the field, can again be evaluated by the Gaussian moment theorem [65] and the use of (2.37) to give

$$\begin{aligned}\langle I(\nu)I(\nu+\Delta\nu_1)I(\nu+\Delta\nu_2)\rangle = \langle I\rangle^3 + \langle I\rangle^3|P(\Delta\nu_1)|^2 + \langle I\rangle^3|P(\Delta\nu_2)|^2 + \\ \langle I\rangle^3|P(\Delta\nu_1+\Delta\nu_2)|^2 + 2\langle I\rangle^3\mathrm{Re}\{P(\Delta\nu_1)P(\Delta\nu_2)P^*(\Delta\nu_1+\Delta\nu_2)\}.\end{aligned} \tag{2.39}$$

It is mathematically convenient to define a normalized intensity of $\tilde{I} = (I - \langle I\rangle)/\langle I\rangle$, in which case the second-order and third-order correlations of the normalized intensity respectively become

$$\langle \tilde{I}(\nu+\Delta\nu)\tilde{I}(\nu)\rangle = |P(\Delta\nu)|^2, \tag{2.40}$$

and

$$\langle \tilde{I}(\nu)\tilde{I}(\nu+\Delta\nu_1)\tilde{I}(\nu+\Delta\nu_1+\Delta\nu_2)\rangle = 2\mathrm{Re}\left\{P(\Delta\nu_1)P(\Delta\nu_2)P^*(\Delta\nu_1+\Delta\nu_2)\right\}. \tag{2.41}$$

Identifying that the normalized intensity third-order correlation of (2.41) is equal to the real component of the bispectrum [69] of $p(t)$ is a key observation [41]. This result enables well established bispectral techniques [69, 70] to be used for reconstructing $p(t)$, which are detailed for this particular application in Section 2.4.

2.2.4 Intensity Temporal Response

It is possible to directly measure the intensity temporal response from a random medium due to an ultrafast optical pulse input. We show that the normalized ensemble average intensity temporal response is in fact equal to the time of flight distribution $p(t)$.

The electric field of the ultrafast pulse applied to the random medium is given by $a_{\mathrm{in}}(t)$ and the output field is given by $a_{\mathrm{out}}(t)$. Both these signals have an optical center frequency of ν_0 and are written as

$$a_{\mathrm{in}}(t) = u(t)\exp(j2\pi\nu_0 t) \ + \mathrm{c.c.} \tag{2.42}$$

and

$$a_{\mathrm{out}}(t) = v(t)\exp(j2\pi\nu_0 t) \ + \mathrm{c.c.}, \tag{2.43}$$

where $u(t)$ and $v(t)$ are the pulse complex amplitude envelope functions, of the input and output signals respectively. The function $v(t)$ is the stochastic output signal from a random medium in response to the deterministic input signal $u(t)$. The output intensity measured by a photodetector will have an ensemble average value of

$$\langle I(t)\rangle = \langle |v(t)|^2\rangle. \tag{2.44}$$

It is convenient to define the transfer function for a random medium that we shall denote by $H(\nu)$. Remaining consistent with linear system theory [71], if the response of a linear system to the input signal $\exp(j2\pi\nu t)$ is the output signal $H(\nu)\exp(j2\pi\nu t)$, then $H(\nu)$ is the transfer function of the linear system. Referring to (2.22) and (2.23), we readily see that the transfer function of a random medium is the output field, $H(\nu) = E_o(\nu)$, when the input field is $E_i = 1$. This result allows the second-order correlation of the random medium transfer function to be obtained directly from (2.37), and is written as

$$\langle H(\nu+\Delta\nu)H^*(\nu)\rangle = \langle |H(\nu)|^2\rangle P(\Delta\nu), \tag{2.45}$$

where the quantity $\langle |H(\nu)|^2\rangle = \langle I\rangle/|E_i|^2$ is a constant.

Denoting the Fourier transforms of $v(t)$ as $V(\nu)$ and $u(t)$ as $U(\nu)$, we can use the relation $V(\nu) = U(\nu)H(\nu+\nu_0)$ to express $v(t)$ as

$$v(t) = \int_{-\infty}^{\infty} \mathrm{d}\nu\; U(\nu)H(\nu+\nu_0)\exp(j2\pi\nu t). \tag{2.46}$$

Expression (2.46) is substituted into (2.44) allowing the ensemble average intensity to be written as

$$\begin{aligned}\langle I(t)\rangle = \Bigg\langle \int_{-\infty}^{\infty} \mathrm{d}\nu'\; U(\nu')H(\nu'+\nu_0)\exp(j2\pi\nu' t)\times \\ \int_{-\infty}^{\infty} \mathrm{d}\nu''\; U^*(\nu'')H^*(\nu''+\nu_0)\exp(-j2\pi\nu'' t)\Bigg\rangle.\end{aligned} \tag{2.47}$$

After interchanging the order of integration and the ensemble averaging, and making the variable substitution of $\Delta\nu = \nu' - \nu''$ and $\nu = \nu''$, (2.47) becomes

$$\langle I(t)\rangle = \int_{-\infty}^{\infty} \mathrm{d}\nu \int_{-\infty}^{\infty} \mathrm{d}\Delta\nu\; \langle H(\nu+\nu_0+\Delta\nu)H^*(\nu+\nu_0)\rangle U(\nu+\Delta\nu)U^*(\nu)\exp(j2\pi\Delta\nu t). \tag{2.48}$$

Using (2.45), the random medium transfer function second-order correlation term in (2.48) can be replaced by $\langle H(\nu+\nu_0+\Delta\nu)H^*(\nu+\nu_0)\rangle = \langle|H(\nu+\nu_0)|^2\rangle P(\Delta\nu)$. Also, if the bandwidth of the input ultrafast pulse is broad compared with the frequency range over which $P(\Delta\nu)$ is non-zero, then the approximation of $U(\nu+\Delta\nu) \simeq U(\nu)$ can be used. Physically, in the time domain, this can be interpreted as having the temporal width of the ultrafast input pulse much smaller than the temporal features in the times of flight distribution $p(t)$. This requirement is necessary if we wish to accurately probe the structure of the times of flight distribution using an ultrafast optical pulse. Under these conditions, (2.48) simplifies to

$$\langle I(t)\rangle = \int_{-\infty}^{\infty} \mathrm{d}\nu \langle|V(\nu)|^2\rangle \int_{-\infty}^{\infty} \mathrm{d}\Delta\nu \; P(\Delta\nu)\exp(j2\pi\Delta\nu t). \tag{2.49}$$

The second integral of (2.49) is by definition equal to $p(t)$. Applying Parseval's theorem,

$$\int_{-\infty}^{\infty} \mathrm{d}\nu \; \langle|V(\nu)|^2\rangle = \int_{-\infty}^{\infty} \mathrm{d}t \; \langle|v(t)|^2\rangle, \tag{2.50}$$

and using (2.44), we see that the normalized ensemble averaged intensity response is equal to the time of flight distribution for the scattered partial waves in the random medium,

$$p(t) = \frac{\langle I(t)\rangle}{\int_{-\infty}^{\infty} \mathrm{d}t \; \langle I(t)\rangle}. \tag{2.51}$$

2.2.5 Source Coherence Effects

When non-monochromatic light is used for the source, the measured speckle statistics are dependent upon both the coherence properties of the source and the scattering properties of the random medium, as we have demonstrated [68]. For non-monochromatic illumination, the total intensity at the output from a random medium (or reflected from a rough surface) will be the weighted sum of the intensities due to each frequency component present in the source. Therefore, it will not be possible to use (2.38) and (2.39) to estimate the Fourier transform of the temporal response, since these relations are only valid for monochromatic light. However, it is possible to

evaluate the first and second moments of the measured intensity to obtain information about the scattering properties of a random medium.

For non-monochromatic light with a power spectral density of $S(\nu)$, the first moment $\langle I \rangle$, and second moment $\langle I^2 \rangle$ are calculated using [72]

$$\langle I \rangle = \int_0^\infty \mathrm{d}\nu \, S(\nu) \langle E_o(\nu) E_o^*(\nu) \rangle, \tag{2.52}$$

and

$$\langle I^2 \rangle = \int_0^\infty \mathrm{d}\nu_1 \int_0^\infty \mathrm{d}\nu_2 \, S(\nu_1) S(\nu_2) \langle E_o(\nu_1) E_o^*(\nu_1) E_o(\nu_2) E_o^*(\nu_2) \rangle. \tag{2.53}$$

The above two equations are strictly true only when the observation time is long compared with the coherence time of the source [30]. The contrast ratio is defined by $C_I = \sigma_I / \mu_I$, where $\mu_I = \langle I \rangle$ is the mean and $\sigma_I = \sqrt{\langle I^2 \rangle - \langle I \rangle^2}$ is the standard deviation. Using the assumption of circular complex Gaussian statistics for the output field, the contrast ratio is calculated using (2.52) and (2.53) with the assumption of $\langle E_o(\nu) E_o^*(\nu) \rangle$ constant and independent of frequency, giving

$$C_I = \frac{\sigma_I}{\mu_I} = \frac{\left\{ \int_0^\infty \mathrm{d}\nu_1 \int_0^\infty \mathrm{d}\nu_2 \, S(\nu_1) S(\nu_2) \left| P(\nu_1 - \nu_2) \right|^2 \right\}^{1/2}}{\int_0^\infty \mathrm{d}\nu \, S(\nu)}. \tag{2.54}$$

For a source with a rectangular power spectral density, which can be synthesized with the tunable laser diode [68], the power spectral density is given by

$$S_{\mathrm{syn}}(\nu) = \begin{cases} 1/\Delta\nu_{\mathrm{syn}} & \text{if } 0 < \nu < \Delta\nu \\ 0 & \text{otherwise} \end{cases} \tag{2.55}$$

where $\Delta\nu_{\mathrm{syn}}$ is the synthesized linewidth of the power spectral density. The expression for the contrast ratio of (2.54) as a function of the synthesized linewidth is given by

$$C_I(\Delta\nu_{\mathrm{syn}}) = \frac{1}{\Delta\nu_{\mathrm{syn}}} \left\{ \int_0^{\Delta\nu_{\mathrm{syn}}} \mathrm{d}\nu_1 \int_0^{\Delta\nu_{\mathrm{syn}}} \mathrm{d}\nu_2 \left| P(\nu_1 - \nu_2) \right|^2 \right\}^{1/2}. \tag{2.56}$$

Thus we have the result that the contrast ratio is dependent upon the synthesized linewidth and the Fourier Transform of the temporal response.

2.3 Photon Transport

The transport of light in a random medium in the weak scattering limit (the transport mean free path is large compared with the wavelength) is well described by the Boltzmann transport equation, often called the radiative transfer equation (RTE) for light [1, 73]. The RTE models the transport of average intensity through the random medium, where the interference of partial waves along different paths can be neglected. An equivalent model is to describe the transport of photons in a scattering medium using similar techniques developed for modeling neutron transport in a nuclear reactor [74], which is the approach taken here.

Under the single-speed approximation [74], where the photons are assumed to travel with a single constant speed, the central quantity describing the distribution of photons within a scattering media is the "photon angular flux density" given by $\psi(\mathbf{r}, \hat{\mathbf{\Omega}}, t)$ with units of (photon $\mathrm{m}^{-2}\,\mathrm{s}^{-1}\,\mathrm{sr}^{-1}$). In the RTE notation, this is related to the specific intensity [1] by $I_\nu(\mathbf{r}, \hat{\mathbf{\Omega}}, t) = h\nu\psi(\mathbf{r}, \hat{\mathbf{\Omega}}, t)$, where h is Planck's constant and ν is the optical frequency of the light. The physical interpretation of the photon angular flux density can be best understood by considering the quantity of $\psi(\mathbf{r}, \hat{\mathbf{\Omega}}, t)\,\hat{\mathbf{\Omega}} \cdot \hat{\mathbf{n}}\,\mathrm{d}A\,\mathrm{d}\Omega$, which is the number of photons per second passing through an area $\mathrm{d}A$ with normal $\hat{\mathbf{n}}$, in the direction of $\hat{\mathbf{\Omega}}$ within solid angle $\mathrm{d}\Omega$, at time t and position $\mathbf{r}$.

The transport equation governing the photon angular flux density is derived on the basis of conservation of photons and is given by [74]

$$\frac{1}{v}\frac{\partial}{\partial t}\psi(\mathbf{r}, \hat{\mathbf{\Omega}}, t) = -[\mu_s(\mathbf{r}) + \mu_a(\mathbf{r})]\psi(\mathbf{r}, \hat{\mathbf{\Omega}}, t) - \hat{\mathbf{\Omega}} \cdot \nabla\psi(\mathbf{r}, \hat{\mathbf{\Omega}}, t) + \mu_s(\mathbf{r}) \int_{4\pi} \mathrm{d}\Omega'\, f(\hat{\mathbf{\Omega}}, \hat{\mathbf{\Omega}}')\psi(\mathbf{r}, \hat{\mathbf{\Omega}}', t) + S(\mathbf{r}, \hat{\mathbf{\Omega}}, t), \quad (2.57)$$

where v is the photon speed, $\mu_s(\mathbf{r})$ the scattering coefficient equal to the mean number of scattering events per unit distance, $\mu_a(\mathbf{r})$ is the absorption coefficient equal to the mean number of absorption events per unit distance, $f(\hat{\mathbf{\Omega}}, \hat{\mathbf{\Omega}}')$ is the scattering phase function representing the probability that a photon traveling in direction $\hat{\mathbf{\Omega}}'$ will be scattered into direction $\hat{\mathbf{\Omega}}$, and $S(\mathbf{r}, \hat{\mathbf{\Omega}}, t)$ is a source term. The LHS of (2.57)

represents the net change with time in the total number of photons traveling in direction $\hat{\Omega}$ in a elemental volume located at position $\mathbf{r}$. The first term on the RHS of (2.57) is the change due to out-scattering and absorption. The second term is the flow out of the elemental volume. The third term represents the increase due to in-scattering from all directions $\hat{\Omega}'$ into direction $\hat{\Omega}$. Finally, the last term is the input due to any sources.

It should be emphasized that the transport equation described by (2.57) is developed after ensemble averaging has been performed, and neglects interference by assuming that it does not contribute to the average intensity. One phenomenon that (2.57) cannot describe is that of speckle. On a microscopic scale, the behavior of light in a random medium is described by Maxwell's equations, which of course can readily describe the speckle behavior, even if based on the simple random phasor sum model. However, the transport model is still useful for speckle based measurements in random media, since it can provide a model for determining the time of flight distribution for the photons or scattered partial waves.

2.3.1 Diffusion Approximation

The photon transport equation of (2.57), being a 6 dimensional integro-differential equation of 3 spatial coordinates, 2 directional coordinates (with direction angles in a polar coordinate system of θ and ϕ, defining the direction vector as $\hat{\Omega} = \hat{\mathbf{x}}\sin\theta\cos\phi + \hat{\mathbf{y}}\sin\theta\sin\phi + \hat{\mathbf{z}}\cos\theta$), and 1 time is very difficult equation to solve in practical applications. In many cases, it is not necessary to solve the full transport equation, but an approximation to it called the diffusion approximation that is valid under a wide range of random media of interest [75, 76, 77, 78].

The diffusion approximation assumes that the photon angular flux density $\psi(\mathbf{r}, \hat{\Omega}, t)$ has a weak dependence upon direction (at any given point in space the directional distribution of the photons is almost isotropic). This is achieved by defining angle-

integrated quantities photon flux density, $\Phi(\mathbf{r},t)$ and photon current density, $\mathbf{J}(\mathbf{r},t)$, both with units of (photon $\mathrm{m}^{-2}\,\mathrm{s}^{-1}$). These quantities are defined by

$$\Phi(\mathbf{r},t) = \int_{4\pi} \mathrm{d}\Omega\, \psi(\mathbf{r},\hat{\mathbf{\Omega}},t), \tag{2.58}$$

and

$$\mathbf{J}(\mathbf{r},t) = \int_{4\pi} \mathrm{d}\Omega\, \hat{\mathbf{\Omega}}\psi(\mathbf{r},\hat{\mathbf{\Omega}},t). \tag{2.59}$$

Under the diffusion approximation, they are related to $\psi(\mathbf{r},\hat{\mathbf{\Omega}},t)$ by [74]

$$\psi(\mathbf{r},\hat{\mathbf{\Omega}},t) \simeq \frac{1}{4\pi}\Phi(\mathbf{r},t) + \frac{3}{4\pi}\mathbf{J}(\mathbf{r},t)\cdot\hat{\mathbf{\Omega}}, \tag{2.60}$$

which can also be interpreted as approximating $\psi(\mathbf{r},\hat{\mathbf{\Omega}},t)$ by the first two terms of its spherical harmonics expansion [74]. By substituting (2.60) into (2.57), assuming all sources are isotropic, and that the rate of time change in the photon current density is small compared with the mean time between scattering events, the diffusion equation for the photon flux density is obtained

$$\frac{\partial}{\partial t}\Phi(\mathbf{r},t) + v\mu_a(\mathbf{r})\Phi(\mathbf{r},t) - \nabla\cdot[D(\mathbf{r})\nabla\Phi(\mathbf{r},t)] = vS_0(\mathbf{r},t). \tag{2.61}$$

The isotropic source term is given by $S_0(\mathbf{r},t)$. The diffusion coefficient $D(\mathbf{r})$ has units of $(\mathrm{m}^2\,\mathrm{s}^{-1})$, and is given by

$$D(\mathbf{r}) = \frac{v}{3\left[\mu_a(\mathbf{r}) + \mu_s'(\mathbf{r})\right]}. \tag{2.62}$$

The quantity $\mu_s'(\mathbf{r})$ is called the reduced scattering coefficient, which takes into account the integrated angular dependence of $f(\hat{\mathbf{\Omega}},\hat{\mathbf{\Omega}}')$, and is defined by

$$\mu_s'(\mathbf{r}) = (1-g)\mu_s(\mathbf{r}). \tag{2.63}$$

The parameter g is a measure of the scattering event anisotropy. It is defined as the mean cosine of the angle between the input direction $\hat{\mathbf{\Omega}}'$ and the output direction $\hat{\mathbf{\Omega}}$, given by

$$g = \int_{4\pi} \mathrm{d}\Omega'\, f(\hat{\mathbf{\Omega}},\hat{\mathbf{\Omega}}')\hat{\mathbf{\Omega}}\cdot\hat{\mathbf{\Omega}}', \tag{2.64}$$

where $0 \leq g \leq 1$. Often the notation of l and l^* are used to represent the scattering mean free path and the transport mean free path. In terms of the scattering coefficient notation, $l = 1/\mu_s$ and $l^* = 1/\mu_s'$ (for $\mu_a = 0$). Also obtained from the diffusion approximation is an expression that relates $\Phi(\mathbf{r}, t)$ and $\mathbf{J}(\mathbf{r}, t)$, called Fick's Law [74]:

$$\mathbf{J}(\mathbf{r}, t) = -\frac{D(\mathbf{r})}{v} \nabla \Phi(\mathbf{r}, t). \tag{2.65}$$

It should also be pointed out that the conditions required to obtain zero-mean circular complex Gaussian statistics to describe the speckle field are independent of those required for the diffusion approximation to be valid. For example, a slab of ground glass readily produces a scattered field with Gaussian statistics, but the light transport is not well described by the diffusion approximation. Therefore, the second-order and third-order intensity correlation techniques are very general and not limited to random media in the diffusion regime.

The intensity measured by a photodetector $I_{\text{meas}}(t)$ is related to the photon current density [79],

$$I_{\text{meas}}(t) = K \int_{A_d} \mathrm{d}A \; \hat{\mathbf{n}} \cdot \mathbf{J}(\mathbf{r}, t), \tag{2.66}$$

where A_d is the photodetector area, $\hat{\mathbf{n}}$ is the photodetector surface normal, and K is a constant proportional to the photodetector numerical aperture and quantum efficiency.

Under the diffusion approximation, we define the intensity temporal response of a random medium by the normalized Green's function of (2.61). Hence, with a source term of $S_0(\mathbf{r}, t) = \delta(\mathbf{r}', t)$, where $\mathbf{r}'$ is the source location we solve (2.61), (2.65), and (2.66) to obtain the intensity temporal response under the diffusion approximation

$$p(t) = \frac{I_{\text{meas}}(t)}{\int_{-\infty}^{\infty} \mathrm{d}t \; I_{\text{meas}}(t)}, \tag{2.67}$$

which is identical in form to Eq. (2.51).

2.3.2 Temporal Response of a Homogeneous Slab

For a homogeneous slab of a scattering random medium, it is possible to obtain an analytic solution to the diffusion equation of (2.61), and hence the temporal response [80]. Consider an infinite 3-D homogeneous scattering domain, with $\mu_s'(\mathbf{r}) = \mu_s'$ and $\mu_a(\mathbf{r}) = \mu_a$. Then the homogeneous Green's function of (2.61), with the source term a delta-function at the origin $S_0(\mathbf{r}, t) = \delta(0, 0)$ is given by [81]

$$G_{3D}(\mathbf{r}, t) = v(4\pi Dt)^{-3/2} \exp\left(-\frac{r^2}{4Dt}\right) \exp(-\mu_a v t). \tag{2.68}$$

The diffusion coefficient is $D = v/3(\mu_s' + \mu_a)$. For a homogeneous slab, there are boundaries between the scattering region of the slab and free-space. These boundaries cannot be exactly treated in the photon transport and diffusion models, but are often treated approximately with sufficient accuracy to be useful [79, 82, 83, 84]. The boundary condition employed here is the partial current boundary condition that treats the boundary as reflecting a fraction of the incident photon current density and transmitting the rest into free-space. For a boundary at $z = 0$, the boundary condition is

$$\frac{D}{v} \frac{\partial \Phi}{\partial z}\bigg|_{z=0} + \frac{\Phi}{2A} = 0. \tag{2.69}$$

The factor A is given by

$$A = \frac{1 + R_{\text{eff}}}{1 - R_{\text{eff}}}, \tag{2.70}$$

where R_{eff} is the effective reflection coefficient for the photon flux density, which is used to model the effect of Fresnel reflections at the boundary between free-space and the background refractive index n of the slab [79]. (For the samples used in this study, a background refractive index of $n = 1.4$ was used, giving a value of $R_{\text{eff}} = 0.493$.) The boundary condition of (2.69) is equivalent to setting the photon flux density to zero at some extrapolated distance z_b from the boundary, $\Phi(z_b) = 0$, where $z_b = 2AD/v$.

The infinite 3-D homogeneous Green's function of (2.68) and the boundary condition of (2.69) can be combined with a method of images technique to determine

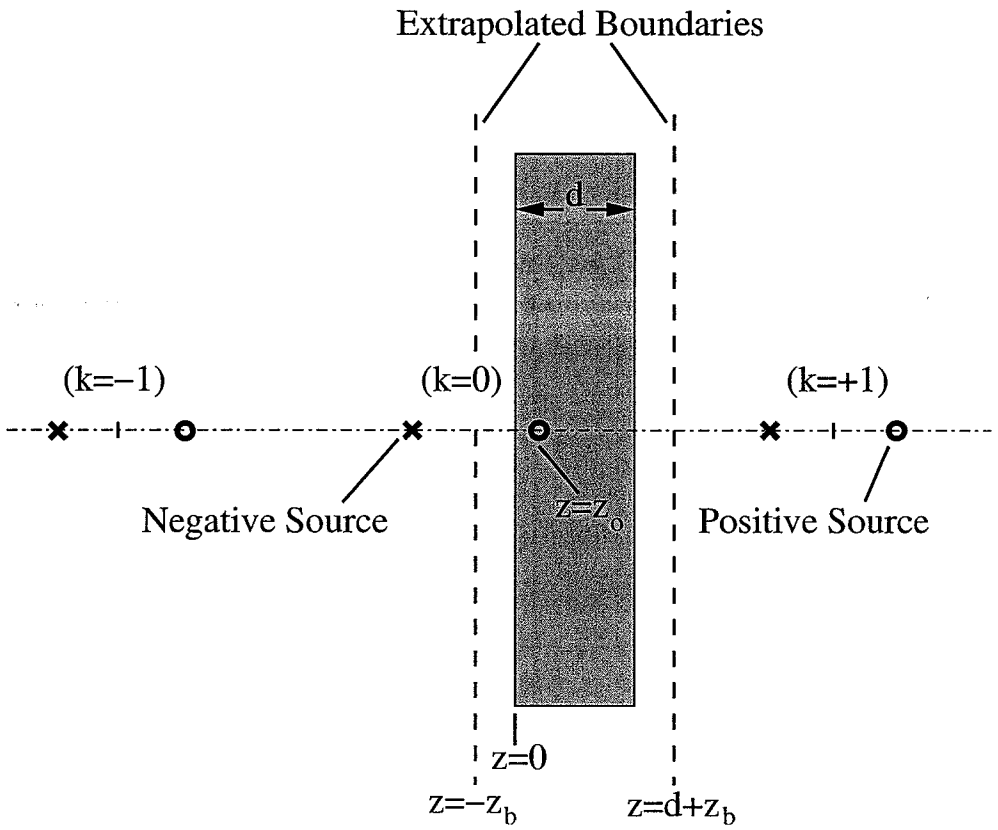

Fig. 2.8. A schematic for the method of images technique applied to a homogeneous slab. The slab is of thickness d and the source is at $z = z_o$.

the Green's function of a finite slab [80, 85]. A schematic diagram of the method of images is given in Fig. 2.8. The source is modeled as a point source at a distance $z_o = 1/\mu_s'$ from the incident boundary. At this distance, the source is modeled as having an isotropic distribution, as required by the diffusion approximation. The method of images consists of using an infinite series of dipole sources, with the positive and negative point sources separated by a distance of $2z_o + 2z_b$, with the dipole centers located at

$$z_c = -z_b + k(2d + 4z_b), \tag{2.71}$$

where $k = 0, \pm 1, \pm 2, \ldots$ and d is the slab thickness. This can be seen in Fig. 2.8. An infinite series of these will give $\Phi(-z_b) = 0$ and $\Phi(d + z_b) = 0$. The actual locations

of the positive sources in the dipoles is given by z_k and for the negative sources by $\overline{z_k}$, conveniently written as

$$\begin{aligned} z_k &= z_c + (z_o + z_b), \\ \overline{z_k} &= z_c - (z_o + z_b). \end{aligned} \tag{2.72}$$

Using equations (2.68)-(2.72), the Green's function for a finite homogeneous slab of thickness d with a point source $S_0(x, y, z, t) = \delta(0, 0, z_o, 0)$, is located at $z = z_o$,

$$G_s(\mathbf{r}, t) = v(4\pi Dt)^{-3/2} \exp\left[-\frac{x^2 + y^2}{4Dt}\right] \exp(-\mu_a v t) \times \sum_{k=-\infty}^{\infty} \left\{ \exp\left[-\frac{(z - z_k)^2}{4Dt}\right] - \exp\left[-\frac{(z - \overline{z_k})^2}{4Dt}\right] \right\}. \tag{2.73}$$

In practice, it is usually sufficient to take values of $k = 0, \pm 1, \pm 2$ in the summation. The Green's function $G_s(\mathbf{r}, t)$ of (2.73) is then used in place of $\Phi(\mathbf{r}, t)$ of (2.65)-(2.67) to calculate the temporal response $p(t)$ of the homogeneous finite slab. Several example temporal responses in a transmission configuration, with the detection location of $z = d$ are given in Fig. 2.9.

2.4 Bispectrum

Third-order correlations provide many advantages over second-order correlations for signal recovery by enabling phase information about the underlying signal to be obtained, and they also having a reduced sensitivity to certain types of additive noise, as reviewed by Lohmann [69]. Here, it is shown that third-order frequency correlations measurements of speckle intensity enable the temporal response of a random medium to be reconstructed.

To review some of the basic concepts, consider the arbitrary real signal $f(t)$ whose third-order temporal correlation is given by

$$g^{(3)}(\tau_1, \tau_2) = \int_{-\infty}^{\infty} \mathrm{d}t \; f(t) f(t + \tau_1) f(t + \tau_2). \tag{2.74}$$

The Fourier transform of $g^{(3)}(\tau_1, \tau_2)$,

$$G^{(3)}(\nu_1, \nu_2) = \int_{-\infty}^{\infty} \mathrm{d}\tau_1 \int_{-\infty}^{\infty} \mathrm{d}\tau_2 \; g^{(3)}(\tau_1, \tau_2) \exp[-j2\pi(\nu_1 \tau_1 + \nu_2 \tau_2)], \tag{2.75}$$

(a)

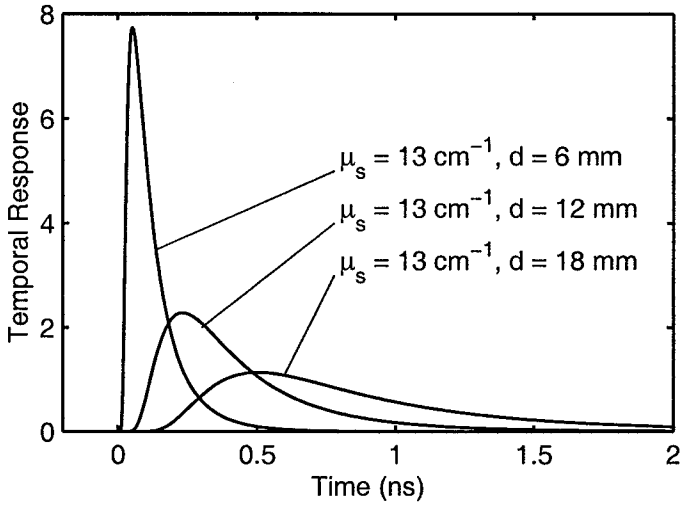

(b)

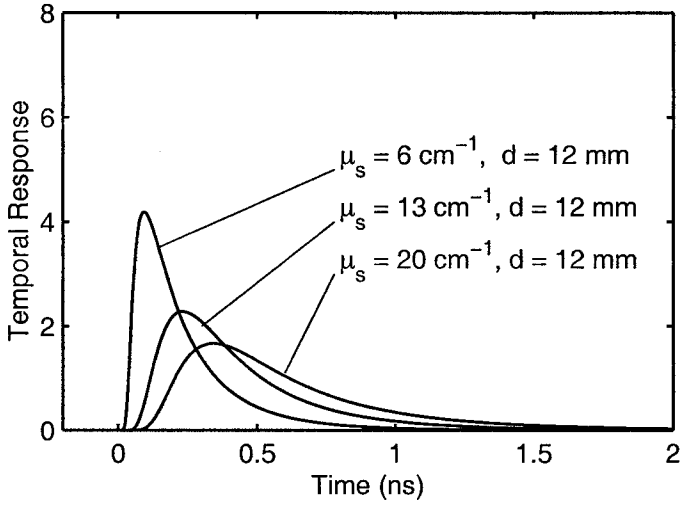

Fig. 2.9. (a) Typical calculated temporal responses as the sample thickness is varied. (b) Typical calculated temporal responses as the sample scattering coefficient is varied.

is defined as the bispectrum of $f(t)$, and can also be expressed in terms of the Fourier transform of $f(t)$, denoted as $F(\nu)$, by the product

$$G^{(3)}(\nu_1, \nu_2) = F(\nu_1)F(\nu_2)F(-\nu_1 - \nu_2). \tag{2.76}$$

Since $f(t)$ is real, its Fourier transform is Hermitian, allowing the identity $F(-\nu_1 - \nu_2) = F^*(\nu_1 + \nu_2)$ to be used in (2.76), giving the result of

$$G^{(3)}(\nu_1, \nu_2) = F(\nu_1)F(\nu_2)F^*(\nu_1 + \nu_2). \tag{2.77}$$

We shall express the Fourier transform of $f(t)$ in terms of its magnitude and phase as $F(\nu) = A(\nu)\exp[j\phi(\nu)]$ and the bispectrum in terms of its magnitude and phase $G^{(3)}(\nu_1, \nu_2) = B(\nu_1, \nu_2)\exp[j\psi(\nu_1, \nu_2)]$. Then the relationship between the Fourier phase and the bispectral phase of $f(t)$, obtained from (2.78), is given by

$$\psi(\nu_1, \nu_2) = \phi(\nu_1) + \phi(\nu_2) - \phi(\nu_1 + \nu_2). \tag{2.78}$$

The expression of (2.78) shows that the bispectral phase is a linear combination of Fourier phases. Also, if we add an arbitrary linear phase component to the Fourier phase of $f(t)$, replacing $\phi(\nu)$ by $\hat{\phi}(\nu) = \phi(\nu) + \alpha\nu$, then from (2.78) we see that the bispectral phase is independent of the linear phase component $\alpha\nu$. For this reason, the bispectrum of $f(t)$ is often termed "blind" to linear Fourier phase. In the time domain, this equates to all real functions $f(t)$ that differ by an arbitrary time-offset, all having the same bispectrum.

The expression of (2.78) can be exploited to reconstruct the Fourier phase of $f(t)$ from its bispectral phase, using a simple explicit scheme [70]. Writing the Fourier and bispectral phases in discrete notation, where $\phi_k = \phi(k\delta\nu)$ is the k^{th} Fourier phase and $\psi_{i,j} = \psi(i\delta\nu, j\delta\nu)$ is the $(i,j)^{\text{th}}$ component of the bispectral phase, where $\delta\nu$ is the sample frequency increment, enables the Fourier phase to be reconstructed using [70]

$$\phi_k = \frac{1}{k-1}\sum_{i=1}^{k-1} \phi_i + \phi_{k-i} - \psi_{i,k-i}, \quad k = 2, \ldots, N, \tag{2.79}$$

where $\phi_0 = 0$, and $\phi_1 = \phi(\delta\nu)$ is arbitrary, and N is the number of samples. The arbitrary value for ϕ_1 gives the reconstructed Fourier phase one degree of freedom, that is equivalent to an indeterminate linear Fourier phase, which in the time-domain gives an arbitrary time-offset. This is a consequence of the bispectrum being independent of linear Fourier phase, as discussed previously.

Using the discrete notation of (2.79), it is possible to express (2.78) as an overdetermined system of linear equations for the unknown Fourier phase ϕ_k. Then, the Fourier phase can also be reconstructed based on least-squares techniques [86, 87, 88].

2.4.1 Reconstruction of the Temporal Response

By comparing (2.77) and (2.41) it can be readily seen that the speckle intensity third-order frequency correlation from a random medium is equal to twice the real-part of the bispectrum of the temporal response $p(t)$. Therefore, by using bispectral techniques we can reconstruct the Fourier phase, and when combined with the Fourier magnitude obtained from the speckle intensity second-order frequency correlations of (2.40), we obtain the Fourier transform of the temporal response $P(\Delta\nu)$. By taking an inverse Fourier transform, the temporal response $p(t)$ is recovered. This is a key result of this study.

Defining the normalized intensities of $\tilde{I}_1 = \tilde{I}(\nu_0)$, $\tilde{I}_2 = \tilde{I}(\nu_0 + \Delta\nu_1)$, and $\tilde{I}_3 = \tilde{I}(\nu_0 + \Delta\nu_1 + \Delta\nu_2)$, the bispectral phase is obtained from third-order and second-order correlations using

$$\psi(\Delta\nu_1, \Delta\nu_2) = \pm\cos^{-1}\left[\frac{\langle\tilde{I}_1\tilde{I}_2\tilde{I}_3\rangle}{2(\langle\tilde{I}_1\tilde{I}_2\rangle\langle\tilde{I}_2\tilde{I}_3\rangle\langle\tilde{I}_3\tilde{I}_1\rangle)^{1/2}}\right]. \tag{2.80}$$

The bispectral phase from (2.80) is then used with the techniques to reconstruct the Fourier phase from (2.78).

The full bispectral phase cannot be directly obtained from the speckle correlation measurements, but only the cosine of the bispectral phase. The main consequence of this is a sign ambiguity in the total reconstructed Fourier phase, leading to time reversal indeterminacy in the temporal response. A more severe limitation occurs if the Fourier phase is not monotonic and its derivative changes sign over a reconstruction interval of $\delta\nu$. However, the form of the temporal response from the random media used for this study are all observed to have a monotonic Fourier phase, which is expected to be true for all similar random media of practical interest.

2.5 Summary

It has been shown that the speckle field from a random medium is well described by Gaussian statistics under the assumptions of the random phasor sum model for the scattered light. The formation of speckle through an imaging system has been discussed, highlighting the importance of the optical transfer function and field statistics in the object plane on determining the field statistics in the image plane. The measured intensity correlations in a speckle pattern as a function of frequency were shown to be related to the Fourier transform of the time of flight distribution for the scattered partial waves through the random medium. This was also shown to be equal to the intensity temporal response that can also be directly measured. The photon transport equation and the diffusion approximation were discussed and provide an analytical model for calculating the temporal response of a random medium. Finally, third-order correlations and bispectral techniques were discussed demonstrating the reconstruction of the temporal response is possible from measured speckle intensity correlations.

3. EXPERIMENTAL TECHNIQUE FOR SPECKLE MEASUREMENTS

3.1 Introduction

In principle, it is quite simple to generate a speckle pattern in the laboratory. For example, illuminating a rough surface like paper with a highly coherent laser source will produce a speckle pattern. However, in practice, it is not necessarily as simple to accurately measure the intensity statistics of a speckle pattern. In this chapter, the experimental setup used to measure the speckle statistics from a random medium and its characterization shall be discussed.

3.2 Experimental Setup

The experimental setup used to obtain the speckle intensity frequency correlation data is shown in Fig. 3.1. The tunable laser source is an external cavity laser diode of the Littman-Metcalf design (New Focus, model# Vortex-6017), that has a single mode output with a narrow-linewidth (nominally 5 MHz), and has a center wavelength of $\lambda = 850\,\text{nm}$. The average output power is about 10 mW and it is linearly polarized. The center frequency can be tuned over a range of approximately 60 GHz by piezoelectric adjustment of the cavity mirror relative to the cavity grating. After passing through an optical isolator, a small portion of the output power was coupled into a scanning Fabry-Perot interferometer using the half-wave plate (HWP) retarder and polarizing beam-splitter (PBS) combination. This was done to monitor the laser diode center frequency as it is tuned. Most of the optical power was focused onto the front face of the scattering random medium using the lens L1 of focal length $f_{L1} = 50\,\text{mm}$.

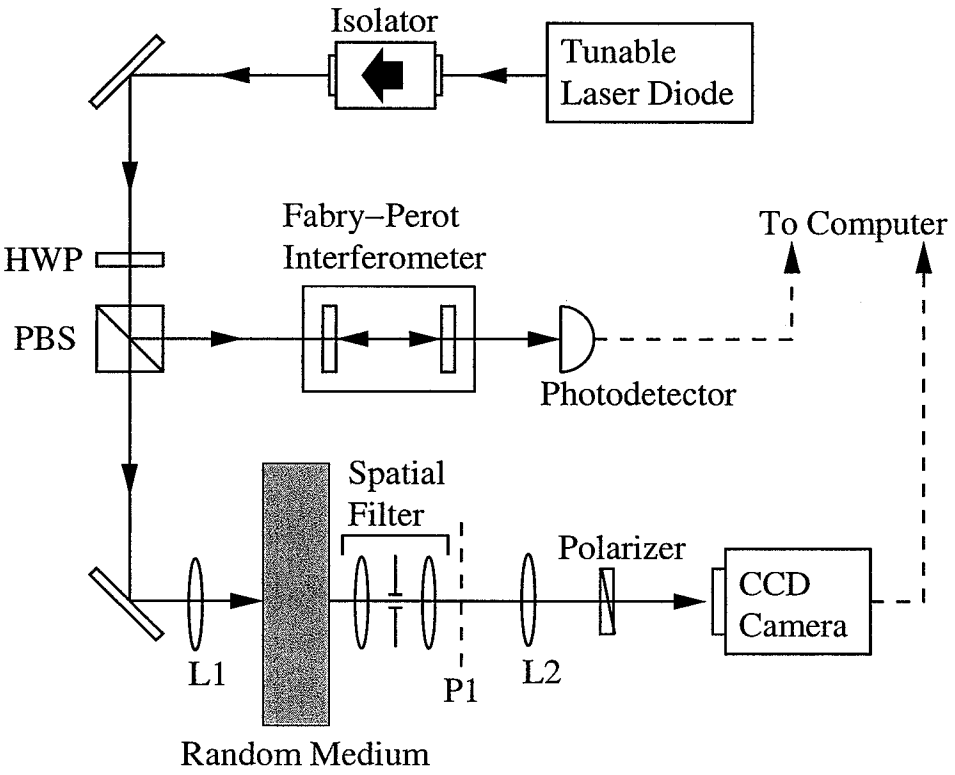

Fig. 3.1. The experimental setup used to measure the speckle intensity patterns as a function of the laser diode center frequency. The Fabry-Perot interferometer is used to monitor the change in the laser diode center-frequency as it is tuned. Lens L1 ($f_{L1} = 50\,\text{mm}$) focuses the laser output onto the front face of the scattering random medium. The spatial structure of the speckle pattern at plane P1 is controlled by the unity magnification spatial filter. Lens L2 ($f_{L2} = 75\,\text{mm}$) provides a magnification factor of $M = 10$ from the plane P1 to the CCD image plane, where the resultant frequency-dependent speckle pattern is obtained.

A small area of $1.2\,\text{mm} \times 1.5\,\text{mm}$ on the back face of the scattering random medium was imaged onto a cooled CCD camera with 1000×800 pixels of size $15\mu\text{m} \times 15\mu\text{m}$ (Princeton Instruments, model# TE/CCD-MicorMAX-800PB). The imaging optics consists of a spatial filter in a $4f$ telescope configuration that gives unity magnification at plane P1, and a lens L2 that provides a magnification of $M = 10$ from plane P1 to the CCD image plane. The spatial filter is formed from two identical achromatic lenses of focal length $f = 50\,\text{mm}$ and an adjustable iris aperture with a typical diameter of $D = 2\,\text{mm}$, located at the Fourier focal plane. The aperture is used to control the

spatial feature size in the random structure of a measured speckle pattern. The lens L2 is an achromatic lens of focal length $f_{L2} = 75\,\text{mm}$.

The light emerging from the random medium is no longer linearly polarized due to the multiple scattering. Therefore, the imaged scattered light was passed through a polarizer to analyze the same linear polarization as the input light for detection with the CCD camera, because a single linear polarization (scalar) model was assumed for the scattered field. Exposure times of about 1 s were used by the CCD camera to acquire a speckle image.

The random media used for this study were commercial white acrylics (Cyro Industries, Acrylite FF) that consist of a transparent acrylic background embedded with a homogeneous concentration of small TiO_2 particles approximately 50 nm in diameter.

3.3 CCD Camera Characterization

The performance of the cooled CCD camera is of critical importance for accurately measuring speckle intensity statistics from a random medium. The CCD camera measures the optical intensity over an area of $15\,\text{mm} \times 12\,\text{mm}$ in the image plane and provides an array of 1000×800 data points in (integer) units of counts, in the range of 0–4095. The measurement noise introduced by the CCD camera must be small in order to obtain a sufficient signal-to-noise ratio for estimating the speckle intensity statistics.

The noise mechanisms for a scientific class CCD camera fall into the two main categories of dark-current noise and read-noise. Dark-current noise is the fluctuations in the thermally generated dark-current [89] and can be minimized by cooling the CCD array. For the CCD camera used in this study, at a temperature of -40 °C, the dark-current noise is specified to be less than 1 photo-electron per pixel per second. This figure is very low, and in fact will register as less that 1 count for exposure times of several seconds. The read-noise is the effective noise produced by the internal am-

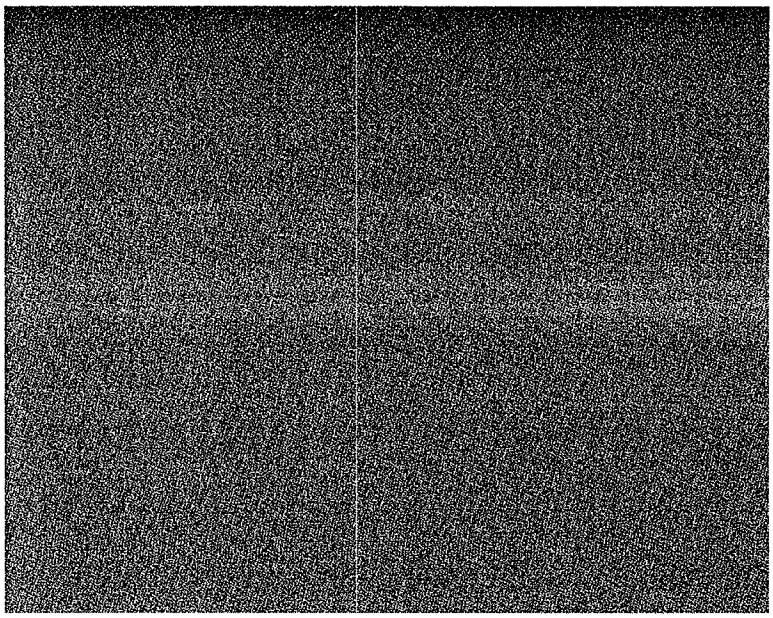

Fig. 3.2. A typical dark-field background image acquired from the cooled CCD camera.

plifiers and the analog-to-digital converter used to convert the stored photo-electrons into the computer readable units of counts. The read-noise for the CCD camera used here was measured to be about 2 counts, which is defined as the standard deviation of the difference between two dark-field images.

In Fig. 3.2, a typical dark-field background image is shown that was obtained by performing an exposure in the absence of any light, thus providing a reference background which can be subtracted on a pixel by pixel basis from actual intensity measurements of interest to remove any CCD background bias. This image is plotted using linear gray-scale mapping, with black representing pixels with background levels 60 counts or less, and with white representing pixels with background levels of 75 counts or more. The vertical white line seen in this image is not a printing anomaly, but is a row of "hot pixels" that have background levels in the range of 75–80 counts, thus appearing as white. This higher bias for the hot pixels will be subtracted from any acquired intensity image, and therefore will not affect the intensity measurements (assuming their responsivity is identical to all the other pixels.)

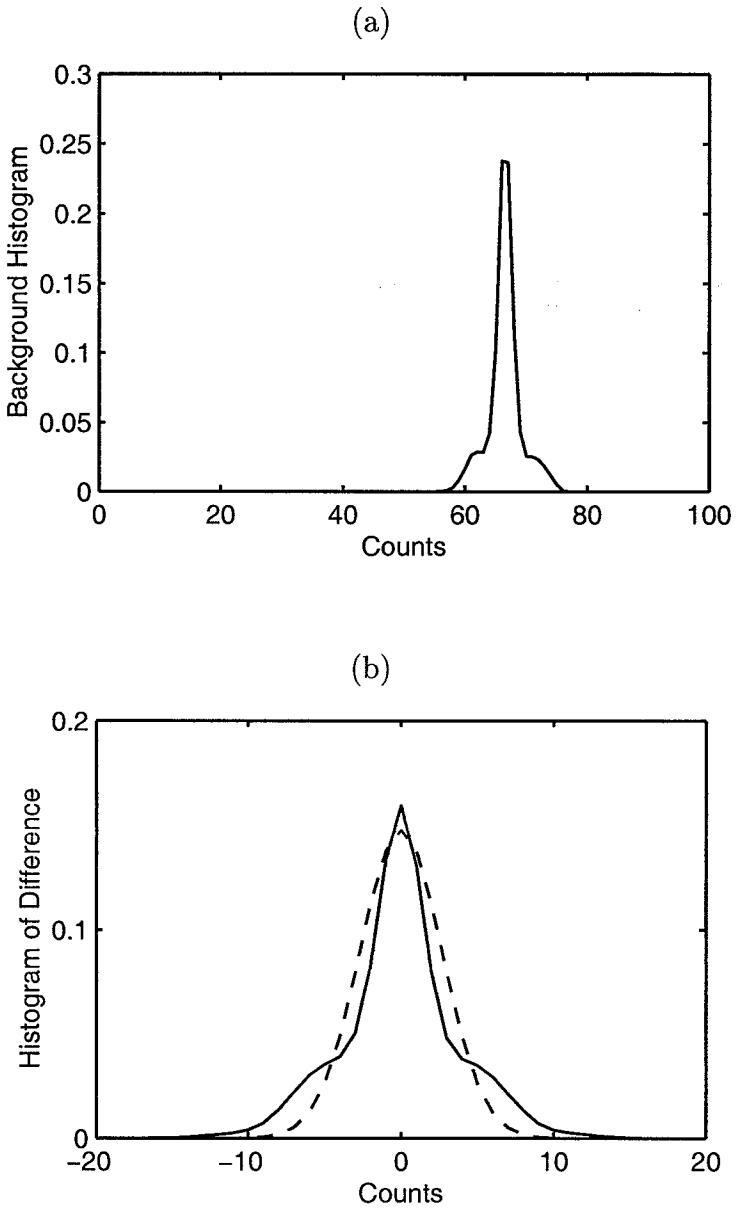

Fig. 3.3. (a) The histogram of the dark-field background image given in Fig. 3.2. The mean is 66 counts. (b) (solid line) The histogram of the difference between two dark-field background images, giving a measure of the CCD camera read-noise. A zero-mean Gaussian with a standard deviation of 2.8 counts (dashed line).

Figure 3.3(a) presents the histogram of the background image shown in Fig. 3.2. The mean background count of approximately 66 counts, as can be seen from this histogram figure, is an intentional offset applied to the CCD camera analog-to-digital

converter. This is done to allow a background subtraction that gives a zero-mean read-noise (if the analog-to-digital converter offset was set to zero, then the read-noise can only be positive, and hence will not be zero-mean.) The histogram of the difference between two dark-field background images is shown in Fig. 3.3(b). This allows the CCD camera read-noise to be estimated. Assuming that the read-noise in each dark-field background image is statistically independent, and that the read-noise of a single image is Gaussian with a variance of σ_r^2, then the difference will also be Gaussian, but with a variance of $2\sigma_r^2$. The histogram plotted in Fig. 3.3(b) is seen to be non-Gaussian due to the presence of the extended tails in the distribution. The dashed line in Fig. 3.3(b) is a Gaussian approximation with a standard deviation of 2.8 counts, which estimates the CCD read-noise to be $\sigma_r = 2$ counts.

In summary, the procedure used to obtain accurate intensity measurements using the CCD camera is described as follows: (i) acquire a dark-field background image, (ii) acquire an optical intensity image from the experiment, (iii) subtract on a pixel by pixel basis the dark-field background of (i) from the measured intensity of (ii) to obtain an estimate of the true image intensity. The advantage of performing a background subtraction is that any CCD bias is removed from the image. The disadvantage is that the read-noise in the true image will be slightly higher (by a factor of $\sqrt{2}$) than the read-noise of each image. However, this has minimal effect because the read-noise of $\sigma_r = 2$ counts is very small.

3.4 Measurement of Speckle Intensity Statistics

A typical measured speckle intensity pattern from a random medium is shown in Fig. 3.4. The intensity histogram for this image is shown in Fig. 3.5, which provides an estimate of the first-order statistics of the speckle intensity, and is seen to closely model the negative exponential pdf expected for fully developed (circular complex Gaussian) field statistics [47]. However, there is a small observable intensity offset in

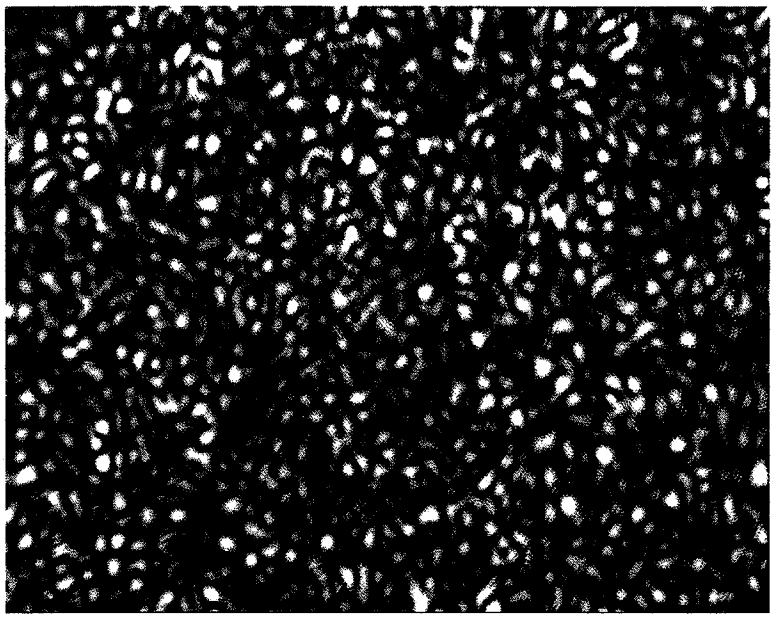

Fig. 3.4. A typical measured speckle intensity pattern from a random medium measured using the experimental setup shown in Fig. 3.1.

this data which is not due to ambient room light (which was rigorously eliminated from the experiment) nor is it due to the CCD read-noise.

To model the behavior of this undesirable intensity offset, I proposed an empirical model for the measured intensity that is surprisingly accurate over a wide range of experimental conditions. Define the measured intensity I_m to be the sum

$$I_m = I_t + I_n, \tag{3.1}$$

where I_t is the true speckle intensity and I_n is a statistically independent noise intensity. The true speckle intensity has a negative exponential pdf of

$$p_{I_t}(I_t) = \frac{1}{\mu_I} \exp(-I_t/\mu_I), \tag{3.2}$$

where the true intensity mean is $\mu_I = \langle I_t \rangle$. The noise intensity is modeled by a Gaussian pdf

$$p_{I_n}(I_n) = \frac{1}{\sqrt{2\pi}\sigma_n} \exp\left[-\frac{1}{2}\frac{(I_n - \eta_I)^2}{\sigma_n^2}\right], \tag{3.3}$$

with a mean intensity offset of $\eta_I = \langle I_n \rangle$ and a variance of σ_n^2. If the only limiting experimental factor were CCD read-noise, then the noise intensity pdf of (3.3) would

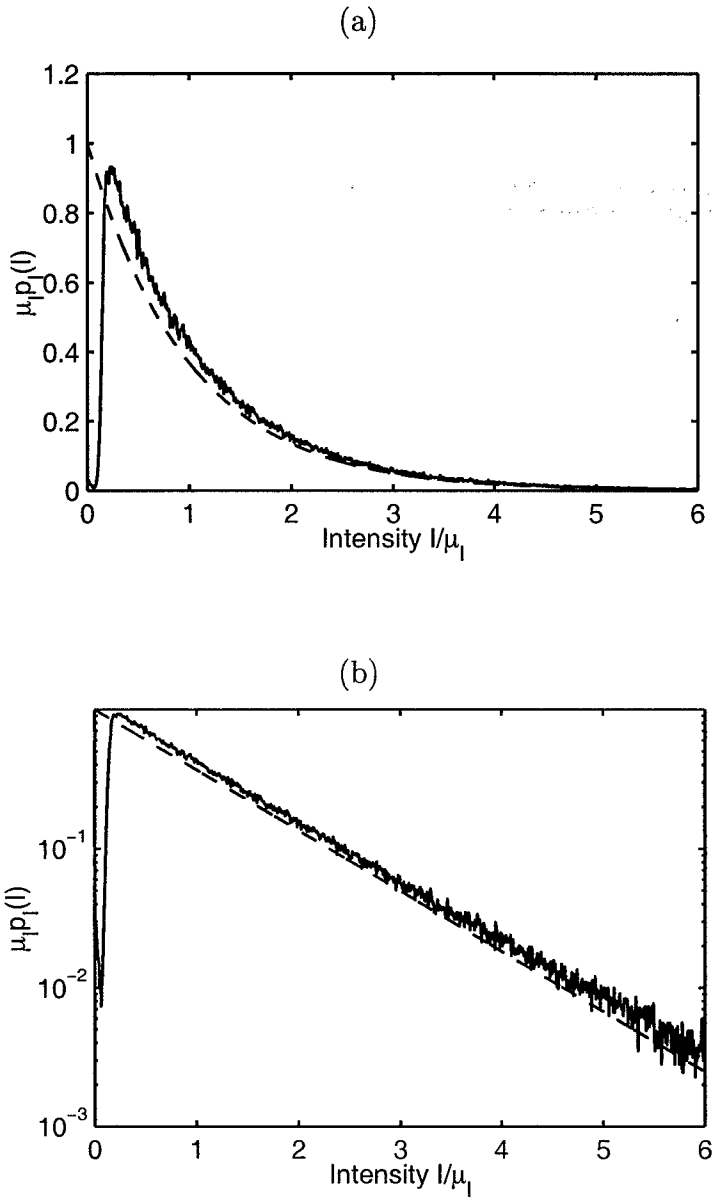

Fig. 3.5. (a) The measured intensity histogram of the speckle intensity given in Fig. 3.4 used to estimate the first-order intensity statistics (solid line). The theoretical negative exponential distribution expected for zero-mean circular complex Gaussian field statistics (dashed line). (b) The data of (a) plotted with semi-logarithmic axes.

have a mean $\eta_I = 0$ and a variance equal to the CCD read-noise variance of $\sigma_n^2 = \sigma_r^2$, which would represent the best possible measurable speckle statistics with the CCD camera used for this study. However, for the measured data, η_I is non-zero and the noise intensity variance is greater than the CCD read-noise.

The pdf for the measured intensity I_m is given by the convolution of (3.2) and (3.3), since it was assumed that I_t and I_n are statistically independent, giving

$$p_{I_m}(I_m) = \frac{1}{2\mu_I} \exp\left[-\frac{(I_m - \eta_I)}{\mu_I}\right] \exp\left[-\frac{1}{2}\frac{\sigma_n^2}{\mu_I^2}\right] \left[1 + \operatorname{erf}\left(\frac{I_m - \eta_I - \sigma_n^2/\mu_I}{\sqrt{2}\sigma_n}\right)\right], \quad (3.4)$$

where $\operatorname{erf}(x)$ is the error function. The mean of the measured intensity is simply

$$\langle I_m \rangle = \mu_I + \eta_I. \quad (3.5)$$

The interesting behavior of this empirical model is that the offset intensity η_I was found to be proportional to the mean of the measured intensity,

$$\eta_I = \beta \langle I_m \rangle. \quad (3.6)$$

This model with $\beta = 0.13$ and $\sigma_n = 7$ was found to fit the measured data over a large range of experimental conditions. For example, these values would fit the experimental data measured for random medium samples with different scattering properties, and also for a sample of ground glass.

Under this model, the true speckle intensity has a mean intensity of

$$\mu_I = (1 - \beta)\langle I_m \rangle. \quad (3.7)$$

The behavior of the measured intensity model presented in (3.4) was investigated further to determine its dependence upon exposure time, polarization, and the effect of stray scattered light from the experimental setup on the measured results. In Fig. 3.6(a) the measured intensity histograms using increasing CCD exposures times of 150 ms, 300 ms, 450 ms, and 600 ms are plotted. This is equivalent to increasing the mean of the measured intensity, because the mean intensity is proportional to the CCD exposure time, and gives mean intensities $\langle I_m \rangle$ of 157, 314, 471, and 627

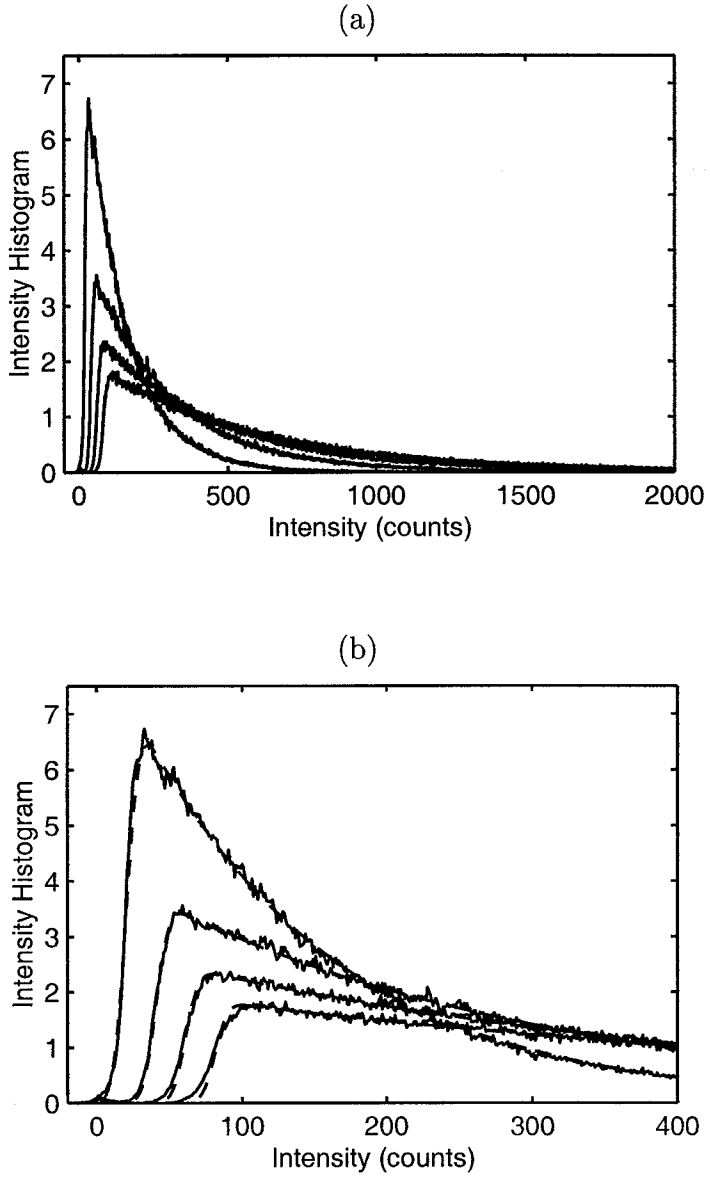

Fig. 3.6. (a) Measured intensity histograms having different means obtained by using CCD camera exposure times of 150 ms, 300 ms, 450 ms, and 600 ms. (b) The same data of (a) plotted on a scale to highlight the low level intensities (solid lines). The empirical model of (3.4) with $\beta = 0.13$ and $\sigma_n = 7$ counts for the histogram of each exposure time (dashed lines).

counts, respectively. Figure 3.6(b) is the same data of Fig. 3.6(a) plotted on a different scale to highlight the lower intensity values. The dashed lines of Fig. 3.6(b), which directly overlay the measured data, are the empirical model of (3.4) with $\beta = 0.13$ and $\sigma_n = 7$ counts. As can be seen from these plots, the empirical model provides an excellent fit to the measured data over a wide range of mean intensities.

The proposed empirical model was also found to accurately describe the measured speckle intensity for different states of polarization. A single 6 mm slab of a random medium with a scattering coefficient of $\mu_s' = 13\,\mathrm{cm}^{-1}$ was illuminated with linearly polarized light. The polarizer in Fig. 3.1 was adjusted to measure the same linear polarization state (co-polarized), the orthogonal linear polarization state (cross-polarized), and then removed to measure all polarization states (un-polarized). The measured speckle intensity patterns and histograms are shown in Fig. 3.7.

As can be seen from the data presented in Fig. 3.7, the agreement with the measurements and the empirical model is very good. The un-polarized intensity speckle pattern is the sum of the co-polarized speckle intensity, with mean μ_{co}, and the cross-polarized speckle intensity, with mean μ_{cr}. For $\mu_{\mathrm{co}} \neq \mu_{\mathrm{cr}}$, the pdf for the un-polarized speckle intensity is given by [47]

$$p_I(I) = \frac{1}{\mu_{\mathrm{co}} - \mu_{\mathrm{cr}}} \exp(-I/\mu_{\mathrm{co}}) - \frac{1}{\mu_{\mathrm{co}} - \mu_{\mathrm{cr}}} \exp(-I/\mu_{\mathrm{cr}}), \tag{3.8}$$

when the co-polarized and cross-polarized fields are both described by circular complex Gaussian statistics. The un-polarized intensity mean is $\mu_{\mathrm{co}} + \mu_{\mathrm{cr}}$. The dashed line in Fig. 3.7(f) is (3.8) with $\mu_{\mathrm{co}} = 194$ and $\mu_{\mathrm{cr}} = 178$, after taking into account the transmission coefficient of 0.92 measured for the the polarizer. The empirical model for the measured un-polarized intensity histogram is given by the convolution of (3.8) with (3.3), which is plotted as the dashed curve overlaying the measured data in Fig. 3.7.

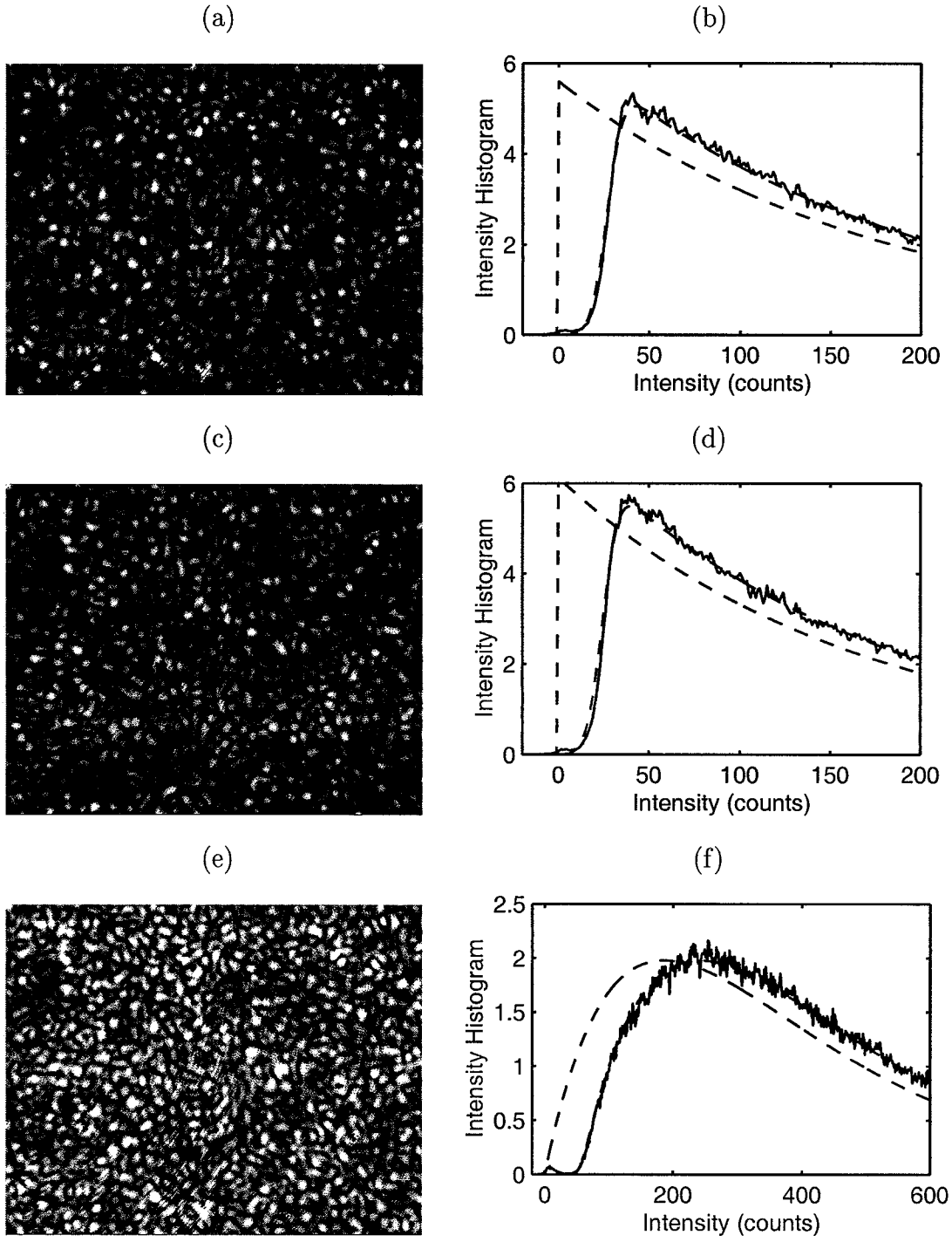

Fig. 3.7. (a) Speckle intensity for co-polarized light. (b) Measured intensity histogram for co-polarized light (solid line). Empirical model with $\beta = 0.13$ and $\sigma_n = 7$ is overlaid on the measured data (overlaid dashed line). The theoretical intensity pdf is also shown (dashed line). (c) As for (a) but for cross-polarized data. (d) As for (b) but for cross-polarized data. (e) As for (a) but for un-polarized data. (f) As for (b) but for un-polarized data.

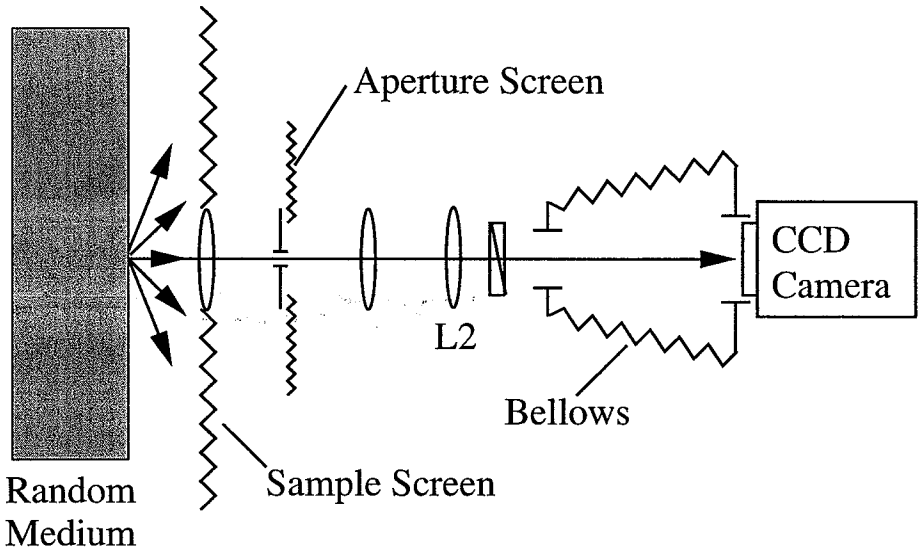

Fig. 3.8. A schematic showing the placement of dark-cloth screens and bellows used in the imaging optics to eliminate stray scattered light from the image plane of the CCD.

The experiments in this study involved measuring the scattered light from a small area on the output face of a random medium in a transmission geometry. The random medium scatters the focused input beam into all directions, and all the light not coming from the small imaging area is considered undesirable stray light. Significant measures needed to be taken to eliminate this stray light from the experimental setup. Figure 3.8 shows a schematic of the various black-cloth light screens and bellows employed to eliminate the stray scattered light. There was a large sample screen located at the first lens of the imaging spatial filter to block most of the scattered light from the random medium. An aperture screen around the spatial filter aperture (at the Fourier plane) was used to ensure that only light that passes through the aperture is imaged, and a bellows around the camera eliminated scattered stray light reflected from the optical table surface entering the camera imaging plane.

The effect of each of these stray light screening measures on the speckle pattern statistics was investigated. The results are presented in Fig. 3.9 and show a very good agreement with the empirical intensity statistics model of (3.4). As each of the stray

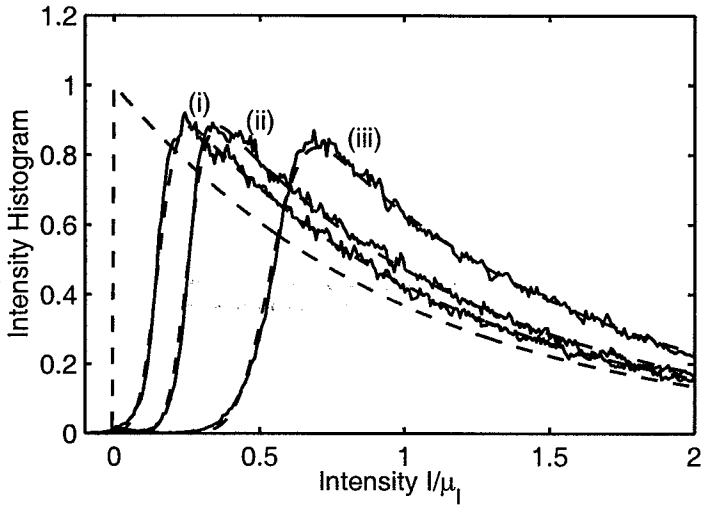

Fig. 3.9. Intensity histograms highlighting the effects of the light screens shown in Fig. 3.8 (solid lines). (i) With aperture screen, with bellows. (ii) With aperture screen, no bellows. (iii) No aperture screen, no bellows. Also shown overlaying the measured data are the histograms calculated from the empirical model (overlaid dashed lines). The theoretical ideal negative exponential pdf (dashed line).

Table 3.1
The β and σ_n parameters of the empirical model for the measured intensity pdf, and the measured mean intensity $\langle I_m \rangle$, for the data presented in Fig. 3.9.

Screens present	$\langle I_m \rangle$	β	σ_n
(i) With aperture screen, with bellows	157	0.13	7
(ii) With aperture screen, no bellows	170	0.20	7
(iii) No aperture screen, no bellows	209	0.35	12

light screening measures were removed, the parameters used to model the anomalous offset intensity, β and σ_n, were found to increase, with the values summarized in Table. 3.1. With all the screen measures in place, the smallest achievable intensity offset values obtained were $\beta = 0.13$ and $\sigma_n = 7$. Without the aperture screen and bellows, the values increased to $\beta = 0.35$ (a significant increase) and $\sigma_n = 12$, but the intensity statistics are still very well modeled by (3.4). From this, it can be concluded

that the anomalous intensity offset can be well modeled as stray light, but this does not imply that it is caused by stray light.

3.4.1 Speckle Size Measurements

Assuming that the speckle statistics are ergodic, we estimate the ensemble statistics by spatially sampling the measured speckle intensity. To ensure accurate sampling of the underlying speckle field, the detection area (CCD pixel size) needs to be small compared with the width of the speckle intensity spatial autocorrelation function [90, 91]. The spatial autocorrelation function provides a measure of the average "speckle size" and is defined by [47]

$$R_I(\Delta r) = \frac{\langle I(r_0 + \Delta r) I(r_0) \rangle}{\langle I \rangle^2}, \tag{3.9}$$

where $I(r_0)$ is the speckle intensity at spatial location r_0 in the image plane and Δr is a small spatial offset. The speckle intensity spatial autocorrelation of (3.9) is determined by the point spread function (PSF) of the imaging optics and the spatial structure of the speckle field in the object plane [60, 61], and was discussed in Section 2.1.2. For our imaging optics shown in Fig. 3.1, we calculate $R_I(\Delta r)$ for a circular complex Gaussian field in the object plane whose spatial structure is very small compared with the PSF of the imaging optics, using scalar diffraction theory under the Fresnel approximation, to give

$$R_I(\Delta r) = \left[1 + \left| \mathrm{jinc}\left(\frac{D \Delta r}{2 M \lambda f} \right) \right|^2 \right]. \tag{3.10}$$

The calculated spatial autocorrelation function of several speckle images measured using varying sizes for the spatial filter aperture diameter D are plotted in Fig. 3.10. For the imaging geometry of Fig. 3.1, the parameters of $\lambda = 850\,\mathrm{nm}$, $f = 50\,\mathrm{mm}$, and $M = 10$ were used in (3.10). The speckles have average diameters of $700\,\mu\mathrm{m}$ for Fig. 3.10(a), $200\,\mu\mathrm{m}$ for Fig. 3.10(c), and $60\,\mu\mathrm{m}$ for Fig. 3.10(e).

To ensure accurate statistics, a large number of independent measurements are usually required. For our measurements, this equates to having a large number of

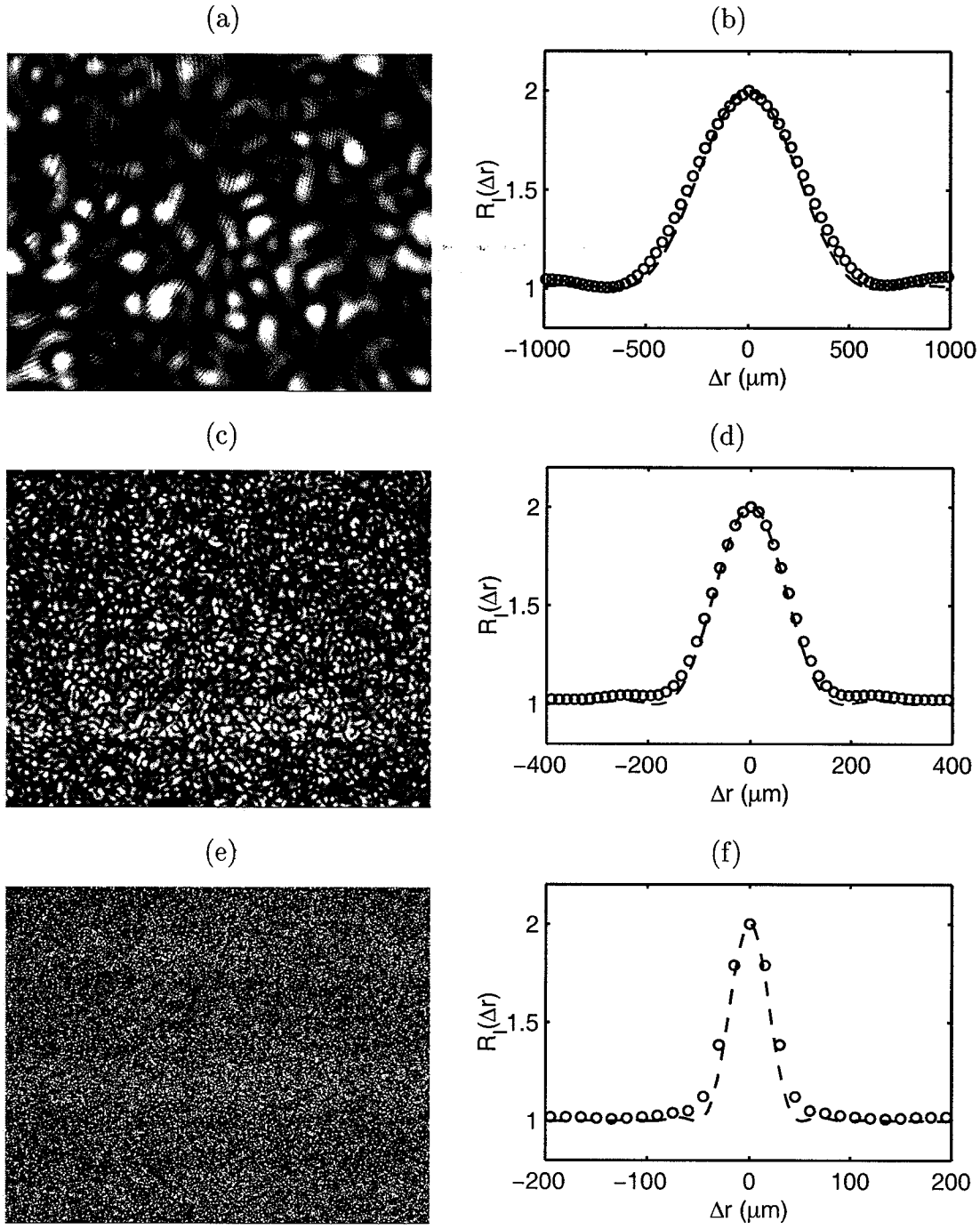

Fig. 3.10. The effect of the spatial filter aperture diameter D, of Fig. 3.1, on the measured speckle patterns. (a) Speckle pattern for $D = 0.8\,\text{mm}$. (b) Measured spatial autocorrelation (symbols) and calculated (dashed line). (c) As for (a) with $D = 2.8\,\text{mm}$. (d) As for (b) with $D = 2.8\,\text{mm}$. (e) As for (a) with $D = 10\,\text{mm}$. (f) As for (b) with $D = 10\,\text{mm}$.

independent speckles in an image obtained by the CCD. The number of independent samples is not given by the number of CCD pixels, but by the ratio of the CCD area to the average area of an individual speckle. For Fig. 3.10(c), we can approximate the average speckle area by $200\,\mu\text{m} \times 200\,\mu\text{m}$, and by comparing this with the CCD imaging area of $15\,\text{mm} \times 12\,\text{mm}$, we have approximately 4500 independent intensity samples in a measured speckle pattern. This proved to be sufficient for estimating the ensemble statistics. Of course, one could make the speckle size smaller by increasing the aperture diameter D of the spatial filter in the imaging optics of Fig. 3.1. However, if the average speckle size begins to approach the CCD pixel size, then the speckle intensity statistics will not be accurately sampled, as is the case with the speckle image of Fig. 3.10(e). The speckle image of Fig. 3.10(a) accurately samples the speckle intensity, but there are too few independent speckle spots to estimate the ensemble statistics. Using an aperture of diameter $D = 2.8\,\text{mm}$, giving the speckle image of Fig. 3.10(c), was found to be close to the optimum for estimating the ensemble statistics, between the two extreme cases.

3.5 Fabry-Perot Interferometer

To enable accurate measurement of the change in the laser center frequency, and to measure the power spectrum of the synthesized variable coherence source, a scanning Fabry-Perot interferometer was used. The Fabry-Perot interferometer consists of two high-reflectivity planar mirrors whose separation can be precisely controlled. One mirror is fixed, while the other can be scanned over a distance of about $1\,\mu\text{m}$ by a piezoelectric transducer, to which a ramp voltage is applied. A transmission peak occurs when the mirror separation is precisely an integer multiple of half-wavelengths. The tunable laser diode was amplitude modulated at 500 MHz and the output applied to the Fabry-Perot. The Fabry-Perot response is shown in Fig. 3.11. In Fig. 3.11(b), the frequency difference between each peak is 500 MHz, which allows the piezoelectric ramp voltage to be calibrated to frequency change in the Fabry-Perot transmission

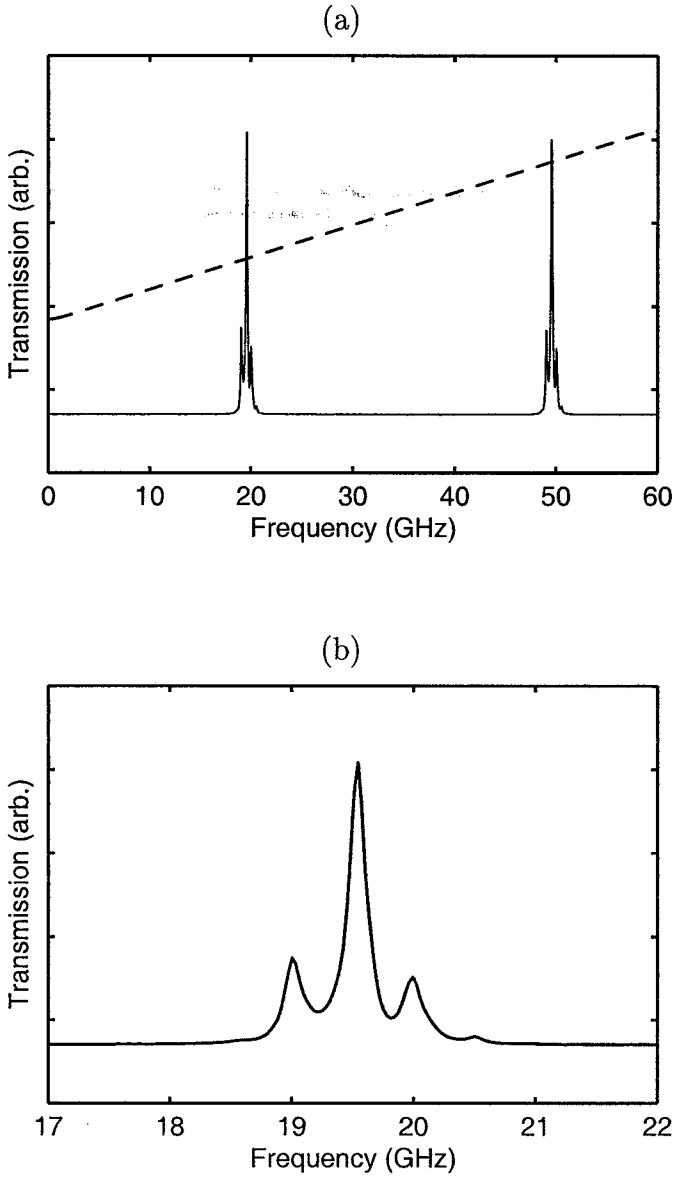

Fig. 3.11. (a) The transmission of the Fabry-Perot interferometer showing two transmission peaks. The FSR is approximately 30 GHz. The dashed line is proportional to the mirror separation that is scanned via piezoelectric transducers. (b) A zoom in of the transmission profile for the laser diode amplitude modulated at 500 MHz, with the two side-bands clearly visible. These side-bands were used to calibrate the Fabry-Perot frequency scan.

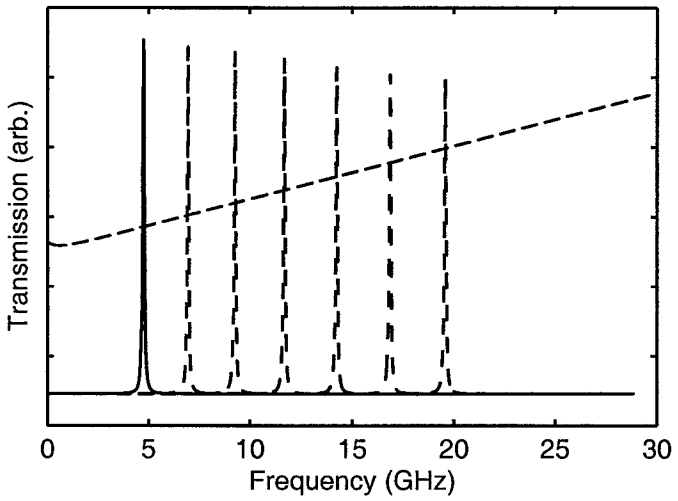

Fig. 3.12. The transmission of the Fabry-Perot as the laser frequency is scanned.

peak. The free spectral range (FSR) was calculated to be 30.64 GHz, which agrees with the FSR of 30 GHz expected for a 5 mm mirror separation that the mirrors were approximately set to.

Figure 3.12 shows the center frequency of the laser change, as recorded by a shift in the Fabry-Perot transmission peak. This data is recorded for each laser frequency scan used to obtain a speckle image.

3.6 Data Processing

The measured intensity statistics were found to be well modeled by (3.4), which accounts for the anomalous intensity offset. To correct the measured intensities for the anomalous offset intensity, the mean value of this offset, $\eta_I = \beta\langle I_m\rangle$, was subtracted. The measured intensity can be now modeled as having a pdf given by the ideal negative exponential of (3.2) convolved with a zero-mean Gaussian of variance σ_n^2. The net effect is that the measured intensity statistics now are identical in form to the ideal statistics, but as if they were measured using a CCD camera with greater read-noise than it actually has. Subtracting the mean intensity offset was found to

be sufficient for correcting the data, as supported by the results in Chapter 4, and was performed for all measured intensities.

It is also possible to show how the mean intensity offset affects the frequency correlations of normalized intensity given by (2.40) and (2.41). Let the measured intensities at frequencies ν_i be denoted by $I_{mi} = I_m(\nu_i)$ and the corresponding true intensity be denoted by $I_{ti} = I_t(\nu_i)$. Defining the normalized intensities by

$$\tilde{I}_{mi} = \frac{I_{mi} - \langle I_m \rangle}{\langle I_m \rangle} \quad \text{and} \quad \tilde{I}_{ti} = \frac{I_{ti} - \mu_I}{\mu_I}, \tag{3.11}$$

where the mean intensities $\langle I_{mi} \rangle = \langle I_m \rangle$ and $\langle I_{ti} \rangle = \mu_I$ are assumed frequency independent. The normalized measured intensity and normalized true intensity correlations are then related by

$$\begin{aligned} \tilde{I}_m &= (1-\beta)\tilde{I}_t \\ \langle \tilde{I}_{mi}\tilde{I}_{mj} \rangle &= (1-\beta)^2 \langle \tilde{I}_{ti}\tilde{I}_{tj} \rangle \\ \langle \tilde{I}_{mi}\tilde{I}_{mj}\tilde{I}_{mk} \rangle &= (1-\beta)^3 \langle \tilde{I}_{ti}\tilde{I}_{tj}\tilde{I}_{tk} \rangle. \end{aligned} \tag{3.12}$$

The effect of the intensity offset on the frequency correlations is to simply scale the true intensity correlations by a factor dependent upon β.

3.7 Summary

The experimental setup used to measured speckle intensity patterns from random media has been described and characterized. The imaging optics was designed to accurately resolve the speckle intensity, by designing the point spread function to produce a speckle size in the image plane 10–15 times the size of a CCD pixel. This also provided a sufficient number of independent speckle spots to accurately estimate the ensemble statistics.

An anomalous intensity offset was also observed in the measured speckle intensity. This offset could not be eliminated, however, its effect was well modeled and found to be minimal on the desired speckle intensity statistics and correlations. The measured data was corrected by subtracting the mean of this offset from all speckle patterns.

4. EXPERIMENTAL RESULTS

4.1 Speckle Correlation Results

Speckle images were measured for 25 discrete laser frequencies in order to calculate the intensity frequency correlations of (2.40) and (2.41). As the laser frequency is scanned the spatial structure of the measured speckle intensity pattern will change due to the change in accumulated random phase with frequency. This behavior is nicely shown in Fig. 4.1, where the insets show the lower left corner of the speckle pattern change for the different laser center frequencies.

Measurements were performed for two homogeneous sample thicknesses of $d = 6\,\text{mm}$ and $d = 12\,\text{mm}$. (The sample of thickness $d = 12\,\text{mm}$ was made from two identical slabs of thickness $d = 6\,\text{mm}$.) For the sample thickness of $d = 6\,\text{mm}$, frequency increments of $\delta\nu = 0.8\,\text{GHz}$ between each measured speckle pattern were used, and for the sample of thickness $d = 12\,\text{mm}$, frequency increments of $\delta\nu = 0.4\,\text{GHz}$ were used.

The second-order intensity correlation of (2.40) is only dependent upon the frequency difference between measurements. Therefore, we averaged each frequency combination pair from the available data set that gave the same frequency difference to form the intensity second-order frequency correlation data point for that particular frequency difference. Denoting the normalized intensity sample at each frequency increment by $\tilde{I}_i = \tilde{I}(\nu + i\delta\nu)$ for $i = 0, 1, \ldots, N-1$, with $N = 25$, then the second-order correlation of (2.40), averaged over all possible combinations, is estimated by

$$\langle \tilde{I}(\nu)\tilde{I}(\nu + \Delta\nu)\rangle = \frac{1}{N-i}\sum_{j=0}^{N-1-i}\langle \tilde{I}_j\tilde{I}_{j+i}\rangle_{\text{est}}, \tag{4.1}$$

with $\Delta\nu = i\delta\nu$ and $i = 0, 1, \ldots, N-1$. The quantity $\langle \tilde{I}_j\tilde{I}_{j+i}\rangle_{\text{est}}$ is the estimate of the second-order intensity correlation evaluated for frequencies $\nu + j\delta\nu$ and $\nu + (j +$

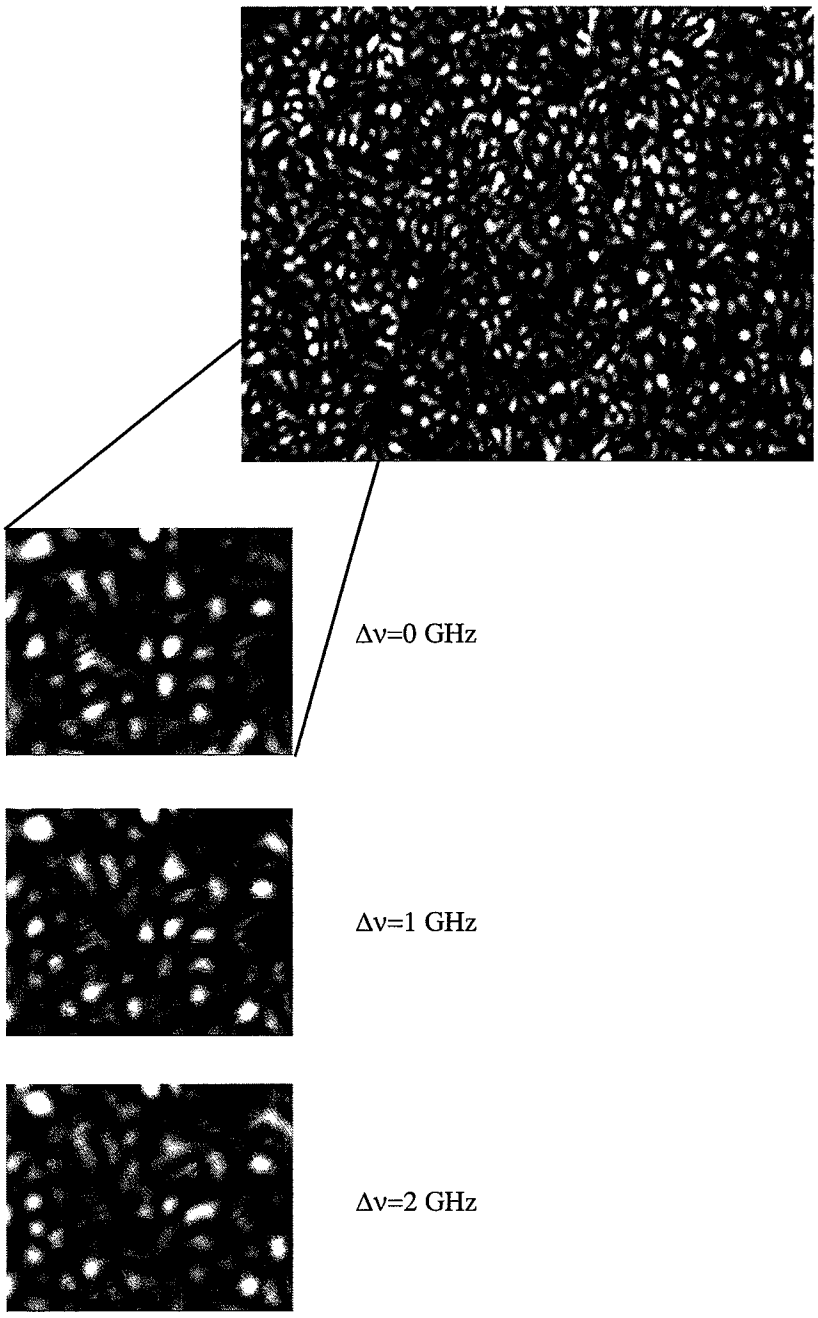

Fig. 4.1. A typical measured speckle pattern. The insets show an expanded image of the lower left sixteenth of the speckle intensity pattern, $I(\nu + \Delta\nu)$, as $\Delta\nu$ is varied. This shows the speckle pattern slowly de-correlate with frequency.

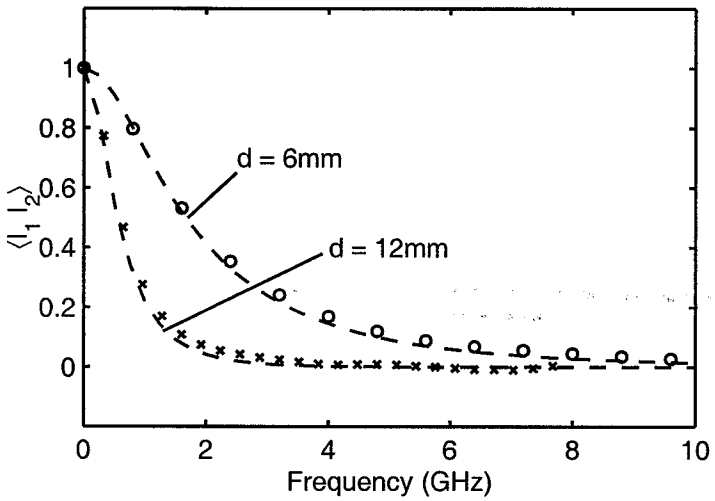

Fig. 4.2. A plot of the measured second-order intensity frequency correlation defined in (4.1) for two slab thicknesses of a scattering random medium (symbols). Excellent agreement with the second-order intensity correlation of (2.40), calculated using an analytic diffusion model for the temporal response $p(t)$, with values of $\mu_s' = 13\,\mathrm{cm}^{-1}$ and negligible absorption ($\mu_a = 0\,\mathrm{cm}^{-1}$) was obtained (dashed lines).

$i)\delta\nu$, formed by calculating the spatial correlation of the two speckle images at these frequencies. The measured speckle intensities are multiplied on a pixel-by-pixel basis then summed over all pixels and divided by the total number of pixels,

$$\langle \tilde{I}_j \tilde{I}_{j+i} \rangle_{\mathrm{est}} = \frac{1}{N_x N_y} \sum_{x=1}^{N_x} \sum_{y=1}^{N_y} \tilde{I}_j[x,y] \tilde{I}_{j+i}[x,y], \tag{4.2}$$

where $\tilde{I}_j[x,y]$ is the intensity value at the $[x,y]$ pixel location for the frequency of $\nu + j\delta\nu$. The averaging procedure of (4.1) will reduce the sampling error of the small frequency differences more than for the larger frequency differences because there are more frequency pairs to average. Of course, one may increase the range of the laser diode frequency scan to be much greater than the frequency range of interest, increasing the number of available frequency pairs used to form the average.

The results for the measured second-order intensity correlations of (4.1) are plotted in Fig. 4.2 for the two slab thicknesses of $d = 6\,\mathrm{mm}$ and $d = 12\,\mathrm{mm}$. Also plotted is the second-order intensity correlation of (2.40), evaluated by using the temporal response $p(t)$ calculated from (2.67) under the diffusion approximation for a homogeneous slab

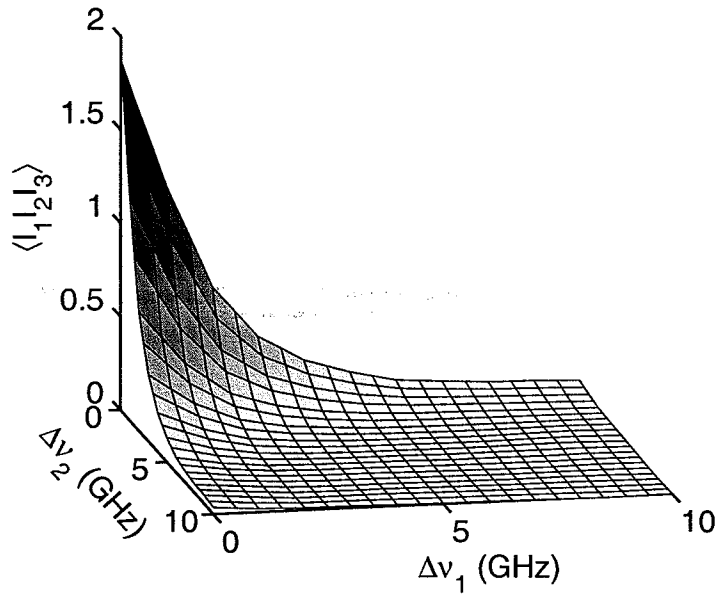

Fig. 4.3. A plot of the measured third-order intensity correlation defined by (4.3) for the sample of thickness $d = 6\,\text{mm}$. This data is equal to twice the real part of the bispectrum of $p(t)$.

and taking a Fourier transform to obtain the Fourier magnitude $|P(\Delta\nu)|$. There is very good agreement between our measured speckle correlations and the analytic diffusion model, with $\mu_s' = 13\,\text{cm}^{-1}$ and negligible absorption ($\mu_a = 0\,\text{cm}^{-1}$), for each slab thickness d.

To calculate the third-order intensity correlation of (2.41), we averaged each frequency triplet from the available data set of measured intensities that gave the same frequency differences for $\Delta\nu_1$ and $\Delta\nu_2$ to form each measured third-order correlation data point. Averaging all possible combinations, gives the measured third-order correlation

$$\langle \tilde{I}(\nu)\tilde{I}(\nu+\Delta\nu_1)\tilde{I}(\nu+\Delta\nu_1+\Delta\nu_2)\rangle = \frac{1}{N-i-j}\sum_{k=0}^{N-1-i-j}\langle \tilde{I}_k\tilde{I}_{k+i}\tilde{I}_{k+i+j}\rangle_{\text{est}}, \qquad (4.3)$$

where $\Delta\nu_1 = i\delta\nu$, $\Delta\nu_2 = j\delta\nu$, and $i, j = 0, 1, \ldots, N-1$ with $i + j \leq N-1$. The quantity $\langle \tilde{I}_k\tilde{I}_{k+i}\tilde{I}_{k+i+j}\rangle_{\text{est}}$ is the estimate of the third-order intensity correlation evaluated at the frequencies of $\nu+k\delta\nu$, $\nu+(k+i)\delta\nu$, and $\nu+(k+i+j)\delta\nu$ by calculating

the spatial correlation between the three speckle images at these frequencies, as for the second-order calculation of (4.2), and is given by

$$\langle \tilde{I}_k \tilde{I}_{k+i} \tilde{I}_{k+i+j} \rangle_{\text{est}} = \frac{1}{N_x N_y} \sum_{x=1}^{N_x} \sum_{y=1}^{N_y} \tilde{I}_k[x,y] \tilde{I}_{k+i}[x,y] \tilde{I}_{k+i+j}[x,y]. \tag{4.4}$$

Figure 4.3 shows a plot of the third-order intensity correlation of the measured data for the homogeneous slab of thickness $d = 6\,\text{mm}$. There is symmetry about line of $\Delta\nu_1 = \Delta\nu_2$ in this plot, as expected for the bispectrum of a real signal.

4.1.1 Reconstructed Temporal Response

To reconstruct the temporal response of a random medium, we first determine the Fourier magnitude using second-order correlations, and second, calculate the Fourier phase from third-order correlations, then combine these results and perform an inverse Fourier transform. Figure 4.4(a) shows the reconstructed Fourier magnitude for the two sample thicknesses. The Fourier magnitude is related to the second-order intensity correlation by (2.40), and was obtained by taking the square root of the measured second-order correlation calculated by (4.1) and shown in Fig. 4.2. The reconstructed Fourier phase is plotted in Fig. 4.4(b) for both sample thicknesses. We obtained this result by using the measured second-order and third-order correlations of (4.1) and (4.3) in (2.80) to estimate the bispectral phase. Then we calculated the Fourier phase from the bispectral phase using (2.79). The arbitrary linear phase was chosen to overlap the reconstructed Fourier phase with the Fourier phase obtained from using an analytic diffusion approximation solution for the temporal response, which is also shown in Fig. 4.4(b).

The noticeable deviation of the reconstructed Fourier phases from the analytic results for the diffusion approximation at a frequency of 12 GHz for the sample thickness of $d = 6\,\text{mm}$, and at a frequency of 5 GHz for the sample thickness of $d = 12\,\text{mm}$, are due to the measured second-order and third-order intensity correlations becoming very small and susceptible to experimental noise, thus causing errors in the bispectral phase calculated using (2.80).

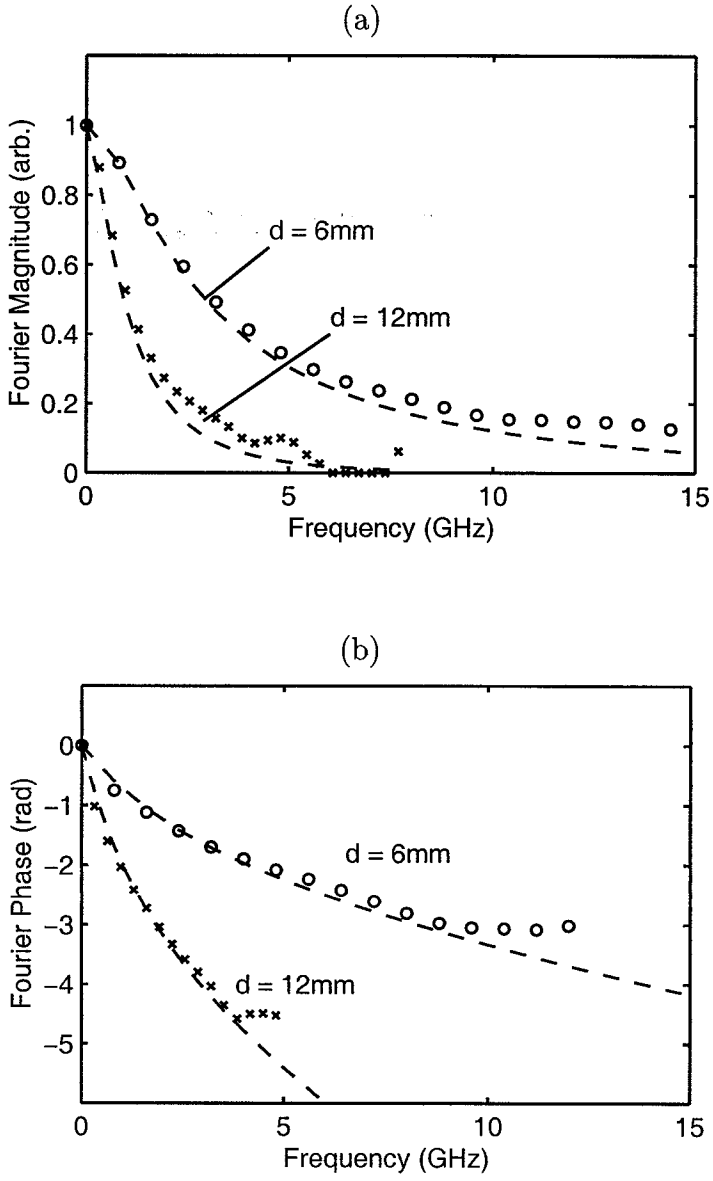

Fig. 4.4. (a) The reconstructed Fourier magnitude of the temporal response for the two sample thicknesses using measured data (symbols). The Fourier magnitude calculated by using an analytic diffusion model for the temporal response with $\mu_s' = 13\,\mathrm{cm}^{-1}$ and $\mu_a = 0\,\mathrm{cm}^{-1}$ for each thickness (dashed lines). (b) The reconstructed Fourier phase of the temporal response using measured data (symbols), and the Fourier phase calculated using the diffusion model, for each sample thickness (dashed lines).

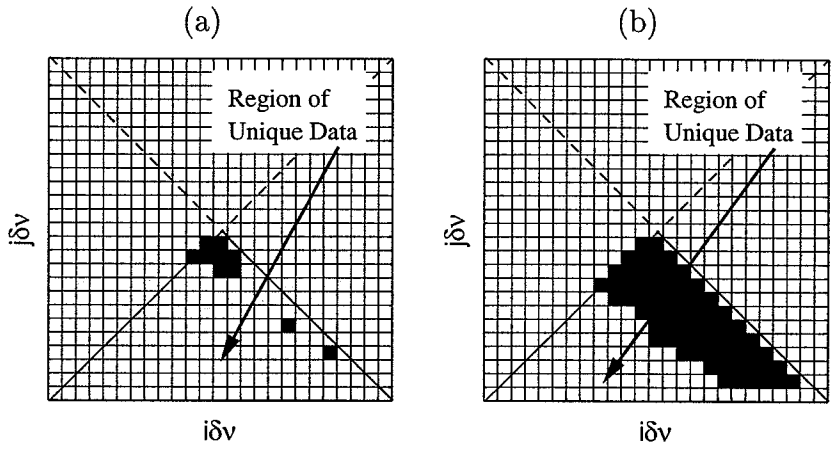

Fig. 4.5. (a) The black regions indicate the discrete frequencies for which the bispectral phase of (2.80) could not be calculated, for the sample of thickness $d = 6\,\text{mm}$. (b) As in (a) but for the sample of thickness $d = 12\,\text{mm}$.

It was also found in some cases that the bispectral phase could not be calculated from the measured second-order and third-order intensity correlations, particularly for the larger frequency differences. This occurs when the argument of the inverse cosine of (2.80) becomes larger than unity, due to the influence of noise. An example of this is shown in Fig. 4.5 for the two sample thicknesses of $d = 6\,\text{mm}$ and $d = 12\,\text{mm}$. As can be seen from these plots, the bispectral phase could not be determined for the large frequency differences. In these cases, the second-order and third-order correlations are themselves very small and susceptible to experimental noise, and also there are fewer combinations to average over to form the data from (4.1) and (4.3).

We applied an inverse FFT to the reconstructed Fourier magnitude and phase data giving the reconstructed temporal responses shown in Fig. 4.6(a) for the sample thickness of $d = 6\,\text{mm}$, and in Fig. 4.6(b) for the sample thickness of $d = 12\,\text{mm}$. As can be readily seen, these results agree very well with those expected from the diffusion approximation model. We can also see that the width of the temporal response scales with sample thickness in a manner predicted by a diffusion approximation model. The oscillations in the reconstructed temporal response are artifacts due to the finite frequency range over which the Fourier phase was reconstructed. These frequency

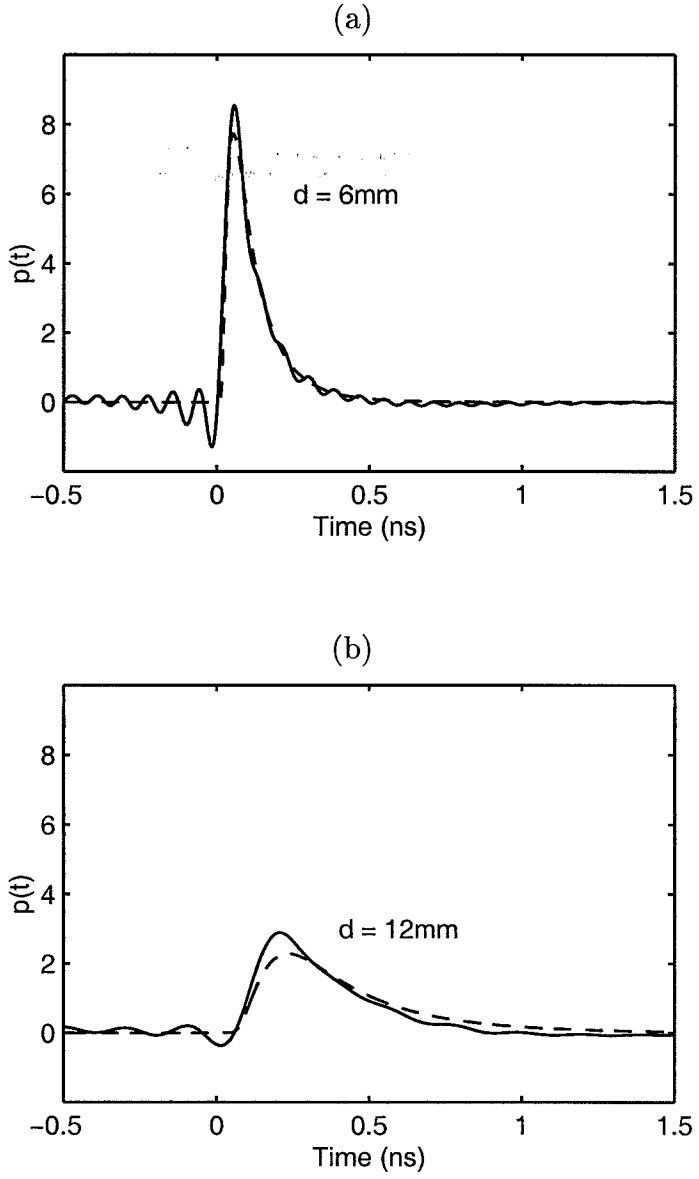

Fig. 4.6. The reconstructed temporal response obtained by taking an inverse FFT of the Fourier magnitude and phase data presented in Fig. 4.4 (solid lines). Each sample thickness gives excellent agreement with a diffusion approximation model for the temporal response (dashed lines).

ranges are shown in Fig. 4.4(b) and are 12 GHz for the sample of thickness $d = 6\,\text{mm}$, and 5 GHz for the sample of thickness $d = 12\,\text{mm}$.

4.2 Streak Camera Results

We confirmed the validity of the temporal response obtained using third-order speckle correlations by directly measuring the intensity temporal response defined in (2.51) using a streak camera. An ultrafast mode-locked Ti:Sapphire laser with a pulse width of approximately 200 fs was used as the input excitation. The center wavelength of the laser was 835 nm, which is a 2% difference in wavelength to the 850 nm used for the speckle frequency correlation experiments. This small difference in wavelength will cause a slight change in the scattering properties of the random medium (approximately 7% based on the λ^{-4} dependence of Rayleigh scattering), however the data shows that these effects are minimal and we shall neglect this small difference.

The streak camera was used in synchroscan mode to obtain the intensity temporal response data. The imaging optics used for the streak camera measurements is different to the configuration shown in Fig. 3.1 for the speckle measurements. It was changed to a single achromatic lens, of focal length 50 mm, and an adjustable iris aperture of diameter 4 mm placed at the lens. The lens was positioned to give a magnification factor of 10 from the object place (output face of the random medium sample) to the image plane (5 mm $\times$ 60 μm input slit of the streak camera). This enabled us to collect sufficient light from a small area on the output face of the random medium. Figure 4.7(a) shows the measured streak camera data for the sample of thickness $d = 6\,\text{mm}$, with the reconstructed result from the third-order speckle correlation technique overlaid. The measured streak camera data for the sample of thickness $d = 12\,\text{mm}$ is shown in Fig. 4.7(b). These results clearly show that the two measurement techniques are in excellent agreement.

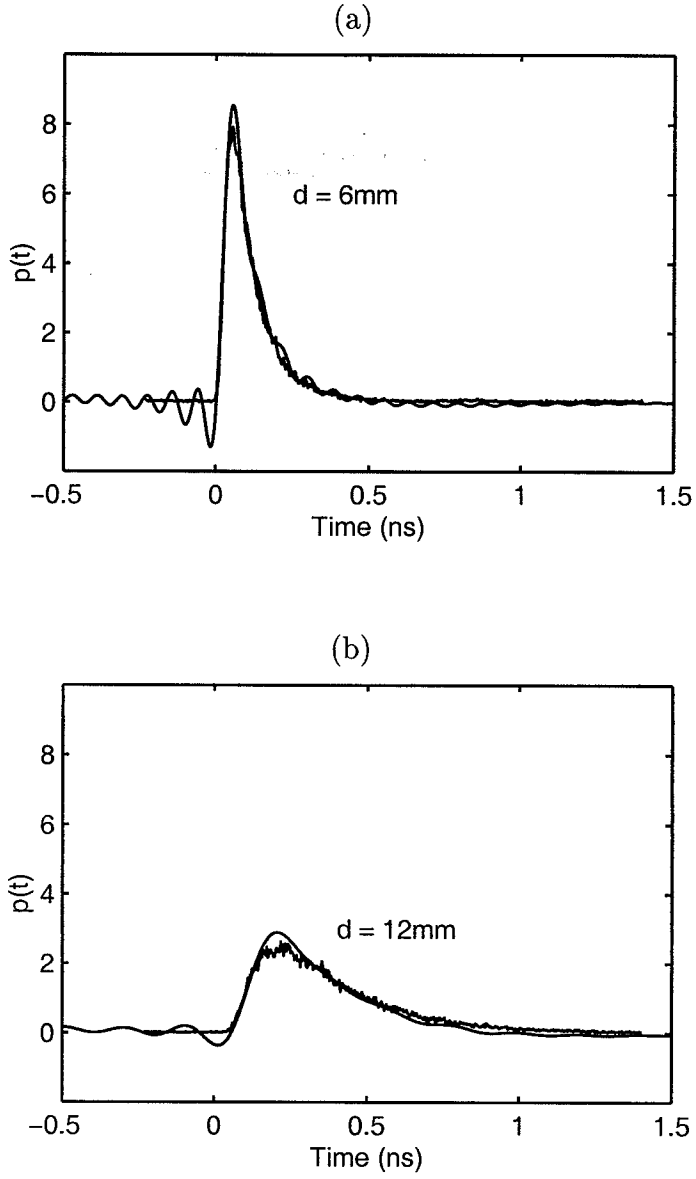

Fig. 4.7. Plots of the intensity temporal response of (2.51) directly measured using a streak camera, for each sample thickness. Overlaid are the temporal responses reconstructed using third-order speckle correlations, given in Fig. 4.6, showing excellent agreement.

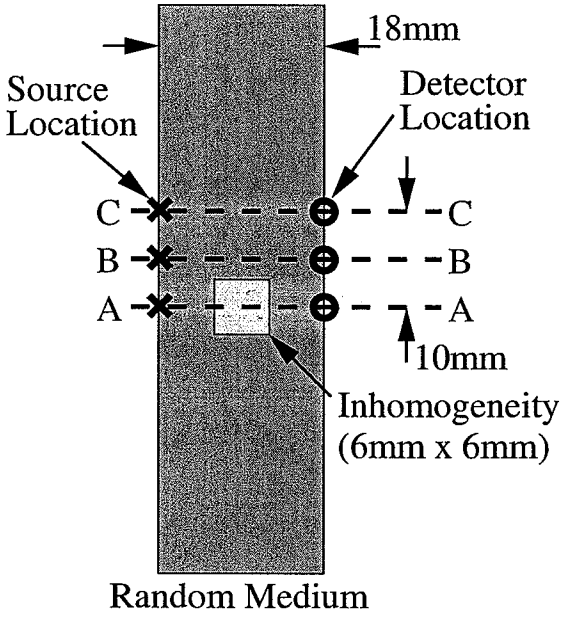

Fig. 4.8. Cross-section of inhomogeneous random medium sample. The background has a scattering coefficient of $\mu_s' = 13\,\mathrm{cm}^{-1}$, and the less scattering inhomogeneity has an estimated scattering coefficient of $\mu_s' = 4\,\mathrm{cm}^{-1}$. The source-detector location combinations used are along the axes of A–A, B–B, and C–C, each separated by 5 mm.

4.3 Inhomogeneous Sample

We also measured second-order and third-order speckle correlations for an inhomogeneous sample, whose cross-section is shown in Fig. 4.8. This sample, of total thickness 18 mm, was constructed from three sheets of thickness 6 mm and area 140 mm × 140 mm of the same scattering white acrylic (with $\mu_s' = 13\,\mathrm{cm}^{-1}$) used for the previous measurements that provided the data of Figs. 4.1–4.7. Centrally located within the background material was an inhomogeneity with cross-sectional dimensions of 6 mm × 6 mm, and a length of 140 mm. This inhomogeneity was less scattering than the background material, and was also a white acrylic but with an estimated scattering coefficient of $\mu_s' = 4\,\mathrm{cm}^{-1}$.

Three source-detector location combinations were used for measuring speckle correlation data, and are shown in Fig. 4.8. The first source-detector location combina-

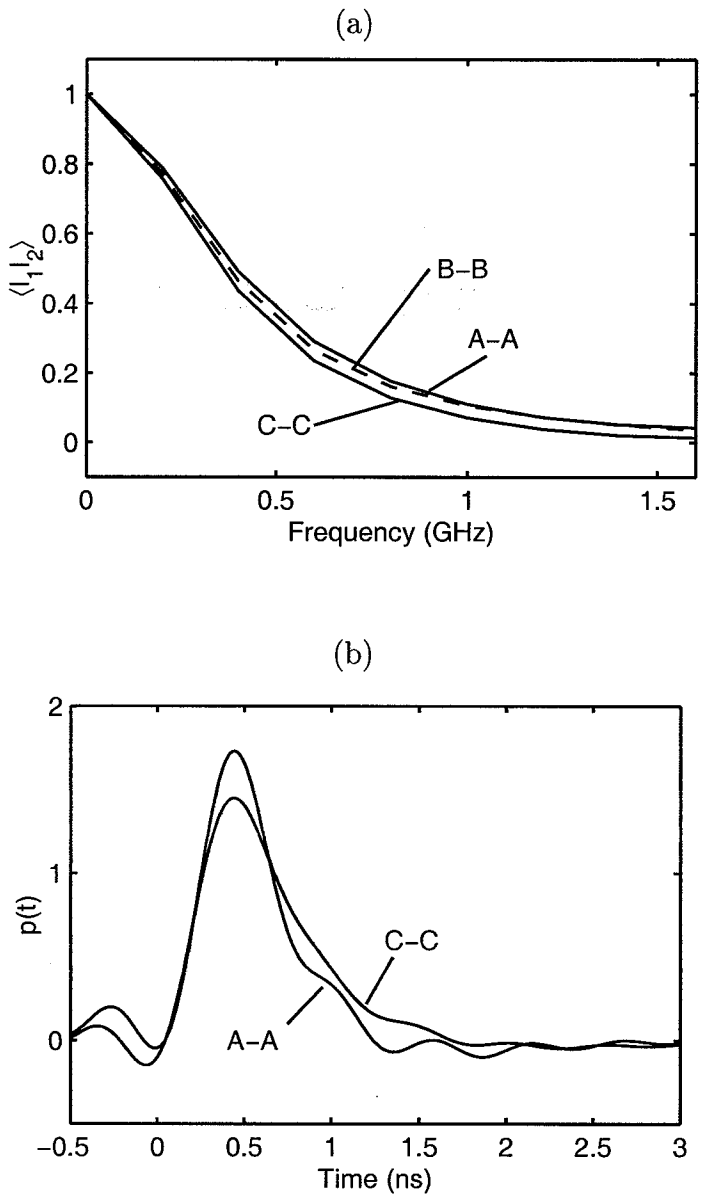

Fig. 4.9. (a) The measured second-order intensity correlations for the inhomogeneous sample shown in Fig. 4.8 for the source-detector location combinations of A–A, B–B, and C–C. (b) The reconstructed temporal responses for the inhomogeneous sample for the source-detector locations of A–A and C–C.

tion, denoted by A–A, was centrally located about the inhomogeneity. The second combination, denoted by B–B, was offset by 5 mm from A–A and whose "line-of-sight"

did not pass through the inhomogeneity. The third combination, denoted by C–C, was offset by 10 mm from A–A.

The second-order intensity correlation measurements for the three source-detector locations are shown in Fig. 4.9(a). The difference in the second-order intensity correlation for each source-detector location is seen to be small, but they display the correct trend for each plot as a function of frequency; the source-detector location of A–A encounters a greater volume of the less scattering inhomogeneity than source-detector combination C–C, thus it will have a broader second-order intensity correlation as a function of frequency. The source detector combination of B–B is geometrically between A–A and C–C in terms of the influence of the less scattering inhomogeneity, and hence the second-order intensity correlation as a function of frequency for B–B lies between the results for A–A and C–C as also seen in Fig. 4.9(a). The temporal responses for two source-detector locations are shown in Fig. 4.9(b), which were reconstructed by using both the second-order and third-order intensity correlations. We expect that the temporal response for each source-detector location will be different, since the time of flight distributions will be different due to the inhomogeneous distribution of scattering properties. For the source-detector location of A–A, the presence of the less scattering inhomogeneity will provide a greater volume of less scattering paths than for the C–C source-detector location, thus we expect the time of flight distribution for A–A to be narrower than for C–C, thus giving a narrower temporal response as is seen in Fig. 4.9(b).

4.4 Variable-Coherence Source

By using a tunable laser source, such as an external cavity laser diode, it is possible to synthesize a source with variable coherence properties[68]. This is achieved by modulating the center-frequency of the narrow-linewidth laser over some finite frequency range of $\Delta\nu_{\text{syn}}$, as shown in Fig. 4.10. When the center-frequency is modulated over this bandwidth at a rate much faster than the observation time of the

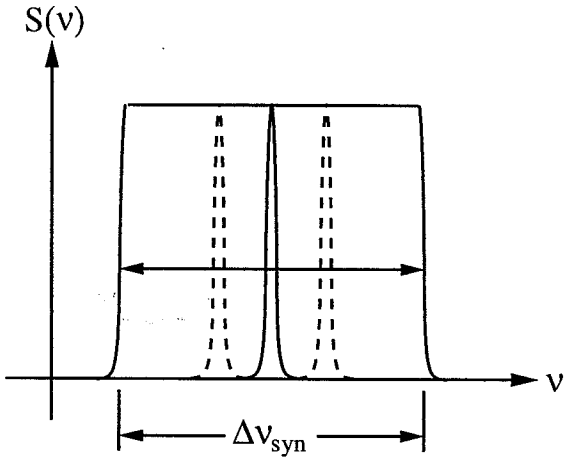

Fig. 4.10. The center-frequency of the narrow-linewidth laser diode is scanned over a range of $\Delta\nu_{\text{syn}}$ to synthesize a desired power spectral density.

detector, then the experiment will see a source with a power spectral density of width $\Delta\nu_{\text{syn}}$. For the experiments report here, which were performed in collaboration with McKinney[92], modulation rates of 200 Hz were used together with integration times for the CCD of about 1–2 s.

To demonstrate the effect that using a source with synthesized coherence properties has on the speckle statistics from a random medium, such as the contrast ratio defined by (2.54), the speckle intensity from a 9 mm thick slab with a scattering coefficient of $\mu_s' = 12.5\,\text{cm}^{-1}$ was measured using a source with synthesized linewidths of $\Delta\nu_{\text{syn}} = 5\,\text{MHz}$ and $\Delta\nu_{\text{syn}} = 10\,\text{GHz}$. The results are shown in Fig. 4.11. The speckle pattern of Fig. 4.11(a) is for the un-modulated source, which has a linewidth of approximately 5 MHz (effectively monochromatic) giving a contrast ratio of $C_I = 0.95$, whereas the speckle pattern Fig. 4.11(b) is for a synthesized linewidth of $\Delta\nu_{\text{syn}} = 10\,\text{GHz}$ and has a contrast ratio of $C_I = 0.47$. Both speckle patterns have the same mean intensity. Figure 4.11(c) shows the measured intensity histograms for both speckle patterns As can be readily seen, the effect of the synthesized linewidth is quite significant on the intensity statistics; the un-modulated source gives statistics close to negative exponential, expected for a monochromatic source, but the source of synthesized linewidth $\Delta\nu_{\text{syn}} = 10\,\text{GHz}$ produces statistics far from negative exponen-

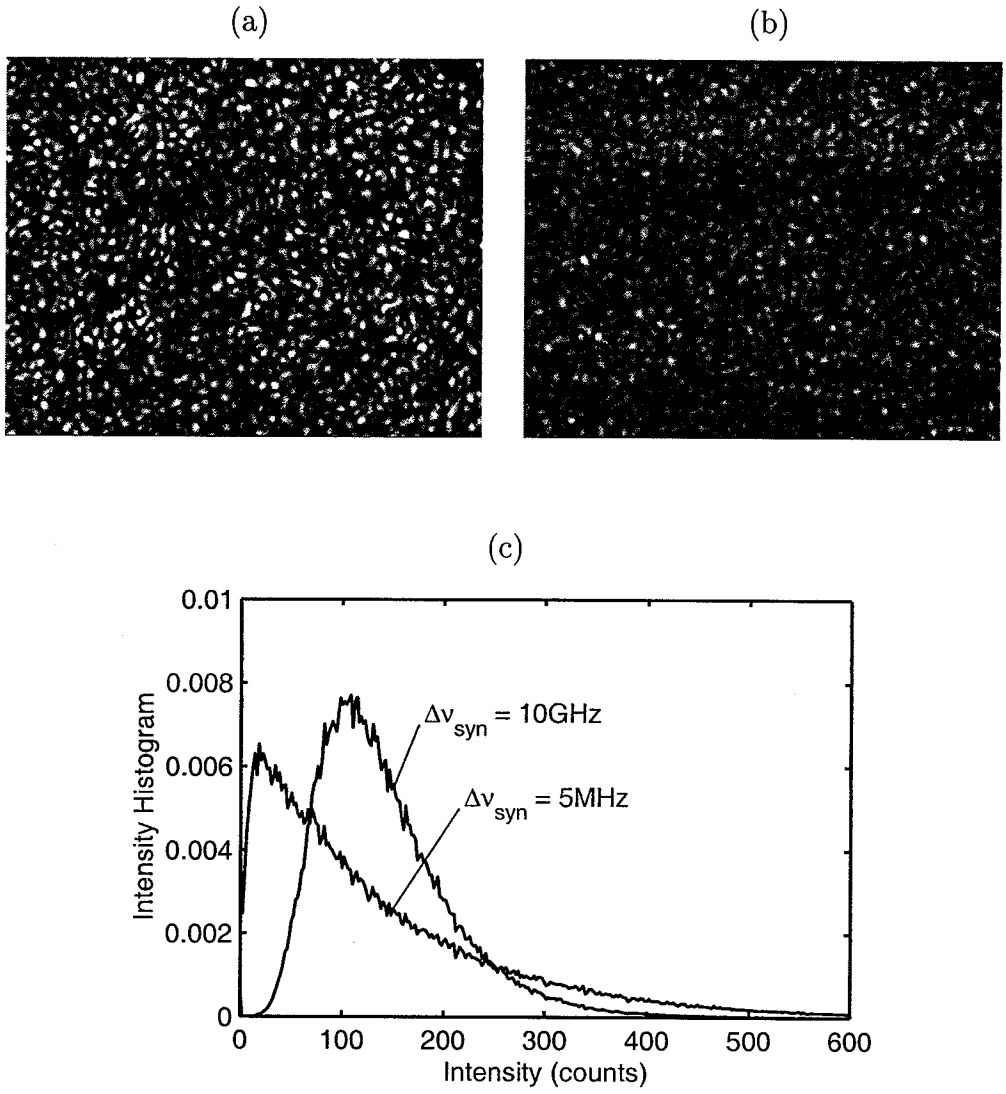

Fig. 4.11. The intensity speckle patterns for a 9 mm homogeneous slab with synthesized linewidths of (a) 5 MHz, (b) 10 GHz. Both speckle patterns have the same mean of 141 counts. (c) The intensity histograms of each speckle pattern. The measured contrast ratio for (a) $\Delta\nu_{\text{syn}} = 5\,\text{MHz}$ is $C_I = 0.95$ and for (b) $\Delta\nu_{\text{syn}} = 10\,\text{GHz}$ is $C_I = 0.47$.

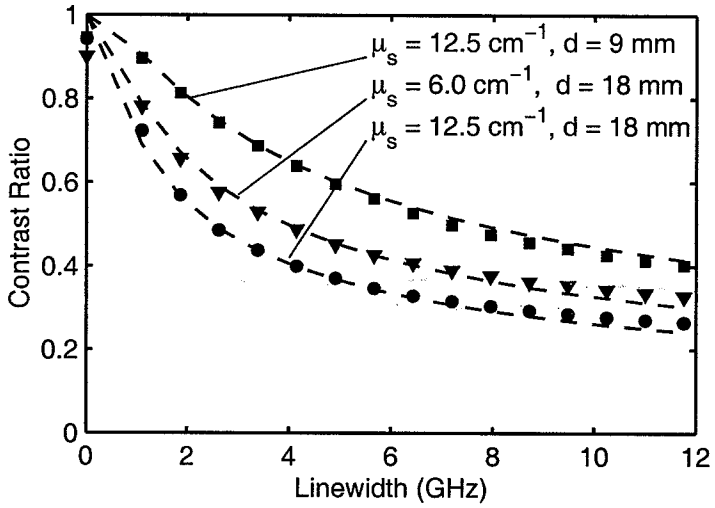

Fig. 4.12. Contrast ratio data as a function of synthesized linewidth for two different acrylic samples. The symbols are experimental data, and the dashed lines are theoretical fits, using a diffusion model for $p(t)$ in (2.54).

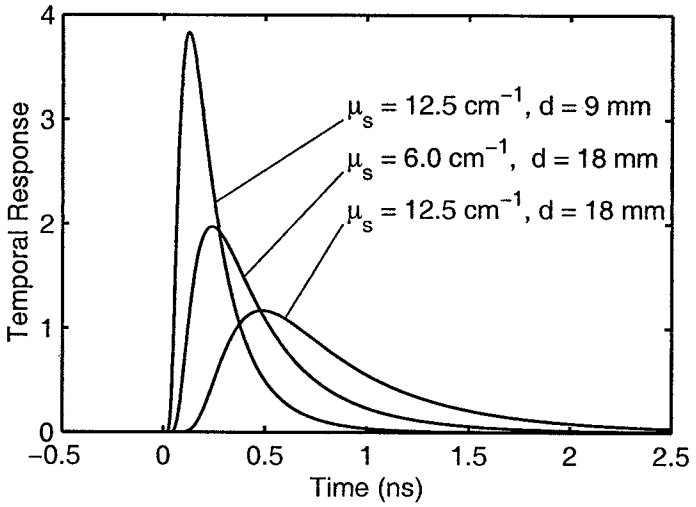

Fig. 4.13. Plots of the temporal responses calculated from a diffusion model with parameters used to model the data in Fig. 4.12.

tial. This is due to the spread in the time of flight distribution of the scattered partial waves being comparable to the synthesized coherence time $1/\Delta\nu_{\text{syn}}$ of the source.

The sensitivity of the speckle statistics to synthesized linewidth allows the scattering properties of a random medium to be estimated, based on a model such as the

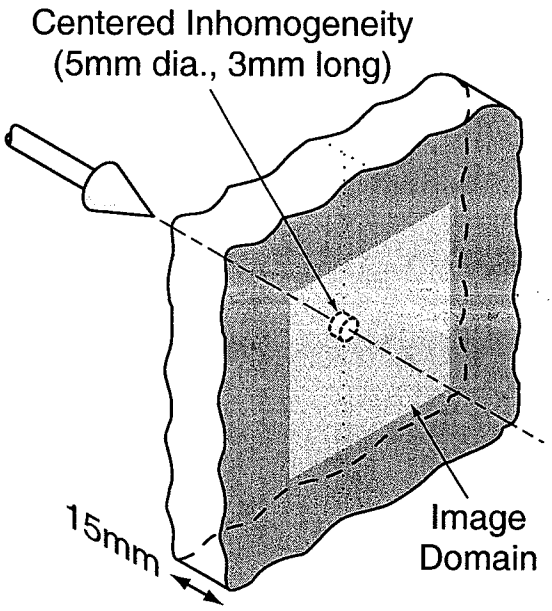

Fig. 4.14. Geometry of the sample used for the inhomogeneity localization experiments. The imaging domain is approximately 45 mm × 36 mm in size.

diffusion model for the time of flight distribution. The contrast ratio as a function of synthesized linewidth was measured for several different scattering slab samples, with the results shown in Fig. 4.12. For a fixed amount of scatter the contrast ratio decreases with decreasing coherence time (increasing $\Delta\nu_{\text{syn}}$), with an initially rapid decrease. This decrease in contrast ratio is also more rapid for greater amounts of scatter. The scattering coefficient for these samples was determined by fitting μ_s' in a diffusion model for the time of flight distribution $p(t)$ in the expression for the contrast ratio of (2.54). These results are shown as the dashed lines in Fig. 4.12. Plots of the corresponding temporal response as given in Fig. 4.13.

The speckle contrast ratio together with a variable linewidth source can also be used to visualize laterally localized inhomogeneities within optically scattering media. To demonstrate this, we fabricated the sample of Fig. 4.14, which consists of 5 sheets of the less scattering acrylic ($\mu_s' = 6\,\text{cm}^{-1}$), each 3 mm-thick, as the background. The central sheet had a 5 mm diameter hole milled through its center, to form or locate an inhomogeneity. The imaging optics were modified to the single lens configuration

shown in Fig. 2.5. The distances $z_1 = 200\,\text{mm}$ and $z_2 = 66\,\text{mm}$, with $f = 50\,\text{mm}$ were chosen such that an area of $45\,\text{mm} \times 36\,\text{mm}$ on the back face of the sample was imaged onto the CCD array, and the aperture at the lens was also adjusted to give a large number of sufficiently sized speckles in the speckle pattern.

Speckle patterns were obtained for three different inhomogeneities, namely a void region, a 5 mm diameter disk of heavily scattering acrylic, and a 5 mm diameter disk of weak absorber ("smoky" colored acrylic), and also for the case of a homogeneous sample, each for synthesized linewidths of 5 MHz and 17 GHz. The contrast ratio was calculated locally within a 150×150 pixel subregion, and this subregion was then scanned throughout the speckle pattern in 25 pixel increments to form a map of the contrast ratio within the speckle pattern domain. The contrast ratio map obtained from a homogeneous sample of the background material for each synthesized linewidth was then subtracted, leaving the contrast ratio difference images shown in Fig. 4.15. In these images, red represents a higher contrast ratio than the homogeneous case, and blue represents a lower contrast ratio. In Fig. 4.15(b) we see a higher contrast ratio for the void inhomogeneity localized in the center of the image, which is consistent with the expectation that less scatter results in a higher contrast ratio. Conversely, in Fig. 4.15(d), for the heavily scattering acrylic inhomogeneity, there is a lower contrast ratio localized in the center of the image, which is consistent with the expectation that more scatter results in a lower contrast ratio. Also, interestingly, in Fig. 4.15(f), the contrast ratio for the weak absorber is also greater than the homogeneous background. This indicates that even though there is absorption present, the time of flight distribution is narrower due to the presence of less scatter. These data demonstrate the ability not only to identify an inhomogeneity, but also to determine whether it is more or less scattering than the background.

No localization of the inhomogeneity is apparent from the contrast ratio difference images of Figs. 4.15(a), (c), and (e) for the 5 MHz linewidth. This result can be explained by considering the data of Fig. 4.12, which shows that for such a narrow-linewidth, the contrast ratio is approximately unity, essentially independent of the

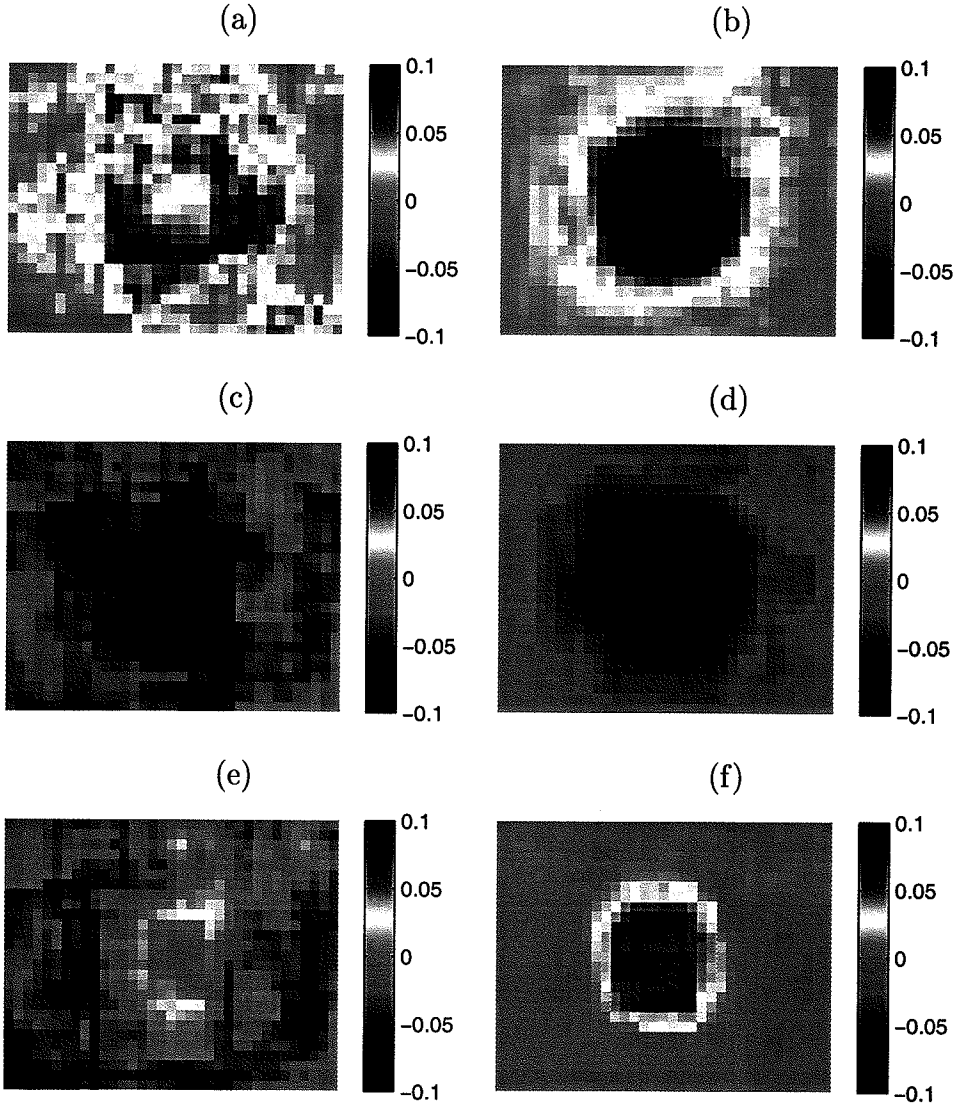

Fig. 4.15. (color) Contrast ratio difference images for three different inhomogeneities at two different synthesized linewidths: (a) void at 5 MHz, (b) void at 17 GHz, (c) heavy scatterer at 5 MHz, (d) heavy scatterer at 17 GHz, (e) absorber at 5 MHz, (f) absorber at 17 GHz. The difference in contrast ratio is shown by the color bars.

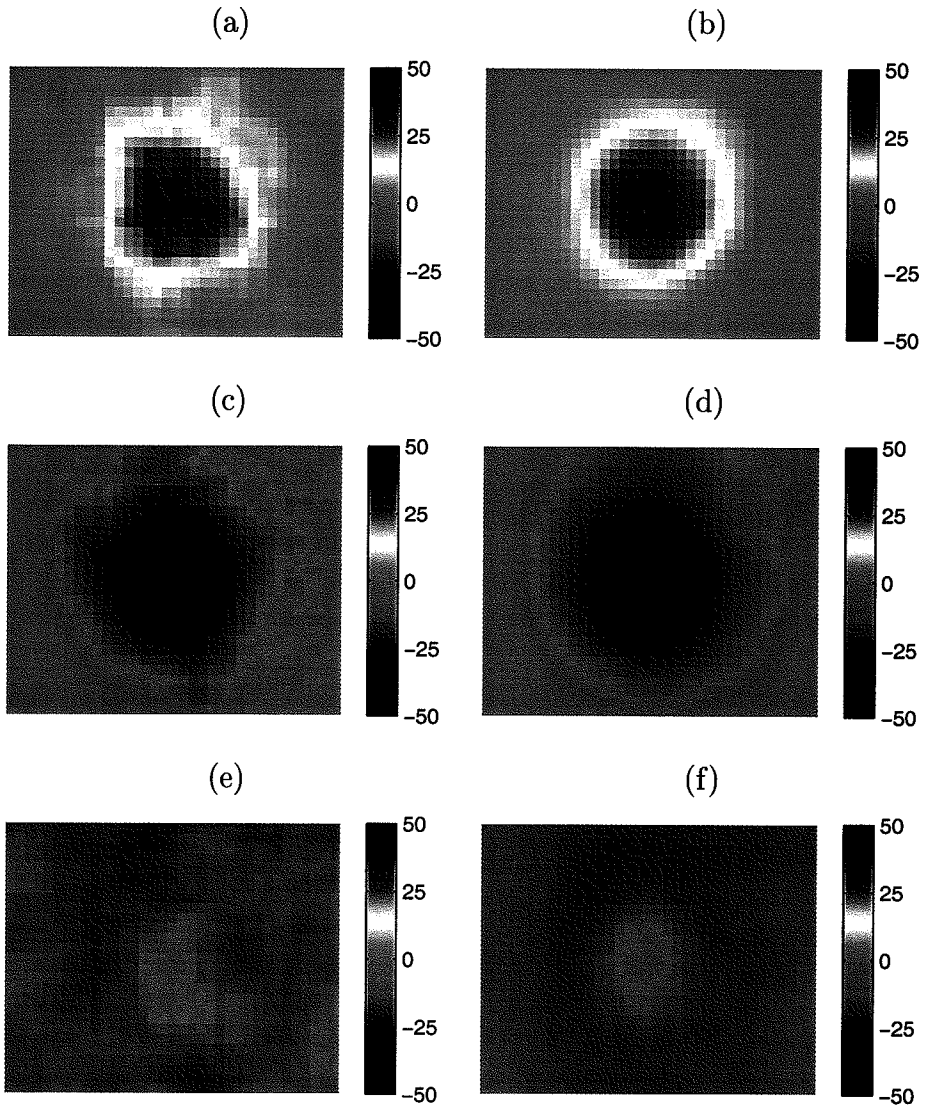

Fig. 4.16. (color) Mean difference images for three different inhomogeneities at two different synthesized linewidths: (a) void at 5 MHz, (b) void at 17 GHz, (c) heavy scatterer at 5 MHz, (d) heavy scatterer at 17 GHz, (e) absorber at 5 MHz, (f) absorber at 17 GHz. The difference in mean from a homogeneous sample is shown by the color bars.

amount of scatter in these samples. The 17 GHz linewidth used in Figs. 4.15(b), (d), and (f) is comparable to the inverse of the width of $p(t)$, for which there is much greater sensitivity of contrast ratio to linewidth and scatter variations. The ability to synthesize the desired linewidth is a very important factor in localizing inhomogeneities using contrast ratio difference images.

A difference map for the mean for each inhomogeneity at both synthesized linewidths was also formed in an identical manner. The results are shown in Fig. 4.16, where again red represents a higher mean than the homogeneous background and blue represents a lower mean. Here, the results are seen to be independent of the synthesized linewidth, which is expected, since the mean intensity is not a function of the coherence properties of the source, as seen in Fig. 4.11. However, the mean is a spatial function of the scattering properties of the inhomogeneous sample. It is interesting to observe that the difference in mean for the void region and heavy scattering inhomogeneity follow the same trend as the difference in contrast ratio, as seen by comparing Figs. 4.16(b) and (d) with Figs. 4.15(b) and (d). But for the weak absorber, the difference mean and contrast ratio follow the opposite trend. This highlights the result that the speckle statistics are sensitive to both the scattering properties a random medium and to the coherence properties of the source.

4.5 Summary

It was shown that the speckle correlation technique provides an accurate means for determining the temporal response of a random medium. The second-order and third-order intensity correlations enabled the reconstruction of the temporal response that showed excellent agreement with both a diffusion model and the intensity response measured directly using a short pulse laser and streak camera. In particular, the third-order intensity correlation technique allows the temporal response to be reconstructed without assuming a form or model for the temporal response. The speckle correlations

also demonstrated measurable sensitivity to an inhomogeneity within a scattering domain.

The coherence properties of the source were also demonstrated to affect the statistics of speckle patterns produced by a random medium. We synthesized the source coherence properties by scanning the center-frequency of a narrow-linewidth tunable laser diode. This enabled the scattering properties of a homogeneous slab to be estimated from the speckle contrast ratio, based upon a diffusion model fit. The speckle contrast ratio as a function of source coherence also demonstrated sensitivity to different types of inhomogeneous scattering domains, highlighting the potential of optical imaging in scattering media.

5. SPECKLE INTERFEROMETER PROPOSAL

5.1 Introduction

In this chapter, I present a proposal for using a speckle interferometer configuration to obtain the temporal response of a random medium. The technique closely parallels that of spectral interferometry used in ultrafast optics for characterizing the frequency response of linear optical elements [93].

There are advantages to using an interferometer configuration over the speckle intensity correlation technique. Firstly, as will be shown, an interferometer allows the complex field amplitude from a random medium to be measured. The reference path, after being calibrated, eliminates the arbitrary time-offset present in the intensity correlation techniques currently used to reconstruct the temporal response $p(t)$. This result is achieved by allowing the field correlation expression of (2.37) to be evaluated directly. Secondly, an increase in the magnitude of the frequency-dependent fluctuating intensity is expected, because this term is the product of a strong reference field amplitude and a weak field from the random medium, rather than the weak field squared that is the measured fluctuating intensity obtained without a reference field.

Recently, Tualle [94] reported a technique for performing time-resolved measurements in random media that is similar to the proposed technique. However, it is believed that the method proposed here is far simpler, since it does not involve the unnecessary mathematical complexity of Tualle's technique. The key observation of this proposed technique is in identifying what an interferometer configuration actually measures from a random medium, and then being able extracting the desired information from these measurements.

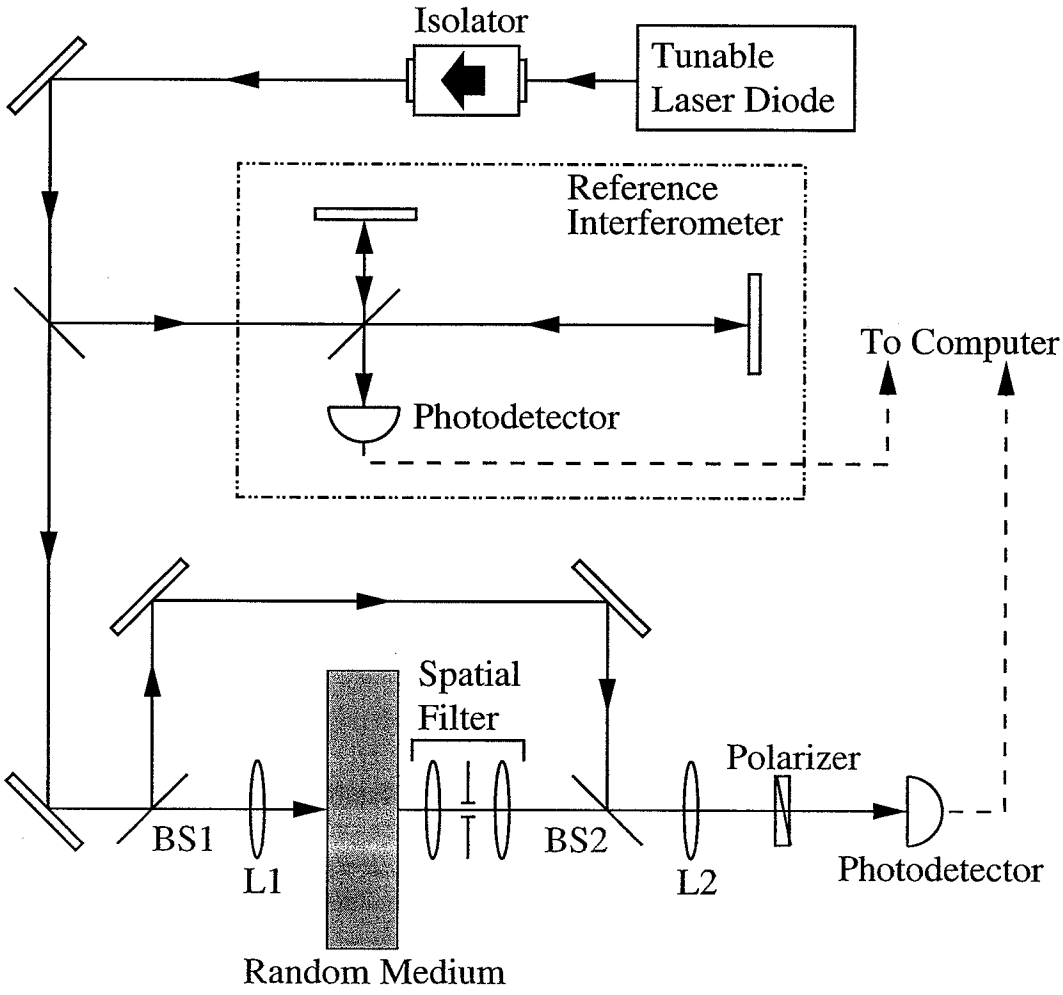

Fig. 5.1. The proposed interferometer experimental configuration. The random medium and speckle forming optics are in one arm of a Mach-Zehnder interferometer configuration. The reference interferometer is used to monitor the laser frequency scan by counting fringes.

5.2 Experimental Configuration

A schematic of the proposed interferometer experimental configuration is shown in Figure 5.1. The random medium and speckle forming optics, the same as in Fig. 3.1, are one arm of a Mach-Zehnder interferometer. The other arm, of a known path length difference, forms the reference arm. In Fig. 3.1, a Fabry-Perot interferometer was used to monitor the change in laser diode frequency, which is replaced by a simple

fixed interferometer (drawn here in the Michelson configuration), to count fringes as the laser frequency is scanned.

Here it is proposed that a photodetector is used to measure the intensity of a single speckle spot. The ensemble statistics are then formed by either moving the sample slightly, or by moving the detector. It is, of course, possible to use a CCD camera here and form the ensemble statistics from the speckle image, as it is currently done. There may be practical issues limiting the use of a CCD camera, such as the acquisition time of the camera relative to the stability of the interferometer. Also, a large number of images will need to be taken at small frequency increments in order to resolve the intensity fluctuations in the interferometer output as the laser frequency is scanned.

5.3 Theory

A reference signal, $e_{\text{ref}}(t)$, and input signal to the random medium, $e_{\text{in}}(t)$, are produced from the output of the narrow-linewidth tunable laser by beam-splitter $BS1$, assumed to have a 50/50 splitting ratio (all the beam-splitters in this analysis are assumed 50/50 to simplify the mathematics, however an arbitrary splitting ratio can also be used). The input signal passes through the random medium under investigation, while the reference signal travels along the reference path. The reference path has a time-delay of τ relative to the signal path. These signals are represented by complex exponentials with an optical frequency of ν, and expressed as

$$e_{\text{in}}(t) = E_i \exp(j2\pi\nu t) + \text{ c.c.}, \tag{5.1}$$

and

$$e_{\text{ref}}(t) = E_{\text{ref}} \exp[j2\pi\nu(t-\tau)] + \text{ c.c.} \tag{5.2}$$

The complex amplitudes of E_{in} and E_{ref} are assumed to be independent of frequency. The observation time-reference of $t = 0$ is defined to be located at the second beam-

splitter, $BS2$, of Fig. 5.1. The output of the random medium, given by (2.23) and repeated here, is

$$e_{\text{out}}(t) = E_o(\nu)\exp(j2\pi\nu t) + \text{ c.c.} \tag{5.3}$$

The complex amplitude of the output signal, $E_o(\nu)$, is a function of the optical frequency, and is the random variable quantity of interest. The detected signal $e_{\text{det}}(t)$ is produced by combining the reference signal $e_{\text{ref}}(t)$ with the output signal from the random medium $e_{\text{out}}(t)$, via the beam-splitter $BS2$, giving

$$e_{\text{det}}(t) = \frac{1}{\sqrt{2}}e_{\text{ref}}(t) + \frac{1}{\sqrt{2}}e_o(t). \tag{5.4}$$

Upon substituting the expressions of (5.2) and (5.3) for $e_{\text{ref}}(t)$ and $e_{\text{out}}(t)$, respectively, into (5.4), the detected field is

$$e_{\text{det}}(t) = \frac{1}{\sqrt{2}}\left[E_o(\nu) + E_{\text{ref}}\exp(-j2\pi\nu\tau)\right]\exp(j2\pi\nu t) + \text{ c.c.} \tag{5.5}$$

The photodetector produces a signal proportional to the detected intensity, hence the measured signal from the interferometer, as a function of the optical frequency ν, is given by

$$I_{\text{det}}(\nu) = \frac{1}{2}\left[|E_o(\nu)|^2 + E_o(\nu)E_{\text{ref}}^*\exp(j2\pi\nu\tau) + E_o^*(\nu)E_{\text{ref}}\exp(-j2\pi\nu\tau) + |E_{\text{ref}}|^2\right]. \tag{5.6}$$

From this we see that the interferometer response has several components: a term proportional to the output intensity of the random medium $|E_o(\nu)|^2$, a term proportional to the reference signal intensity $|E_{\text{ref}}|^2$, a cross-product term of $E_o(\nu)E_{\text{ref}}^*\exp(j2\pi\nu\tau)$ with a τ-dependent spectral phase, and the conjugate of this cross-product term. It is the cross-product term that yields $E_o(\nu)$ from an interferometer configuration.

Consider the inverse Fourier transform of a function $F(\nu)$ defined by

$$f(t) = \int_{-\infty}^{\infty} \mathrm{d}\nu\ F(\nu)\exp(j2\pi\nu t). \tag{5.7}$$

Taking the inverse Fourier transform of $I_{\text{det}}(\nu)$ of (5.6) using the relation of (5.7), we obtain an expression consisting again of several terms in the form of

$$i_{\text{det}}(t) = \frac{1}{2}\left[g(t) + e(t+\tau) + e^*(-t+\tau)\right]. \tag{5.8}$$

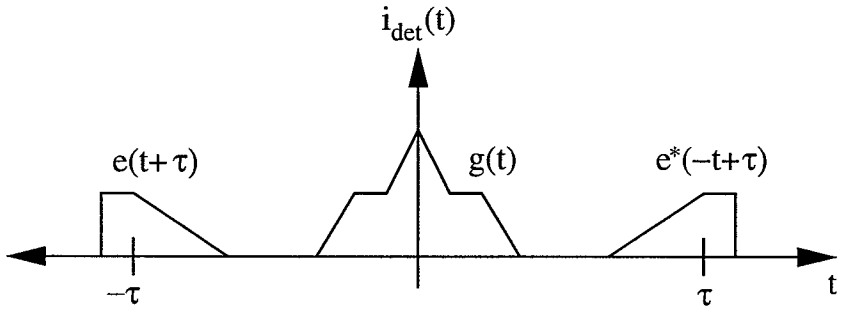

Fig. 5.2. A sketch showing the features obtained from inverse Fourier Transforming the measured interferometer data.

The terms in (5.8) are given by

$$g(t) = \int_{-\infty}^{\infty} \mathrm{d}\nu \; |E_o(\nu)|^2 \exp(j2\pi\nu t) + |E_{\mathrm{ref}}|^2 \delta(t), \tag{5.9}$$

and

$$e(t) = E_{\mathrm{ref}}^* \int_{-\infty}^{\infty} \mathrm{d}\nu \; E_o(\nu) \exp(j2\pi\nu t). \tag{5.10}$$

The function $i_{\mathrm{det}}(t)$ can be seen to consist of three main features: the function $g(t)$ centered at $t = 0$, the function $e(t)$ centered at $t = -\tau$, and its time-reversed conjugate centered at $t = \tau$. Assuming that the duration of $g(t)$ and $e(t)$ are limited such that a value of τ can be chosen large enough so that the features do not overlap, we will obtain a representation for $i_{\mathrm{det}}(t)$ in the form of the plot shown in Figure 5.2. This result is identical in form to the result obtained by inverse Fourier transforming data measured using spectral interferometry in ultrafast optics.

To obtain our desired function of $E_o(\nu)$, we can simply take the temporal data of $i_{\mathrm{det}}(t)$ and set the result to zero, except for a finite window centered at $t = -\tau$ that captures the features of $e(t+\tau)$. Next, we can shift this data by τ to the origin, and then take a Fourier transform, which gives

$$E_o(\nu) = (E_{\mathrm{ref}}^*)^{-1} \int_{-\infty}^{\infty} \mathrm{d}\nu \; e(t) \exp(-j2\pi\nu t). \tag{5.11}$$

Thus, by scanning the laser frequency and measuring the interferometer output as a function of scan frequency, then Fourier transforming the data as described above, we obtain the desired field of $E_o(\nu)$ (scaled by the constant E_{ref}^*).

Having obtained an expression for $E_o(\nu)$, the temporal response of the random medium can be obtained by using the field correlation expression of (2.37), repeated here,

$$\langle E_o(\nu + \Delta\nu) E_o^*(\nu) \rangle = \langle I \rangle P(\Delta\nu), \tag{5.12}$$

where $\langle I \rangle$ is the mean intensity from the random medium (taken as a constant), and $P(\Delta\nu)$ is the Fourier transform of the temporal response given by

$$P(\Delta\nu) = \int_{-\infty}^{\infty} \mathrm{d}t \; p(t) \exp(-j2\pi\Delta\nu t). \tag{5.13}$$

The ensemble statistics can be formed by moving the sample or photodetector and repeating the measurement.

5.4 Numerical Simulations

In this section I shall briefly discuss some numerical simulations performed to model the data one would obtain from interferometer measurements of a random medium using the procedure outlined in the previous section.

The key aspect of these simulations is the requirement to generate a random field for $E_o(\nu)$ that has the desired statistical properties. It is usually simple, in MATLAB, for example, to generate an array zero-mean Gaussian random variables to represent the sampled complex field $E_o(\nu)$. However, the random variables in this array are all independent, and thus represent a delta-function correlated random field, often called white Gaussian random noise. It is required that $E_o(\nu)$ have a finite frequency correlation range and form given by (5.12). This can be obtained by adapting a "moving average" technique on the array of uncorrelated data [95, 96]. Here, each point in the array of correlated data is generated by a weighted sum of the values from the uncorrelated array, using a suitably chosen weighting function. This can also be conveniently viewed as a convolution operation.

Consider a zero-mean complex white Gaussian random noise process as a function of frequency $Z(\nu) = Z_r(\nu) + jZ_i(\nu)$, whose correlation is given by

$$\langle Z(\nu + \Delta\nu) Z^*(\nu) \rangle = \delta(\Delta\nu). \tag{5.14}$$

The function $Z(\nu)$ is convolved with a weighting function $W(\nu)$ to form the zero-mean complex random process representing the complex field amplitude

$$E_o(\nu) = \int_{-\infty}^{\infty} \mathrm{d}\nu' \; W(\nu - \nu') Z(\nu'). \tag{5.15}$$

After some algebra utilizing (5.14), it can be shown that the field correlation function is given by

$$\langle E_o(\nu + \Delta\nu) E_o^*(\nu) \rangle = \int_{-\infty}^{\infty} \mathrm{d}\nu' \; W(\nu' + \Delta\nu) W^*(\nu'). \tag{5.16}$$

Thus, what remains is to choose a suitable weighting function $W(\nu)$ that gives the field correlation function of (5.12). Representing $W(\nu)$ as the Fourier transform of the function $w(t)$,

$$W(\nu) = \int_{-\infty}^{\infty} \mathrm{d}t \; w(t) \exp(-j2\pi\nu t), \tag{5.17}$$

and then substituting (5.17) into (5.16), gives the final result of

$$\langle E_o(\nu + \Delta\nu) E_o^*(\nu) \rangle = \int_{-\infty}^{\infty} \mathrm{d}t \; |w(t)|^2 \exp(-j2\pi\Delta\nu t). \tag{5.18}$$

To obtain the desired result, we simply chose the weighting function

$$|w(t)| = \sqrt{p(t)} \tag{5.19}$$

The phase of the weighting function is unimportant in this example. Also, recall that $p(t)$ is a real positive quantity.

To demonstrate the results of this technique, a weighting function was chosen using the diffusion equation model for the temporal response of a random medium with thickness $d = 12\,\mathrm{mm}$ and a scattering coefficient of $\mu_s' = 13\,\mathrm{cm}^{-1}$. The real part of a sample $Z(\nu)$ white noise process is shown in Fig. 5.3(a). It can be seen that the spectral features in this plot are very small. Using (5.15), the simulated random medium output complex field amplitude was calculated, with the real part of a sample function shown in Fig. 5.3(b) (the imaginary part is similar). The key observation is that the spectral feature size in this plot is now much broader, and on the order of 1–2 GHz. These observations are also supported by the correlation functions plotted in Fig. 5.3(c) for $\langle Z(\nu+\Delta\nu) Z^*(\nu) \rangle$, and in Fig. 5.3(d) for $\langle E_o(\nu+\Delta\nu) E_o^*(\nu) \rangle$, calculated

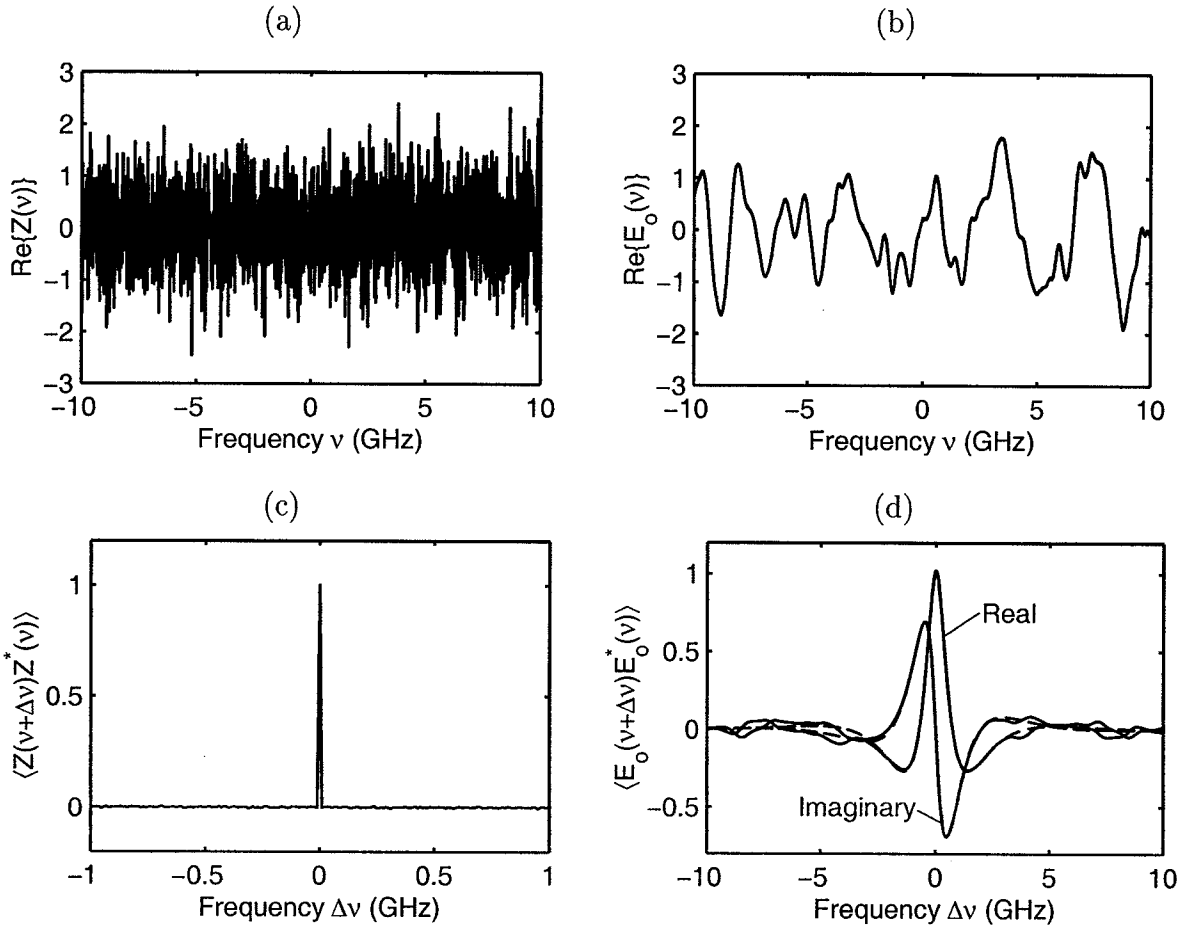

Fig. 5.3. (a) The real part of the delta-correlated noise $Z(\nu)$. (b) The real part of the simulated random medium output field $E_o(\nu)$. (c) The correlation of $\langle Z(\nu+\Delta\nu)Z^*(\nu)\rangle$ evaluated using 100 samples. (d) The random field correlation of $\langle E_o(\nu+\Delta\nu)E_o^*(\nu)\rangle$ evaluated using 100 samples (solid lines). The desired real and imaginary components of $P(\Delta\nu)$ (dashed lines).

by using 100 samples to form the ensemble statistics. In Fig. 5.3(d), there is very good agreement with the desired correlation function of (5.12).

The numerically generated random medium complex field amplitude $E_o(\nu)$, as a function of frequency, was used to simulate the response of the interferometer with two values for the reference arm delay of $\tau = 4\,\text{ns}$ and $\tau = 2\,\text{ns}$. The interferometer output intensity $I_{\text{det}}(\nu)$ for each delay was calculated using (5.6), and these results are plotted in Fig. 5.4. These plots were generated using $\langle|E(\nu)|^2\rangle = 1$ and $|E_{\text{ref}}|^2 = 1$.

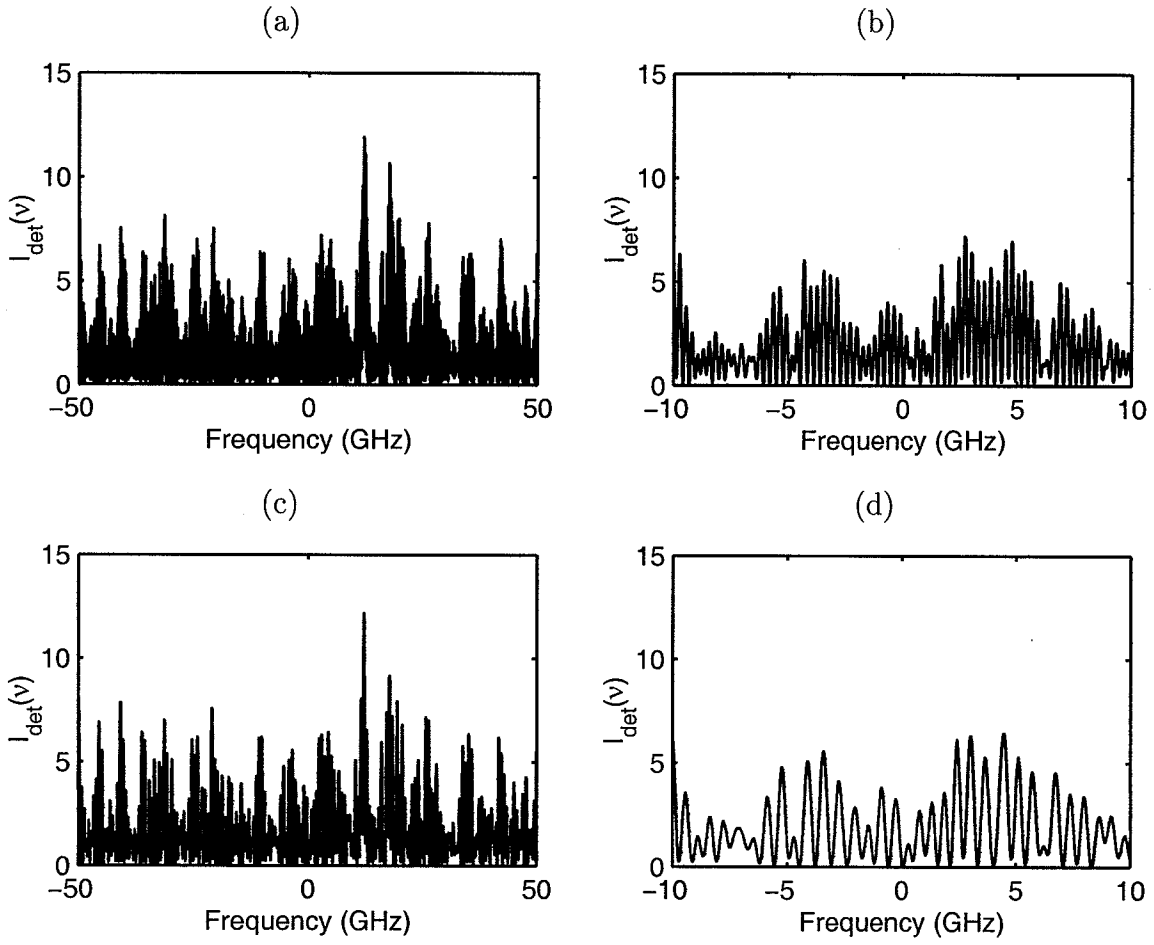

Fig. 5.4. (a) Simulated interferometer output intensity for $\tau = 4\,\text{ns}$. (b) As in (a), but with a change in frequency scale. (c) Simulated interferometer output intensity for $\tau = 2\,\text{ns}$. (d) As in (c), but with a change in frequency scale.

In practice, $|E_{\text{ref}}|^2 \gg \langle |E(\nu)|^2 \rangle$. Comparing Figs. 5.4(b) and (d), for the cases of $\tau = 4\,\text{ns}$ and $\tau = 2\,\text{ns}$ respectively, we see that the fluctuations in $I_{\text{det}}(\nu)$ are more rapid for the larger reference arm delay than for the smaller reference arm delay. This is expected from (5.6), since for a larger delay time, smaller changes in frequency are required to cause a 2π phase change.

An inverse Fourier transform of the numerical data in Fig. 5.4 was taken to obtain the function $i_{\text{det}}(t)$ of (5.8). The results for a typical sample for both values of reference arm delay, $\tau = 4\,\text{ns}$ and $\tau = 2\,\text{ns}$ are plotted in Fig. 5.5. The features indicated in

(a)

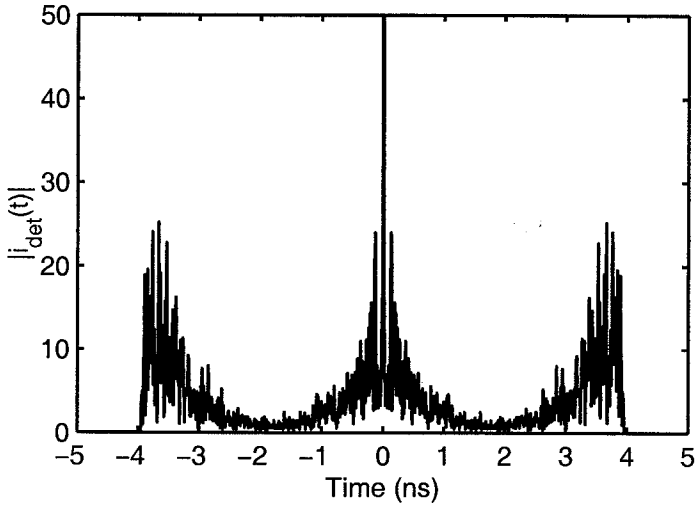

(b)

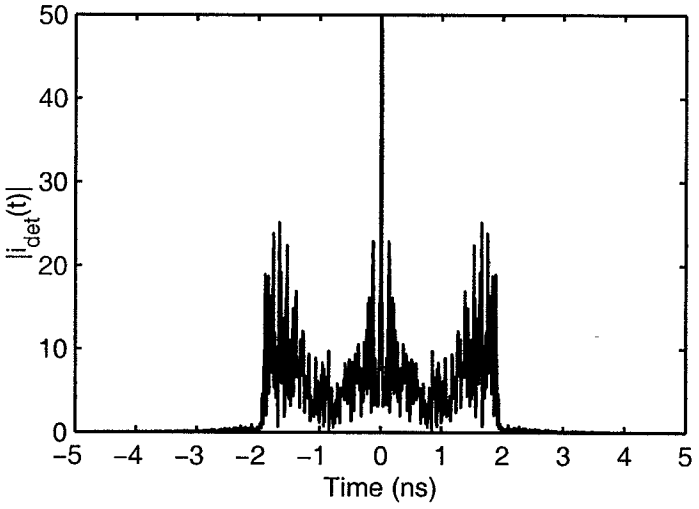

Fig. 5.5. (a) The magnitude of $i_{\mathrm{det}}(t)$ calculated by inverse Fourier transforming the data of Fig. 5.4(a), for $\tau = 4\,\mathrm{ns}$. (b) The magnitude of $i_{\mathrm{det}}(t)$ calculated by inverse Fourier transforming the data of Fig. 5.4(c), for $\tau = 2\,\mathrm{ns}$.

Fig. 5.2 can be readily seen in these plots. For the $\tau = 2\,\mathrm{ns}$ case, shown in Fig. 5.5(b), the features are not well separated, and some aliasing in the reconstructed temporal response can be expected. However, in Fig. 5.5(a), the features are well separated.

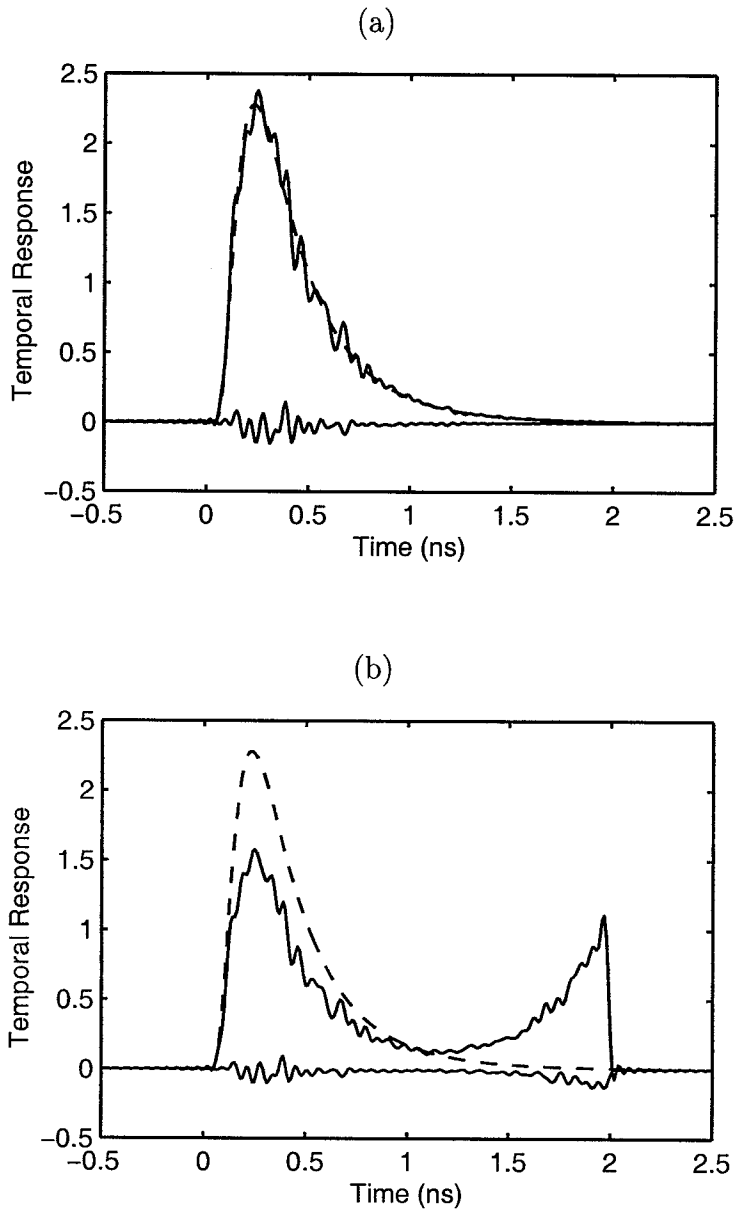

Fig. 5.6. (a) The reconstructed temporal response simulated using an interferometer with $\tau = 4\,\text{ns}$. (b) The reconstructed temporal response simulated using an interferometer with $\tau = 2\,\text{ns}$. The small imaginary component for each result is also shown. The analytic temporal response is shown in both plots (dashed lines).

The field correlation of (5.12) was calculated using the simulated data presented in Fig. 5.5 for 100 sample realizations, to estimate the ensemble statistics. An inverse Fourier transform of the correlation in (5.12) was then used to estimate the temporal

response, with the results plotted in Fig. 5.6. Ideally, the field correlation of (5.12) should be Hermitian, so the inverse Fourier transform should be purely real. However, due to the errors in statistical sampling using 100 samples, the field correlation is not truly Hermitian, which results in the small imaginary component seen in the reconstructed temporal responses. (The correlation data could have been forced to be Hermitian by only calculating it for positive frequencies, then using symmetry to get the data for negative frequencies, but this was not done.)

The effect of the aliasing noted in Fig. 5.5(b) for the case of $\tau = 2\,\text{ns}$ is clearly seen in Fig. 5.6(b). This raises the trade-off issue of choosing a suitable value for the reference arm delay of τ. If the delay is too small for the width of the expected temporal response, then the aliasing phenomenon will occur. However, making the delay large causes the detected intensity fluctuations to vary more rapidly with the frequency scan, which requires finer sampling increments. This will make the experimental implementation more challenging.

5.5 Summary

A proposal has been outlined for using an interferometer configuration to obtaining the temporal response of a random medium. Numerical simulations were performed to verify the operation of the interferometer, highlighting the important design parameters. The interferometer technique allows the complex amplitude of the electric field as a function of frequency from a random medium to be obtained directly. Hence, the temporal response can be evaluated without the arbitrary time-offset obtained when using purely intensity correlations.

6. CONCLUSIONS

The scattering properties of a random medium have been investigated using speckle intensity frequency correlation techniques. A narrow-linewidth external cavity tunable laser diode was used as the source for these experiments. The first-time demonstration of reconstructing the temporal response from a random medium using third-order intensity frequency correlations was presented. The third-order correlation technique measures the temporal response up to a arbitrary time offset, but does not require any *a priori* knowledge about the form of the temporal response, only that the speckle field be described by circular complex Gaussian statistics. The measured results were in excellent agreement with those obtained using a short pulse ultrafast laser and a streak camera. The scattering properties of the random medium samples used in this study were accurately modeled by the diffusion approximation to the photon transport equation.

It was also demonstrated that a source with a variable power spectral density could be synthesized using an external cavity tunable laser diode. This enabled the coherence properties of the source to be varied, allowing the change in speckle statistics as a function of synthesized coherence be used to characterize a scattering medium. It was found that the speckle contrast ratio as a function of synthesized linewidth provides a good measure for determining the scattering properties of a homogeneous random medium in the diffusion regime.

The speckle intensity correlations and also the measured speckle contrast ratio as a function of synthesized linewidth were shown to be sensitive to inhomogeneities within the scattering domain. Therefore, speckle techniques show potential as a new and interesting experimental modality to obtain imaging data for scattering random media.

LIST OF REFERENCES

LIST OF REFERENCES

[1] A. Ishimaru, *Wave Propagation and Scattering in Random Media.* New York: Academic Press, 1978.

[2] A. Ishimaru, "Wave propagation and scattering in random media and rough surfaces," *Proc. IEEE*, vol. 79, pp. 1359–1366, October 1991.

[3] V. V. Tuchin, *Tissue Optics: Light Scattering Methods and Instruments for Medical Diagnosis*, vol. TT38 of *Tutorial Texts in Optical Engineering.* Bellingham: SPIE Press, 2000.

[4] J. C. Hebden, S. R. Arridge, and D. T. Delpy, "Optical imaging in medicine: I. Experimental techniques," *Phys. Med. Biol.*, vol. 42, pp. 825–840, 1997.

[5] P. P. Ho, P. Baldeck, K. S. Wong, K. M. Yoo, D. Lee, and R. R. Alfano, "Time dynamics of photon migration in semiopaque random media," *Appl. Opt.*, vol. 28, pp. 2304–2310, June 1989.

[6] K. M. Yoo and R. R. Alfano, "Time-resolved coherent and incoherent components of forward light scattering in random media," *Opt. Lett.*, vol. 15, pp. 320–322, March 1990.

[7] L. Wang, P. P. ho, C. Liu, G. Zhang, and R. R. Alfano, "Ballistic 2-D imaging through scattering walls using an ultrafast optical Kerr gate," *Science*, vol. 253, pp. 769–771, August 1991.

[8] K. M. Yoo, Q. Xing, and R. R. Alfano, "Imaging objects hidden in highly scattering media using femtosecond second-harmonic-generation cross-correlation time gating," *Opt. Lett.*, vol. 16, pp. 1019–1021, July 1991.

[9] E. Leith, C. Chen, H. Chen, Y. Chen, D. Dilworth, J. Lopez, J. Rudd, P. C. Sun, J. Valdmanis, and G. Vossler, "Imaging through scattering media with holography," *J. Opt. Soc. Am. A*, vol. 9, pp. 1148–1153, July 1992.

[10] D. Huang, E. A. Swanson, C. P. Lin, J. S. Schuman, W. G. Stinson, W. Chang, M. R. Hee, T. Flotte, K. Gregory, C. A. Puliafito, and J. G. Fujimoto, "Optical coherence tomography," *Science*, vol. 254, pp. 1178–1181, November 1991.

[11] J. M. Schmitt, "Optical coherence tomograhy (OCT): A review," *IEEE J. Sel. Topics Quantum Electron.*, vol. 5, pp. 1205–1215, July 1999.

[12] J. G. Fujimoto, W. Drexler, U. Morgner, F. Kartner, and E. Ippen, "Optical coherence tomography: high resolution imaging using echoes of light," *Optics and Photonics News*, vol. 11, pp. 24–31, January 2000.

[13] J. C. Hebden, R. A. Kruger, and K. S. Wong, "Time resolved imaging through a highly scattering medium," *Appl. Opt.*, vol. 30, pp. 788–794, March 1991.

[14] J. C. Hebden and D. T. Delpy, "Enhanced time-resolved imaging with a diffusion model of photon transport," *Opt. Lett.*, vol. 19, pp. 313–313, March 1994.

[15] R. Cubeddu, A. Pifferi, P. Taroni, A. Torricelli, and G. Valentini, "Time-resolved imaging on a realistic tissue phantom: μ_s' and μ_a images versus time-integrated images," *Appl. Opt.*, vol. 35, pp. 4533–4540, August 1996.

[16] S. J. Madsen, E. R. Anderson, R. C. Haskell, and B. J. Tromberg, "Portable, high-bandwidth frequency-domain photon migration instrument for tissue spectroscopy," *Opt. Lett.*, vol. 19, pp. 1934–1936, December 1994.

[17] J. B. Fishkin, S. Fantini, M. J. van de Ven, and E. Gratton, "Gigahertz photon density waves in a turbid medium: theory and experiments," *Phys. Rev. E*, vol. 53, pp. 2307–2319, March 1996.

[18] M. A. O'Leary, D. A. Boas, and A. G. Yodh, "Experimental images of heterogeneous turbid media by frequency-domain diffusing-photon tomography," *Optics Lett.*, vol. 20, pp. 426–428, March 1995.

[19] J. S. Reynolds, A. Przadka, S. P. Yeung, and K. J. webb, "Optical diffusion imaging: a comparative numerical and experimental study," *Appl. Opt.*, vol. 35, pp. 3671–3679, July 1996.

[20] B. J. Tromberg, L. O. Svaasand, T. T. Tsay, and R. C. Haskell, "Properties of photon density waves in multiple-scattering media," *Appl. Opt.*, vol. 32, pp. 607–616, February 1996.

[21] S. R. Arridge, "Optical tomography in medical imaging," *Inverse Problems*, vol. 15, pp. R41–R93, 1999.

[22] J. C. Ye, K. J. Webb, C. A. Bouman, and R. P. Millane, "Optical diffusion tomography using iterative coordinate descent optimization in a Bayesian framework," *J. Opt. Soc. Am. A*, vol. 10, pp. 2400–2412, October 1999.

[23] Y. Yao, Y. Wang, Y. Pei, W. Zhu, and R. L. Barbour, "Frequency-domain optical imaging of absorption and scattering distributions by a Born iterative method," *J. Opt. Soc. Am. A*, vol. 14, pp. 325–342, January 1997.

[24] A. B. Milstein, S. Oh, J. S. Reynolds, K. J. Webb, C. A. Bouman, and R. P. Millane, "Three-dimensional Bayesian optical diffusion tomography with experimental data"," *Opt. Lett.*, vol. 27, pp. 95–97, January 2002.

[25] J. C. Dainty, ed., *Laser Speckle and Related Phenomena.* Berlin: Springer-Verlag, second ed., 1984.

[26] H. H. Arsenault, "Roughness determination with laser speckle," *J. Opt. Soc. Am.*, vol. 61, pp. 1425–1426, October 1971.

[27] H. M. Pedersen, "Theory of speckle dependence on surface roughness," *J. Opt. Soc. Am.*, vol. 66, pp. 1204–1210, November 1976.

[28] H. Fujii, T. Asakura, and Y. Shindo, "Measurement of surface roughness properties by using image speckle contrast," *J. Opt. Soc. Am.*, vol. 66, pp. 1217–1222, November 1976.

[29] H. M. Pedersen, "On the contrast of polychromatic speckle patterns and its dependence on surface roughness," *Opt. Acta*, vol. 22, no. 1, pp. 15–24, 1975.

[30] G. Parry, "Some effects of temporal coherence on the first order statistics of speckle," *Opt. Acta*, vol. 21, no. 10, pp. 763–772, 1974.

[31] A. Labeyrie, "Attainment of diffraction limited resolution in large telescopes by Fourier analysing speckle patterns in star images," *Astron. Astrophys.*, vol. 6, no. 1, pp. 85–87, 1970.

[32] J. A. Leendertz, "Interferometric displacement measurement on scattering surfaces utilizing speckle effect," *J. Phys. E: Sci. Instrum.*, vol. 3, pp. 214–218, March 1970.

[33] K. Creath, "Phase-shifting speckle interferometry," *Appl. Opt.*, vol. 24, pp. 3053–3058, September 1985.

[34] A. F. Doval, "A systematic approach to TV holography," *Meas. Sci. Technol.*, vol. 11, pp. R1–R36, 2000.

[35] P. Sheng, ed., *Scattering and Localization of Classical Waves in Random Media.* Singapore: World Scientific, 1990.

[36] S. Feng and P. A. Lee, "Mesoscopic conductors and correlations in laser speckle patterns," *Science*, vol. 251, pp. 633–639, February 1991.

[37] J. H. Li and A. Z. Genack, "Correlation in laser speckle," *Phys. Rev. E*, vol. 49, pp. 4530–4533, May 1994.

[38] R. Berkovits and S. Feng, "Correlations in coherent multiple scattering," *Phys. Rep.*, vol. 238, no. 3, pp. 135–172, 1994.

[39] M. C. W. van Rossum and T. M. Nieuwenhuizen, "Multiple scattering of classical waves: microscopy, mesoscopy, and diffusion," *Rev. Mod. Phys.*, vol. 71, pp. 313–371, January 1999.

[40] S. Feng, C. Kane, P. A. Lee, and A. D. Stone, "Correlations and fluctuations of coherent wave transmissions through disordered media," *Phys. Rev. Lett.*, vol. 61, pp. 834–837, August 1988.

[41] M. A. Webster, K. J. Webb, and A. M. Weiner, "Temporal response of a random medium from third-order laser speckle frequency correlations," *Phys. Rev. Lett.*, vol. 88, p. 033901, January 2002.

[42] H. Gamo, "Phase determination of coherence functions by the intensity interferometer," in *Electromagnetic Theory and Antennas* (E. C. Jordan, ed.), vol. 6 of *International Series of Monographs on Electromagnetic Wave*, New York: Pergamon Press, 1963.

[43] H. Gamo, "Triple correlator of photoelectric fluctuations as a spectroscopic tool," *J. Appl. Phys.*, vol. 34, pp. 875–876, April 1963.

[44] R. Hanbury Brown and R. Q. Twiss, "A new type of interferometer for use in radio astronomy," *Phil. Mag.*, vol. 45, pp. 663–682, July 1954.

[45] A. W. Lohmann, G. Weigelt, and B. Wirnitzer, "Speckle masking in astronomy: triple correlation theory and applications," *Appl. Opt.*, vol. 22, pp. 4028–4037, December 1983.

[46] E. I. Blount and J. R. Klauder, "Recovery of laser intensity from correlation data," *J. Appl. Phys.*, vol. 40, p. 2874, June 1969.

[47] J. W. Goodman, "Statistical properties of laser speckle patterns," in *Laser Speckle and Related Phenomena* (J. C. Dainty, ed.), Berlin: Springer-Verlag, second ed., 1984.

[48] J. C. Dainty, "The statistics of speckle patterns," in *Progress in Optics* (E. Wolf, ed.), vol. XIV, Amsterdam: North-Holland, 1976.

[49] A. Papoulis, *Probability, Random Variables, and Stochastic Processes.* Boston: WCB/McGraw-Hill, third ed., 1991.

[50] E. Jakeman, "Speckle statistics with a small number of scatterers," *Opt. Eng.*, vol. 23, pp. 453–461, July 1984.

[51] W. T. Welford, "First order statistics of speckle produced by weak scattering media," *Opt. Quantum Electron.*, vol. 7, pp. 413–416, 1975.

[52] M. Nieto-Vesperinas and N. Garcia, "Non-circular Gaussian speckle contrast in the exact theory of multiple scattering of waves from random rough surfaces," *Opt. Commun.*, vol. 35, pp. 25–30, October 1980.

[53] J. W. Goodman, *Introduction to Fourier Optics.* New York: McGraw-Hill, 1996.

[54] M. Born and E. Wolf, *Principles of Optics.* Cambridge: Cambridge University Press, seventh ed., 1999.

[55] J. W. Goodman, "Dependence of image speckle constrast on surface roughness," *Opt. Commun.*, vol. 14, pp. 324–327, July 1975.

[56] B. Shapiro, "Large intensity flucuations for wave propagation in random media," *Phys. Rev. Lett.*, vol. 57, pp. 2168–2171, October 1986.

[57] W. T. Welford, "Speckle in images," *J. Opt. Soc. Am.*, vol. 66, pp. 1172–1174, November 1976.

[58] E. Jakeman and W. T. Welford, "Speckle statistics in imaging systems," *Opt. Commun.*, vol. 21, pp. 72–79, April 1977.

[59] S. Lowenthal and H. Arsenault, "Image formation for coherent diffuse objects: statistical properties," *J. Opt. Soc. Am.*, vol. 60, pp. 1478–1483, November 1970.

[60] N. George, "Speckle at various planes in an optical system," *Opt. Eng.*, vol. 25, pp. 754–764, June 1986.

[61] H. Fujii and T. Asakura, "Effect of the point spread function on the average contrast of image speckle patterns," *Opt. Commun.*, vol. 21, pp. 80–84, April 1977.

[62] N. Takai, H. Kadono, and T. Asakura, "Stastical properties of the speckle phase in image and diffraction fields," *Opt. Eng.*, vol. 25, pp. 627–635, May 1986.

[63] J. Uozumi and T. Asakura, "First-order intensity and phase statistics of Gaussian speckle produced in the diffraction field," *Appl. Opt.*, vol. 20, pp. 1454–1466, April 1981.

[64] D. S. Wiersma, P. Bartolini, A. Lagendijk, and R. Righini, "Localization of light in a disordered meidum," *Nature*, vol. 390, pp. 671–673, December 1997.

[65] I. S. Reed, "On a moment theorem for complex Gaussian processes," *IRE Trans. Inform. Theory*, vol. IT-8, pp. 194–195, April 1962.

[66] A. Z. Genack and J. M. Drake, "Relationship between optical intensity, fluctuations and pulse propagation in random media," *Europhys. Lett.*, vol. 11, pp. 331–336, February 1990.

[67] A. Z. Genack, "Fluctuations, correlations and average transport of electromagnetic radiation in random media," in *Scattering and Localization of Classical Waves in Random Media* (P. Sheng, ed.), Singapore: World Scientific, 1990.

[68] J. D. McKinney, M. A. Webster, K. J. Webb, and A. M. Weiner, "Characterization and imaging in optically scattering media by use of laser speckle and a variable-coherence source," *Opt. Lett.*, vol. 25, pp. 4–6, January 2000.

[69] A. W. Lohmann and B. Wirnitzer, "Triple correlations," *Proc. IEEE*, vol. 72, pp. 889–901, July 1984.

[70] H. Bartelt, A. W. Lohmann, and B. Wirnitzer, "Phase and amplitude recovery from bispectra," *Appl. Opt.*, vol. 23, pp. 3121–3129, September 1984.

[71] J. D. Gaskill, *Linear Systems, Fourier Transforms, and Optics.* New York: John Wiley & Sons, 1978.

[72] G. Parry, "Speckle patterns partially coherent light," in *Laser Speckle and Related Phenomena* (J. C. Dainty, ed.), Berlin: Springer-Verlag, second ed., 1984.

[73] R. Pnini and B. Shapiro, "Fluctuations in transmission of waves through disordered slabs," *Phys. Rev. B*, vol. 39, pp. 6986–6994, April 1989.

[74] J. J. Duderstadt and L. J. Hamilton, *Nuclear reactor analysis.* New York: Wiley, 1976.

[75] A. Ishimaru, "Diffusion of light in turbid material," *Appl. Opt.*, vol. 28, pp. 2210–2215, June 1989.

[76] K. Furutsu, "Diffusion equation derived from space-time transport equation," *J. Opt. Soc. Am.*, vol. 70, pp. 360–366, April 1980.

[77] A. H. Hielscher, R. E. Alcouffe, and R. L. Barbour, "Comparison of finite-difference transport and diffusion calculations for photon migration in homogeneous and hetergeneous tissues," *Phys. Med. Biol.*, vol. 43, pp. 1285–1302, 1998.

[78] A. D. Kim and A. Ishimaru, "Optical diffusion of continuous-wave, pulsed, and density waves in scattering media and comparisons with radiative transfer," *Appl. Opt.*, vol. 37, pp. 5313–5319, August 1998.

[79] R. C. Haskell, L. O. Svaasand, T. T. Tsay, T. C. Feng, M. S. McAdams, and B. J. Tromberg, "Boundary conditions for the diffusion equation in radiative transfer," *J. Opt. Soc. Am. A*, vol. 11, pp. 2727–2741, October 1994.

[80] M. S. Patterson, B. Chance, and B. C. Wilson, "Time resolved reflectance and transmittance for the non-invasive measurement of tissue optical properties," *Appl. Opt.*, vol. 28, pp. 2331–2336, June 1989.

[81] G. Barton, *Elements of Green's Functions and Propagation.* Oxford: Oxford University Press, 1989.

[82] R. Aronson, "Boundary conditions for diffusion of light," *J. Opt. Soc. Am. A*, vol. 12, pp. 2532–2539, November 1995.

[83] D. J. Durian, "Importance of boundary reflections in the theory of diffusive light scattering," *Opt. Eng.*, vol. 34, pp. 3344–3346, November 1995.

[84] A. H. Hielscher, S. L. Jacques, L. Wang, and F. K. Tittel, "The influence of boundary conditions on the accuracy of diffusion theory in time-resolved reflectance spectroscopy of biological tissues," *Phys. Med. Biol.*, vol. 40, pp. 1957–1975, 1995.

[85] C. A. Thompson, K. J. Webb, and A. M. Weiner, "Diffusive media characterization using laser speckle," *Appl. Opt.*, vol. 36, pp. 3726–3734, June 1997.

[86] C. A. Haniff, "Least-squares Fourier phase estimation frmo the modulo 2π bispectrum phase," *J. Opt. Soc. Am. A*, vol. 8, pp. 134–140, January 1991.

[87] C. L. Matson, "Weighted-least-squares phase reconstruction from the bispectrum," *J. Opt. Soc. Am. A*, vol. 8, pp. 1905–1913, December 1991.

[88] J. C. Marron, P. P. Sanchez, and R. C. Sullivan, "Unwrapping algorithm for least-squares phase recovery from the modulo 2π bispectrum phase," *J. Opt. Soc. Am. A*, vol. 7, pp. 14–20, January 1990.

[89] B. E. A. Saleh and M. C. Teich, *Fundamentals of Photonics.* New York: John Wiley & Sons, 1991.

[90] A. A. Scribot, "First-order probability denisty functions of speckle measured with a finite aperture," *Opt. Commun.*, vol. 11, pp. 238–241, July 1974.

[91] B. C. Park and M. S. Chung, "First-order probability denisty function of the integrated speckle," *Opt. Commun.*, vol. 83, pp. 5–9, May 1991.

[92] J. D. McKinney, "Characterization of thick, optically scattering media with laser speckle and a tunable coherence source," Master's thesis, Purdue Univ., 1999.

[93] L. Lepetit, G. Cheriaux, and M. Joffre, "Linear techniques of phase measurement by femtosecond spectral interferometry for applications in spectroscopy," *J. Opt. Soc. Am. B*, vol. 12, pp. 2467–2474, December 1995.

[94] J. M. Tualle, E. Tinet, and S. Avrillier, "A new and easy way to perform time-resolved measurements of the light scattered by a turbid medium," *Opt. Commun.*, vol. 189, pp. 211–220, March 2001.

[95] J. A. Ogilvy, "Computer simulations of acoustic wave scatering from rough surfaces," *J. Phys. D: Appl. Phys.*, vol. 21, pp. 260–277, 1988.

[96] J. A. Ogilvy and J. R. Foster, "Rough surfaces: Gaussian or exponential statistics?," *J. Phys. D: Appl. Phys.*, vol. 22, pp. 1243–1251, 1989.

[97] M. A. Berger, *An Introduction to Probability and Stochastic Processes.* New York: Springer-Verlag, 1993.

[98] J. W. Goodman, *Statistical Optics.* New York: John Wiley & Sons, 1985.

[99] R. A. Wooding, "The multivariate distribution of complex normal variables," *Biometrika*, vol. 43, pp. 212–215, 1956.

[100] T. L. Grettenberg, "A representation theorem for complex normal processes," *IEEE Trans. Inform. Theory*, vol. 11, pp. 305–306, April 1965.

[101] K. S. Miller, "Moments of complex Gaussian processes," *Proc. IEEE*, vol. 56, pp. 83–84, January 1968.

[102] K. S. Miller, "Complex Gaussian processes," *SIAM Rev.*, vol. 11, pp. 544–567, October 1969.

[103] R. N. Goodman, "Statistical analysis based on a certain multivariate complex Gaussian distribution," *Ann. Math. Stat.*, vol. 34, pp. 152–176, 1963.

APPENDICES

APPENDIX A: JOINT STATISTICS OF SCATTERED FIELD

In this appendix we develop the joint statistics of the scattered field from a random medium. We shall show that under the assumptions (i)–(iii) given in Section 2.1, the scattered fields measured at different frequencies have zero-mean circular complex Gaussian joint statistics.

We desire to determine the joint statistics of the output field at frequencies $\nu_1, \nu_2, \ldots, \nu_M$. Using (2.24) the output field of a random medium at frequency ν_m, for $m = 1, 2, \ldots, M$, is given by

$$E_o(\nu_m) = \frac{1}{\sqrt{N}} \sum_{k=1}^{N} A_k \exp\left[-j\phi_k(\nu_m)\right]. \tag{A.1}$$

We shall express the k^{th} elementary phasor of this sum in terms of its real and imaginary components, given by $x_k(\nu_m) = A_k \cos\phi_k(\nu_m)$ and $y_k(\nu_m) = -A_k \sin\phi_k(\nu_m)$, respectively. For each frequency ν_m, Goodman [47] has shown that these real and imaginary components of $E_o(\nu_m)$ are distributed as zero-mean Gaussian random variables, by using assumptions (i)–(iii) and applying the central limit theorem. However, having *marginal* Gaussian statistics for each frequency does not imply that real and imaginary components for all frequencies $\nu_1, \nu_2, \ldots, \nu_M$ are described by *jointly* Gaussian statistics [49].

To show that the statistics of $E_o(\nu_m)$ are jointly Gaussian we can simply apply a multivariate form of the central limit theorem given by Berger [97], which is stated as follows: Let $\mathbf{u}_1, \mathbf{u}_2, \ldots, \mathbf{u}_N$ be a sequence of zero-mean independent identically distributed random vectors of dimension $2M$ with finite second moments, $\langle ||\mathbf{u}_k||^2 \rangle < \infty$, and a common covariance matrix of C_u. Then the random vector $\mathbf{u}$ formed by

$$\mathbf{u} = \lim_{N\to\infty} \frac{1}{\sqrt{N}} \sum_{k=1}^{N} \mathbf{u}_k, \tag{A.2}$$

will be jointly Gaussian with a probability density function of

$$p_u(\mathbf{u}) = \frac{1}{(2\pi)^M |C_u|^{1/2}} \exp\left(-\tfrac{1}{2}\mathbf{u}^T C_u^{-1}\mathbf{u}\right). \tag{A.3}$$

To show that the real and imaginary components of (A.1) are jointly Gaussian for the frequencies $\nu_1, \nu_2, \ldots, \nu_M$, consider the following. Form the vectors $\mathbf{u}_1, \mathbf{u}_2, \ldots, \mathbf{u}_N$ from the real and imaginary components of $E_o(\nu_m)$ as

$$\mathbf{u}_1 = \begin{bmatrix} x_1(\nu_1) \\ \vdots \\ x_1(\nu_M) \\ y_1(\nu_1) \\ \vdots \\ y_1(\nu_M) \end{bmatrix}, \quad \mathbf{u}_2 = \begin{bmatrix} x_2(\nu_1) \\ \vdots \\ x_2(\nu_M) \\ y_2(\nu_1) \\ \vdots \\ y_2(\nu_M) \end{bmatrix}, \quad \ldots, \quad \mathbf{u}_N = \begin{bmatrix} x_N(\nu_1) \\ \vdots \\ x_N(\nu_M) \\ y_N(\nu_1) \\ \vdots \\ y_N(\nu_M) \end{bmatrix}. \tag{A.4}$$

Let the common covariance matrix of C_u be partitioned into sub-matrices in the following form

$$C_u = \begin{bmatrix} C_{xx} & C_{xy} \\ C_{yx} & C_{yy} \end{bmatrix}. \tag{A.5}$$

The $(i,j)^{\text{th}}$ element of the sub-matrix C_{xx} is given by $[C_{xx}]_{i,j} = \langle x(\nu_i)x(\nu_j)\rangle$, for sub-matrix C_{xy} it is given by $[C_{xy}]_{i,j} = \langle x(\nu_i)y(\nu_j)\rangle$, and similarly for the elements of sub-matrices of C_{yy}, and C_{yx}.

It is clear from assumptions (i)–(iii) that the random vectors formed in (A.4) are zero-mean, $\langle \mathbf{u}_k \rangle = 0$ for all k. To invoke the multivariate form of the central limit theorem, we must show that the random vectors have a finite second moment, $\langle ||\mathbf{u}_k||^2 \rangle < \infty$. This can be readily shown. Consider the vector norm

$$||\mathbf{u}_k||^2 = \sum_{m=1}^{M} A_k^2 \cos^2 \phi_k(\nu_m) + \sum_{m=1}^{M} A_k^2 \sin^2 \phi_k(\nu_m). \tag{A.6}$$

Taking the expected value of this vector norm and using assumption (iii), the statistical independence of the k^{th} random magnitude and random phase, gives

$$\langle ||\mathbf{u}_k||^2 \rangle = \sum_{m=1}^{M} \langle A_k^2 \rangle \langle \cos^2 \phi_k(\nu_m) \rangle + \sum_{m=1}^{M} \langle A_k^2 \rangle \langle \sin^2 \phi_k(\nu_m) \rangle. \tag{A.7}$$

By assumption (ii), the phase is uniformly distributed over the interval $-\pi$ to π, resulting in $\langle \cos^2 \phi_k(\nu_m) \rangle = 1/2$ and $\langle \sin^2 \phi_k(\nu_m) \rangle = 1/2$. Furthermore, by assumption

(i), the random magnitudes A_k are identically distributed, giving $\langle A_k^2 \rangle = \langle A^2 \rangle$. Using these results gives the expression

$$\langle ||\mathbf{u}_k||^2 \rangle = M \langle A^2 \rangle. \tag{A.8}$$

From (2.28), the quantity $\langle A^2 \rangle$ is equal to the ensemble average intensity $\langle I \rangle$, which must be finite from the conservation of energy principle. Thus, the second moment $\langle ||\mathbf{u}_k||^2 \rangle$ is also finite. Therefore, by the multivariate central limit theorem, the scattered field from a random medium $E_o(\nu_m)$ at frequencies ν_m have zero-mean jointly Gaussian statistics.

A.1 Circular Complex Gaussian Statistics

When the covariance matrix of (A.5) has a special structure, the jointly Gaussian real random vector of length $2M$ can be conveniently represented as a *circular* complex Gaussian random vector of length M. The conditions for this are [98, 49]

$$C_{xx} = C_{yy} \quad \text{and} \quad C_{yx} = -C_{xy}. \tag{A.9}$$

Forming the complex vector

$$\mathbf{z} = \begin{bmatrix} x(\nu_1) + jy(\nu_1) \\ \vdots \\ x(\nu_M) + jy(\nu_M) \end{bmatrix}, \tag{A.10}$$

a complex covariance matrix C_z can be defined whose $(i,j)^{\text{th}}$ element is given by $[C_z]_{i,j} = \langle z(\nu_i) z^*(\nu_j) \rangle$. It can be easily seen that $C_z = 2(C_{xx} - jC_{xy})$, when the relations given by (A.9) hold. Under these conditions, the joint probability density function for the complex random vector z can be written as [49]

$$p_z(\mathbf{z}) = \frac{1}{\pi^M |C_z|} \exp\left(-\mathbf{z}^H C_z^{-1} \mathbf{z}\right), \tag{A.11}$$

where $\mathbf{z}^H$ is the complex Hermitian transpose of $\mathbf{z}$. Further discussion on this form for the joint probability density function is given by Wooding [99] and by Grettenberg [100].

To show that the statistics of the output fields $E_o(\nu_m)$ given by (A.1) at frequencies ν_m from a random medium are circular complex Gaussian, we need to show that under assumptions (i)–(iii) the conditions given by (A.9) hold. Consider the $(i,j)^{\text{th}}$ element of the sub-matrix C_{xx} which given by

$$\langle x(\nu_i)x(\nu_j)\rangle = \frac{1}{N}\sum_{k=1}^{N}\sum_{l=1}^{N}\langle A_k A_l \cos\phi_k(\nu_i)\cos\phi_l(\nu_j)\rangle \tag{A.12}$$

Since the random magnitudes and random phases are assumed statistically independent, we can write

$$\begin{aligned}\langle x(\nu_i)x(\nu_j)\rangle = &\frac{1}{N}\sum_{k=1}^{N}\langle A_k^2\rangle\langle\cos\phi_k(\nu_i)\cos\phi_k(\nu_j)\rangle + \\ &\frac{1}{N}\sum_{k=1}^{N}\sum_{\substack{l=1\\ l\neq k}}^{N}\langle A_k\rangle\langle A_l\rangle\langle\cos\phi_k(\nu_i)\rangle\langle\cos\phi_l(\nu_j)\rangle.\end{aligned} \tag{A.13}$$

Under assumption (ii), the random phase is uniformly distributed from $-\pi$ to π, and the second summation term above is equal to zero. Relating the random phase to the random time of flight, as given by (2.25), and expanding the cosine product using a trigonometry identity, gives

$$\langle x(\nu_i)x(\nu_j)\rangle = \frac{1}{2N}\sum_{k=1}^{N}\langle A_k^2\rangle\left[\langle\cos 2\pi(\nu_i-\nu_j)t_k\rangle + \langle\cos 2\pi(\nu_i+\nu_j)t_k\rangle\right]. \tag{A.14}$$

The second ensemble average cosine term is equal to zero, because if the phases of $2\pi\nu_i t_k$ and $2\pi\nu_j t_k$ are each assumed uniform over $-\pi$ to π when taken modulo 2π, then so is the phase $2\pi(\nu_i+\nu_j)t_k$. However, we cannot make the same assumption about the phase $2\pi(\nu_i-\nu_j)t_k$, because the value of $1/(\nu_i-\nu_j)$ may not be large when compared with range of values for t_k. Finally, since the random magnitudes are identically distributed, and the random times of flight are identically distributed, we obtain the result

$$\langle x(\nu_i)x(\nu_j)\rangle = \langle A^2\rangle\langle\cos 2\pi(\nu_i-\nu_j)t\rangle/2. \tag{A.15}$$

Using the same procedure, one can easily obtain expressions for all the $(i,j)^{\text{th}}$ elements of the sub-matrices C_{yy}, C_{xy}, and C_{yx} which are summarized as

$$\begin{aligned}
\langle x(\nu_i)x(\nu_j)\rangle &= \langle A^2\rangle\langle\cos 2\pi(\nu_i-\nu_j)t\rangle/2 \\
\langle y(\nu_i)y(\nu_j)\rangle &= \langle A^2\rangle\langle\cos 2\pi(\nu_i-\nu_j)t\rangle/2 \\
\langle x(\nu_i)y(\nu_j)\rangle &= \langle A^2\rangle\langle\sin 2\pi(\nu_i-\nu_j)t\rangle/2 \\
\langle y(\nu_i)x(\nu_j)\rangle &= -\langle A^2\rangle\langle\sin 2\pi(\nu_i-\nu_j)t\rangle/2.
\end{aligned} \tag{A.16}$$

Thus, we can readily see that the expressions given in (A.16) satisfy the conditions of (A.9) for all i,j. Therefore, the output fields $E_o(\nu_m)$ for frequencies ν_m from a random medium have circular complex Gaussian statistics under assumptions (i)–(iii). This enables use of the Gaussian moment theorem of Reed [65] for calculating all moments of the random output field.

APPENDIX B: GAUSSIAN MOMENT THEOREM

In this appendix the Gaussian moment theorem of Reed [65] is discussed. The statistics for a set of random variables sampled from a zero-mean circular complex Gaussian random process with a pdf given by (A.11) can be completely specified by the elements of complex covariance matrix C_z. The entries of this matrix are second order moments of the form $[C_z]_{i,j} = \langle z_i z_j^* \rangle$, where z_i and z_j are random variables. It is possible to express moments of any order in terms of these second order moments, which is a property of Gaussian distributions in general [49].

The Gaussian moment theorem for zero-mean circular complex random variables can be expressed as [65]

- A set of N complex random variables $z_1, z_2, \ldots, z_N$ are chosen having a pdf given by (A.11)
- Two sets of integers, $m = \{m_1, m_2, \ldots, m_t\}$ and $n = \{n_1, n_2, \ldots, n_s\}$, consisting of t and s elements respectively with $s, t \geq 0$ are selected. The entries of these sets can take on any values such that $1 \leq m_i, n_i \leq N$.
- For $s \neq t$, the moment of

$$\langle z_{m_1} z_{m_2} \ldots z_{m_t} z_{n_1}^* z_{n_2}^* \ldots z_{n_s}^* \rangle = 0. \tag{B.1}$$

- For $s = t$, the moment of

$$\langle z_{m_1} z_{m_2} \ldots z_{m_t} z_{n_1}^* z_{n_2}^* \ldots z_{n_t}^* \rangle = \sum_p \langle z_{m_1} z_{p_1}^* \rangle \langle z_{m_2} z_{p_2}^* \rangle \cdots \langle z_{m_t} z_{p_t}^* \rangle, \tag{B.2}$$

  where p is the summation over the $t!$ possible permutations of the set of integers $\{n_1, n_2, \ldots, n_t\}$.

It must be emphasized, that the above relations for the Gaussian moment theorem only hold for zero-mean *circular* complex random variables. Non zero-mean random

variables can be transformed by subtracting the mean to form a set of zero-mean random variables. In the case of non-circular complex Gaussian random variables, the result of (B.2) cannot be used. Further details on the statistics of circular complex Gaussian processes can be found in [101, 100, 102, 103].

B.1 Some Examples

It can be seen that when the number of conjugated and un-conjugated terms in the correlation on the RHS of (B.2) must be the same otherwise the result is zero. For the case of $s = t$, we have the sum of $t!$ terms, where each term is the product of t second order correlations. Some examples are list below.

$$
\begin{aligned}
\langle z_1 z_2 z_3^* \rangle &= 0 \\
\langle (z_1 z_2^*)^n \rangle &= n! \langle z_1 z_2^* \rangle^n \\
\langle z_1 z_2 z_3^* z_4^* \rangle &= \langle z_1 z_3^* \rangle \langle z_2 z_4^* \rangle + \langle z_1 z_4^* \rangle \langle z_2 z_3^* \rangle \\
\langle |z_1|^2 |z_2|^2 \rangle &= \langle |z_1|^2 \rangle \langle |z_2|^2 \rangle + |\langle z_1 z_2^* \rangle|^2 \\
\langle z_1 z_2 z_3 z_4^* z_5^* z_6^* \rangle &= \langle z_1 z_4^* \rangle \langle z_2 z_5^* \rangle \langle z_3 z_6^* \rangle + \langle z_1 z_4^* \rangle \langle z_2 z_6^* \rangle \langle z_3 z_5^* \rangle + \langle z_1 z_5^* \rangle \langle z_2 z_4^* \rangle \langle z_3 z_6^* \rangle + \\
&\quad \langle z_1 z_5^* \rangle \langle z_2 z_6^* \rangle \langle z_3 z_4^* \rangle + \langle z_1 z_6^* \rangle \langle z_2 z_4^* \rangle \langle z_3 z_5^* \rangle + \langle z_1 z_6^* \rangle \langle z_2 z_5^* \rangle \langle z_3 z_4^* \rangle \\
\langle |z_1|^2 |z_2|^2 |z_3|^2 \rangle &= \langle |z_1|^2 \rangle \langle |z_2|^2 \rangle \langle |z_3|^2 \rangle + \\
&\quad \langle |z_1|^2 \rangle |\langle z_2 z_3^* \rangle|^2 + \langle |z_2|^2 \rangle |\langle z_1 z_3^* \rangle|^2 + \langle |z_3|^2 \rangle |\langle z_1 z_2^* \rangle|^2 + \\
&\quad 2\mathrm{Re}\left\{ \langle z_1 z_2^* \rangle \langle z_2 z_3^* \rangle \langle z_3 z_1^* \rangle \right\}
\end{aligned}
$$

VITA

VITA

Mark Andrew Webster was born in Melbourne, Australia, on September 16, 1967. He received his B.Eng (Bachelor of Engineering) degree in Electronic Engineering from R.M.I.T. (Royal Melbourne Institute of Technology), with distinction, in 1990. He received a M.Eng (Master of Engineering) degree in 1994, also from R.M.I.T. Prior to arriving at Purdue University in August 1996 to pursue a Ph.D. degree, he worked at R.M.I.T as a research engineer, modeling, designing, fabricating, and testing integrated optical modulators in Lithium Niobate.